SELF-ORGANIZED NANOPOROUS MATERIALS FOR CHEMICAL SEPARATIONS AND CHEMICAL SENSING

by

BIPIN PANDEY

B.S., Truman State University, 2007

AN ABSTRACT OF A DISSERTATION

submitted in partial fulfillment of the requirements for the degree

DOCTOR OF PHILOSOPHY

Department of Chemistry
College of Arts and Sciences

KANSAS STATE UNIVERSITY
Manhattan, Kansas

2013

Abstract

Self-organized nanoporous materials have drawn a lot of attention because the uniform, highly dense, and ordered cylindrical nanopores in these materials provide a unique platform for chemical separations and chemical sensing applications. Here, we explore self-organized nanopores of PS-*b*-PMMA diblock copolymer thin films and anodic gallium oxide for chemical separations and sensing applications.

In the first study, cyclic voltammograms of cytochrome c on recessed nanodisk-array electrodes (RNEs) based on nanoporous films (11, 14 or 24 nm in average pore diameter; 30 nm thick) derived from polystyrene-poly(methylmethacrylate) diblock copolymers were measured. The faradic current of cytochrome c was observed on RNEs, indicating the penetration of cytochrome c (hydrodynamic diameter ≈ 4 nm) through the nanopores to the underlying electrodes. Compared to the 24-nm pores, the diffusion of cytochrome c molecules through the 11- and 14-nm pores suffered significantly larger hindrance. The results reported in this study will provide guidance in designing RNEs for size-based chemical sensing and also for controlled immobilization of biomolecules within nanoporous media for biosensors and bioreactors.

In another study, conditions for the formation of self-organized nanopores of a metal oxide film were investigated. Self-organized nanopores aligned perpendicular to the film surface were obtained upon anodization of gallium films in ice-cooled 4 and 6 M aqueous H_2SO_4 at 10 V and 15 V. The average pore diameter was in the range of 18 ~ 40 nm, and the anodic gallium oxide was ca. 2 μm thick. In addition, anodic formation of self-organized nanopores was demonstrated for a solid gallium monolith incorporated at the end of a glass capillary. Nanoporous anodic oxide monoliths formed from a fusible metal will lead to future development of unique devices for chemical sensing and catalysis.

In the final study, surface chemical property of self-organized nanoporous anodic gallium oxide is explored through potentiometric measurements. The nanoporous anodic and barrier layer gallium oxide structures showed slow potentiometric response only at acidic pH (≤ 4), in contrast to metallic gallium substrates that exhibited a positive potentiometric response to H^+ over the pH range examined (3-10). The potentiometric response at acidic pH probably reflects some chemical processes between gallium oxide and HCl.

SELF-ORGANIZED NANOPOROUS MATERIALS FOR CHEMICAL SEPARATIONS AND CHEMICAL SENSING

by

BIPIN PANDEY

B.S., Truman State University, 2007

A DISSERTATION

submitted in partial fulfillment of the requirements for the degree

DOCTOR OF PHILOSOPHY

Department of Chemistry
College of Arts and Sciences

KANSAS STATE UNIVERSITY
Manhattan, Kansas

2013

Approved by:

Major Professor
Takashi Ito

Copyright

Abstract

Self-organized nanoporous materials have drawn a lot of attention because the uniform, highly dense, and ordered cylindrical nanopores in these materials provide a unique platform for chemical separations and chemical sensing applications. Here, we explore self-organized nanopores of PS-*b*-PMMA diblock copolymer thin films and anodic gallium oxide for chemical separations and sensing applications.

In the first study, cyclic voltammograms of cytochrome c on recessed nanodisk-array electrodes (RNEs) based on nanoporous films (11, 14 or 24 nm in average pore diameter; 30 nm thick) derived from polystyrene-poly(methylmethacrylate) diblock copolymers were measured. The faradic current of cytochrome c was observed on RNEs, indicating the penetration of cytochrome c (hydrodynamic diameter ≈ 4 nm) through the nanopores to the underlying electrodes. Compared to the 24-nm pores, the diffusion of cytochrome c molecules through the 11- and 14-nm pores suffered significantly larger hindrance. The results reported in this study will provide guidance in designing RNEs for size-based chemical sensing and also for controlled immobilization of biomolecules within nanoporous media for biosensors and bioreactors.

In another study, conditions for the formation of self-organized nanopores of a metal oxide film were investigated. Self-organized nanopores aligned perpendicular to the film surface were obtained upon anodization of gallium films in ice-cooled 4 and 6 M aqueous H_2SO_4 at 10 V and 15 V. The average pore diameter was in the range of 18 ~ 40 nm, and the anodic gallium oxide was ca. 2 μm thick. In addition, anodic formation of self-organized nanopores was demonstrated for a solid gallium monolith incorporated at the end of a glass capillary. Nanoporous anodic oxide monoliths formed from a fusible metal will lead to future development of unique devices for chemical sensing and catalysis.

In the final study, surface chemical property of self-organized nanoporous anodic gallium oxide is explored through potentiometric measurements. The nanoporous anodic and barrier layer gallium oxide structures showed slow potentiometric response only at acidic pH (≤ 4), in contrast to metallic gallium substrates that exhibited a positive potentiometric response to H^+ over the pH range examined (3-10). The potentiometric response at acidic pH probably reflects some chemical processes between gallium oxide and HCl.

Table of Contents

List of Figures

List of Tables

Acknowledgements

I am very fortunate to have teachers, colleagues, friends, and family who were constant source of inspiration throughout my graduate studies. I am glad to have this opportunity to thank all those who have helped me in some way or the other. I must say that the work presented in this thesis would have not been possible without their help.

First of all, I would like to thank my advisor Professor Takashi Ito for providing me the opportunity to conduct research projects in his group. I have learned a lot from him throughout my graduate studies. Dr. Ito always motivated me and gave fruitful advice during experimental set-up, data analysis, manuscript writing and paper presentation. I admire his encouragement that helped me think independently to solve research problems. I would not have been able to achieve this much without his support and guidance. I would like to thank Dr. Ito for nominating my name for summer stipends and department research award. I cannot thank him enough for all he has done for me.

I am very grateful to the members of my advisory committee for their guidance and support in the course of my graduate studies and doctoral research. My sincere appreciation goes to Professor Christopher Culbertson, Professor Peter Pfromm, and Professor Paul Smith for their suggestions on my PhD proposal and their valuable time. I would like to thank the outside chairperson Professor Antje Philine Wangemann for her time and her willingness to conduct the exam.

Special thanks to Ruben Diaz, Khanh Hoa Tran Ba, Dr. Yongxin Li, Dr. Prem Thapa and Professor Daniel Higgins who were involved in my PhD work. I would like to take this opportunity to thank all the group members of the Ito group, both past and present, for their suggestions and advice as well as their help in the laboratory works. I am very grateful to Khanh Hoa Tran Ba, a fellow graduate student in Ito group, for his help with finite element simulations and undergraduate student Christian Cox for his help with the potentiometric measurements. To Khanh Hoa Tran Ba, Christian Cox, Dol Raj Sapkota, Chrishani De Silva, Ruben Diaz, Dr. Feng Li, Dr. Yongxin Li, Dr. Shaida Ibrahim, Dr. Neluni Perera, and Dr. Helene Maire: I have learnt so much from each of you. Thank you all for making the laboratory working environment a very enjoyable one.

I would like to convey many thanks to Dr. David Moore, Dr. Prem Thapa, and Heather Shinogle at the Microscopy and Analytical Imaging Laboratories, University of Kansas for all their help with electron microscopy imaging. Thank you to Ranju Karna, a graduate student at K-State Agronomy department, for her help with the Inductively Coupled Plasma Atomic Absorption Spectroscopy measurements. I would also like to thank Professor Kenneth Klabunde and Professor Emily McLaurin for letting me use the UV-Vis spectrometer.

To the chemistry department staff – I would like to thank Tobe Eggers for his technical support with computer systems, Ron Jackson for fabricating electrochemical cells and devices for me, Jim Hodgson for all his help with the glassware items he provided very promptly upon request. Thanks also to Ralph Hudson, Christa Obermeyer, Lisa Percival, Mary Dooley, Kimberly Ross, Donna Wright, Connie Cusimano, Brenda Luther, and Arlon Meek for helping me in various ways. Special thanks go to Earline Dikeman, the Director of Undergraduate Laboratories for the mentorship she provided when I was a Graduate Teaching Assistant. I admire her enthusiasm towards chemical education and her flexibility with assigning the teaching duties.

I would like to acknowledge the funding agencies for their financial support: ACS petroleum research fund, Terry C. Johnson Center for Basic Cancer Research and Division of Chemical Sciences, Geosciences, and Biosciences, Office of Basic Energy Sciences of the U.S. Department of Energy. Thanks to the department of chemistry at Kansas State University for their support with Graduate Teaching Assistantships.

I am deeply grateful to my parents: late father Birendra Lal Pandey and mother Laxmi Pandey, for providing all the support and care. Thanks to my brother and his family for their support. By providing good care to my mother, they have given me a peace of mind which enabled me to concentrate on my studies. Thanks also to my sister and her family. Had she not constantly encouraged me, my dreams of a higher education in the US would not have materialized. Special thanks go to my wife Richa Sharma and her family. Richa has been my lady luck and her presence in my life has always brought me good fortunes. I am very thankful for all her love and support. I acknowledge her patience and understanding at times when I was unable to provide her time. I am very fortunate to have a wonderful, loving and caring family and I owe it all to them.

I would also like to take this moment to thank all my teachers who have given me the wonderful gift of education. I would not have been the person I am now without your help. Thank you very much. I have been very lucky to have very good friends around me both at Kansas State University and Truman State University. I would like to thank my dear friend Kiran Khadka and my host mom Nancy Forquer who provided me the guardianship at Truman State University. Special thanks go to another dear friend Dr. Deepak Shrestha from physics department at Kansas State University, who has always been there for me to share my moments of joy and sorrow. Thank you to all the members of the Nepalese Student Association for making me feel at home. All of you have been very wonderful and I will always remember the good times we had together at K-State. I would also like to thank the K-State Housing and Dining Jardine Apartments for providing an inexpensive, quiet and amazing housing facility.

I have had it all at graduate school: moments of joy, pride, disappointment and frustration. However, to sum it up, it was simply wonderful and rewarding thanks to the faculty, staff and students at K-State. Once again thank you to all who have made a difference in my life.

Dedication

This work is dedicated to my mother Laxmi Pandey, late father Birendra Lal Pandey, wife Richa Sharma, all my loved ones and my country Nepal.

List of Abbreviations

PS-*b*-PMMA	Polystyrene- poly(methylmethacrylate)
PMMA	Polymethylmethacrylate
BCP	Block Copolymers
ODT	Order-Disorder Transition
AFM	Atomic Force Microscopy
PPS-PI-PPS	Poly (4-vinylphenyl-dimethyl-2-propoxysilane)-*b*-polyisoprene-*b*-poly (4-vinylphenyl-dimethyl-2-propoxysilane)
PS-PBD	Polystyrene-polybutadiene
HRV	Human Rhino Virus
CV	Cyclic Voltammetry
AAO	Anodic Aluminum Oxide
ATO	Anodic Titanium Oxide
RNE	Recessed Nanodisk Electrodes
SEM	Scanning Electron Microscopy
EDS/EDX	Energy Dispersive X-ray Spectroscopy
STEM	Scanning Tunneling Microscopy
CRT	Cathode Ray Tube
CF-PS-*b*-PMMA	Cylinder-Forming-Polystyrene-poly(methylmethacrylate)
ICP-AES	Inductively Coupled Plasma Atomic Emission Spectroscopy

Chapter 1 - Introduction

This dissertation describes the fabrication and characterization of self-organized nanoporous materials made up of polystyrene-poly(methylmethacrylate) (PS-*b*-PMMA) diblock copolymer as well as anodic gallium oxide. The self-organized, uniform, cylinder-shaped nanopores in these materials offer unique advantages for chemical separations and sensing applications as explained in this dissertation.

In this chapter, first of all the objectives and motivation for carrying out the studies described in this dissertation will be explained. This will be followed by background/literature review section that provides an overview of the self-organized nanoporous materials. In particular, those nanoporous materials that have been used in the studies described in this dissertation i.e. block copolymers and anodic metal oxides, will be discussed. In this dissertation, metallic gallium has been used to form anodic gallium oxide. So, the properties of gallium and its electrochemistry will be briefly described. The surface chemical properties of nanoporous anodic gallium oxide have been studies using potentiometric measurements. Thus, literature review on potentiometric studies performed on metal oxides will be presented. The chapter concludes with an outline of the dissertation.

1.1 Objectives and Motivation

Self-organized nanoporous materials with uniform cylindrical pores are attractive candidates for various applications. This dissertation aims to understand the properties of self-organized nanoporous materials based on block copolymers (BCP) and anodic metal oxides. The studies described in this dissertation utilizes the cylindrical nanopores obtained from these materials for analytical applications: size-exclusion properties of block copolymer derived nanopores make them a candidate for size-based chemical sensing, while capillary incorporated anodic gallium oxide has been used as a sensor material.

Block copolymer derived polystyrene-poly(methylmethacrylate) nanoporous membranes were used to study the diffusion of a protein molecule, cytochrome c via electrochemical methods. It was found that smaller nanopores provide steric hindrance to the diffusion of

cytochrome c molecules. The results hinted that these block copolymer based membranes could be used for size and charge based separation of the analytes. However, it has to be noted that in order to utilize these membranes for separation, they have to be either made as a free-standing membrane or used in conjunction with a porous solid support. The preparation of these membranes as free-standing monolith was attempted inside the narrower end of a silica capillary. Unfortunately, cracks in these monoliths were observed possibly due to the shrinkage of the polymer. This led us to try an alternative approach.

It has been reported in literature that anodic oxidation of valve metals in acidic electrolyte solution lead to the formation of self-organized nanopores. Self-organized nanopores of anodic alumina have been extensively studied for a very long time. Gallium and aluminum belong to the same group of the periodic table and thus we hypothesized that anodization of gallium in acidic electrolytes should form self-organized nanoporous structure. Indeed, we have verified our hypothesis and confirmed that gallium could be anodized to form self-organized nanoporous structures.

Gallium is a fusible metal with a very low melting point (29.7 °C). Therefore, it can be incorporated inside a silica capillary. The density of gallium and gallium oxide is very similar. Thus nanoporous anodic gallium oxide incorporated inside a silica capillary should suffer from no leaks or cracks. Indeed, we have demonstrated that capillary incorporated gallium could be anodized to form self-organized nanoporous structures. In order to utilize these monoliths for separation purpose, it is necessary to prepare an anodic gallium oxide monolith containing nanopores that bridge the two fluidic spaces. So far, we have not been able to prepare such a monolith. We are looking for ways to remove the barrier oxide and the metallic layers present at the other side of the capillary.

The surface chemical property of the nanoporous anodic gallium oxide successfully prepared via anodic oxidation has been studied by potentiometry. Specifically, *p*H-dependent potentiometric responses with the nanoporous anodic gallium oxide monoliths have been measured in a supporting electrolyte of 0.01 *M* LiCl by adjusting the *p*H with HCl or LiOH solution containing 0.01 *M* LiCl. The nanoporous anodic gallium oxide structures showed slow potentiometric response only at acidic pH (≤ 4). If the surface chemical properties as well as material properties of these nanoporous gallium oxide are well understood, they can be efficiently used for applications such as sensors and catalysts.

1.2 Background/Literature review

1.2.1 Self-Organized Nanoporous Materials

Self-organized nanoporous materials are interesting materials. They have been used for many applications such as membrane filtration, or as a template for synthesis of other nanostructured materials. The research involving these self-organized materials has developed around two focus areas. The fabrication and characterization of these materials as well understanding the mechanism of their formation constitute the first area, while the second area addresses possible applications of these materials. Nanoporous materials based on anodic metal oxides, track-etched polycarbonate membranes, block copolymers, sol-gel precursor derived materials, and zeolites are some of the types of these materials that have been explored. In the following section, BCP based nanoporous materials will be discussed. A brief history of BCP derived materials will be presented and polystyrene-poly(methylmethacrylate) block copolymer thin films will be introduced. The preceding section will discuss the anodic oxide based nanoporous materials.

1.2.2 Block-copolymer based nanoporous materials

Block copolymers comprise two or more homopolymer subunits linked via a covalent bond. Nanoporous membranes fabricated from BCPs have a higher pore density and a narrow pore size distribution, compared to track-etch polycarbonate membrane. Also, their pore size can be easily tuned by choosing an appropriate molecular weight. Block-copolymer based nanoporous materials are interesting materials because they can be used as lithographic masks,[1,2] as templates for nanomaterials synthesis,[3-5] for electrophoretic deposition of nanoparticles,[6] and for virus filtration.[7] A block copolymer molecule contains two or more polymer chains attached at their ends. The microphase separation of block copolymer leads to nanoscale-ordered morphologies. The phase behavior of block copolymer melts is explained in a phase diagram in terms of χN and f as shown in **Figure 1.1**.[8] Here f is the volume fraction of one block, χ is the Flory-Higgins interaction parameter, which reflects the interaction energy between different segments and N is the degree of polymerization. When the product χN exceeds a critical value

i.e. $(\chi N)_{ODT}$ (ODT = order-disorder transition), the block copolymer microphase separates into a periodically ordered structure, with a length scale of ~5-500 nm.

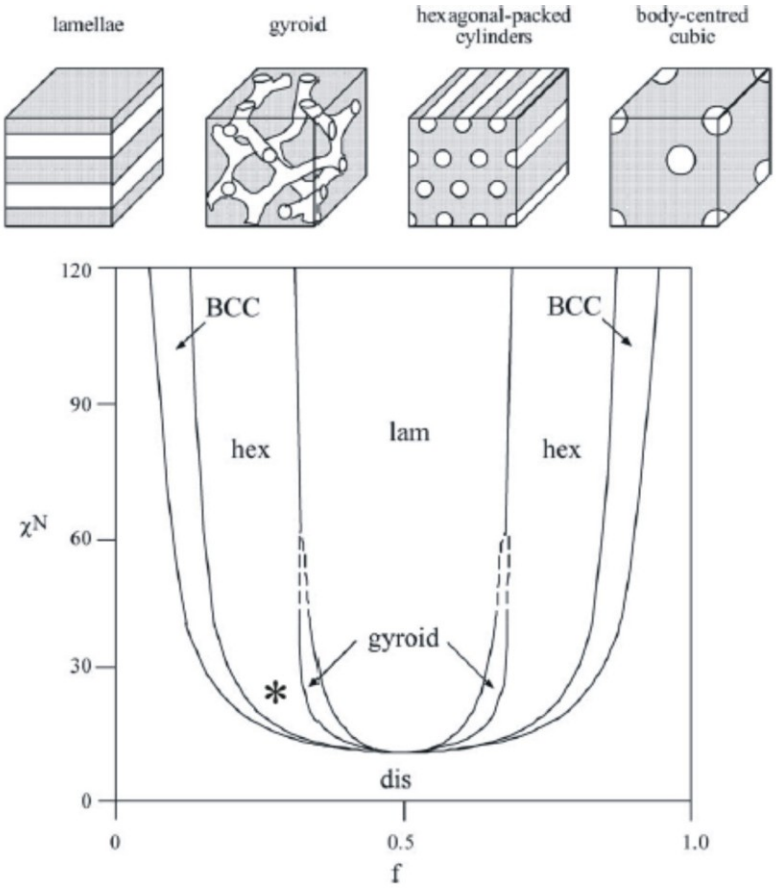

Figure 1.1 The phase diagram of a diblock copolymer. (Reproduced from ref. 8 by permission of Elsevier B.V. Copyright © 2004.)

As shown in the phase diagram in **Figure 1.1**, the structure is disordered below $(\chi N)_{ODT}$. Whenever $(\chi N)_{ODT}$ is reached or exceeded depending upon the volume fraction, different periodically ordered structures such as body-centered cubic, hexagonal, gyroid or lamellae are obtained. For the diblock copolymer PS-*b*-PMMA used in this dissertation, volume fraction of 0.3 for PMMA was used. The molecular weight of the polymers used gives a value for the χN parameter that is above the ODT so that hexagonally ordered cylinders of PMMA in the matrix of PS were obtained as shown by an "asterisk" in the phase diagram itself.

1.2.2.1 Fabrication of block-copolymer thin films

Block copolymer thin films can be prepared by spin-coating technique, where drops of a solution of the polymer in a volatile organic solvent are deposited on a spinning solid substrate. The polymer films spread by centrifugal forces and the volatile solvent is rapidly driven off. When carefully prepared, this method can give films with a low surface roughness over areas as large as square millimeters. The film thickness can be controlled through the spin speed, concentration of block copolymer solution or the volatility of the solvent. Dip coating is another method for fabricating thin films. However, the spin-coating technique was used to prepare the samples used in this dissertation for advantages aforementioned.

1.2.2.2 Characterization of block-copolymer thin films

The film thickness of the block-copolymer thin films can be estimated by either ellipsometry or profilometry. Their surface morphology can be investigated by atomic force microscopy (AFM). Sometimes, islands and holes can have dimensions of micrometers and consequently may be observed using optical microscopy. Suitably etched or sectioned samples can be examined by transmission electron microscopy.

1.2.3 Brief history of block copolymers

BCPs are hybrid macromolecules which phase separate into nanodomains in the matrix of bulk segment due to incompatibility of the monomeric segments. Using a triblock copolymer, Lee *at al*. in 1988 for the first time demonstrated the fabrication of block copolymer derived porous membranes.[9] Their triblock copolymer; poly (4-vinylphenyl-dimethyl-2-propoxysilane)-*b*-polyisoprene-*b*-poly (4-vinylphenyl-dimethyl-2-propoxysilane) (PPS-PI-PPS) film, showed formation of a lamellar morphology. After degrading the minor PI component via ozonolysis followed by methanol treatment, the porous structure was obtained. They used the same triblock copolymer in another work to form porous structures with different morphologies as verified by SEM and TEM images.[10] The authors were of the opinion that the presence of residual functional groups could be a potential site for functionalization. These noteworthy works done by Lee *at al* in the area of block copolymer precursors have led to the continual fabrication of nanoporous structures.[11-15] Nanoporous films derived from block copolymers as a lithographic template material was first demonstrated by Mansky *et al* when they succeeded in orienting the cylindrical

domains perpendicular to the underlying substrate.[13] The results obtained in their study were crucial because templating applications require perpendicular domains. Thin films of polystyrene-polybutadiene (PS-PBD) with vertically oriented PBD domains were prepared and the PBD component degraded via ozonolysis to generate a well-ordered porous template. Ever since, research involving the use of the patterns produced by the self-assembly of block copolymer systems as lithographic templates has flourished.[2,16-18] Driven by this promising application and possible new ones, a vast amount of research has been devoted to studying the self assembly of block copolymers in terms of its chemistry and thermodynamics. In this regard, it is not surprising that BCPs fall into the category of nanomaterials that are well-explored and documented.[19-23] The majority of such work was driven by the potential applications of block copolymer derived nanoporous materials as heterogeneous catalysts,[24] chemical sensors,[25] separation membranes,[7,26,27] and lithographic templates for the synthesis of nanomaterials of desired size and shapes.[6,28,29] In this dissertation, block copolymer derived nanoporous thin films have been utilized to form a recessed nanodisk electrodes to study the diffusion of cytochrome c molecule within the nanopores. The diblock copolymer used in this dissertation i.e. PS-*b*-PMMA will be briefly discussed in the next section.

1.2.4 PS-b-PMMA thin films

Among block copolymer systems, PS-*b*-PMMA (**Figure 1.2(a)**) has been widely used to fabricate nanostructured materials[3,6,7,28-30] because well-established procedures for selectively etching the PMMA domains to form the nanoporous structure are already known.[17] The self-assembly of cylinder forming PS-*b*-PMMA, where the PMMA domains were oriented perpendicular to an underlying substrate, was first demonstrated by Thurn-Albrecht *et al* in 2000.[17] PS-*b*-PMMA with a PMMA volume fraction of 0.3 was used where PMMA formed the minor component. Thurn-Albrecht and co-workers demonstrated that nanopores were easily formed via exposure of the PS-*b*-PMMA thin films to UV radiation at 254 nm and subsequent acetic acid treatment to rinse away the degraded PMMA debris. This treatment transformed the PS-*b*-PMMA BCP into a nanoporous template with arrays of vertically aligned void cylinders. PS-PMMA is the only block copolymer system that requires UV radiation to form the nanoporous structure. Figure 2c shows an AFM image of the surface of a PS-*b*-PMMA film. The

phase separated PMMA domains shown as dots were induced by annealing at 170 °C. Upon UV-irradiation and subsequent treatment with acetic acid, the PMMA domains could be removed to give a nanoporous film as shown in figure 2d. For PS-*b*-PMMA film, degradation of PMMA and crosslinking of the PS occur in a single exposure step making the resulting PS matrix mechanically and chemically stable.

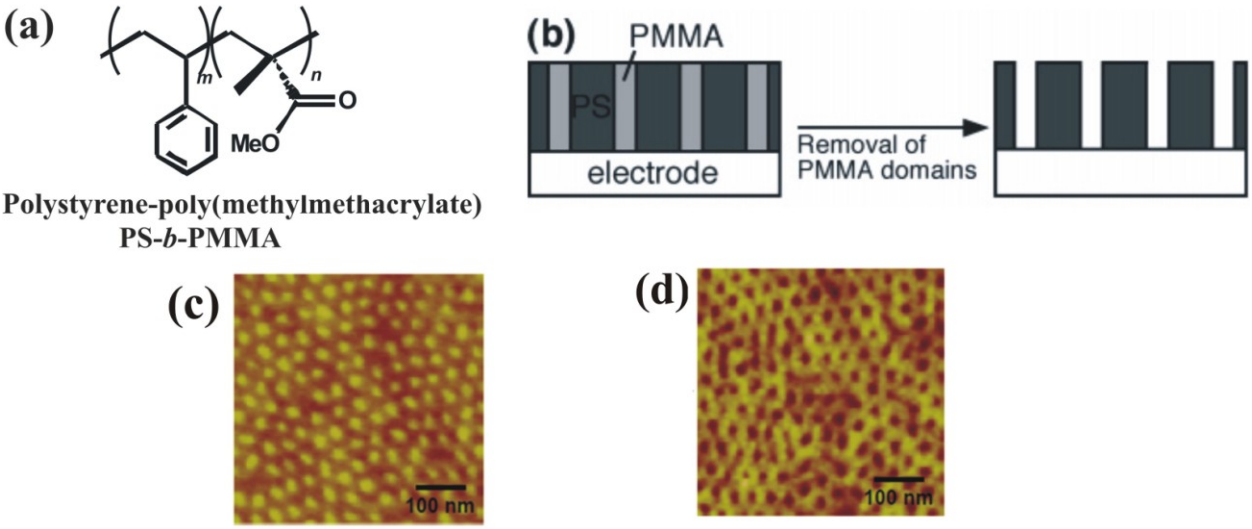

Figure 1.2 (a) Chemical structure of a PS-*b*-PMMA diblock copolymer. (b) Schematic of a PS-*b*-PMMA phase separated block copolymer film with cylindrical PMMA domains before and after the removal of PMMA. AFM images of (c) annealed PS-*b*-PMMA film showing the PMMA domains as dots and (d) nanoporous film formed by the degradation of the PMMA domain upon UV irradiation and subsequent acetic acid treatment. (Reproduced from ref. 32 by permission of American Chemical Society, Copyright © 2007.)

In addition to demonstrating the vertical alignment of cylinder forming PS-*b*-PMMA, Thurn-Albrecht *et al* also showed the use of vertically-aligned PS-*b*-PMMA as a nanoporous template for the fabrication of cobalt nanowires.[3] The nanowires grown within the templates had dimensions of the void cylindrical domains in the template: length of 500 nm and diameter of 14 nm.[3] Kim *et al*. from the same group also showed that silicon dioxide pillars, having a height of 6 nm and a diameter of 20 nm could be grown inside thin nanoporous PS-*b*-PMMA templates.[4] Guarini *et al*. demonstrated the deposition of gold nanodot arrays onto a nanoporous PS-*b*-

PMMA block copolymer template.[1] Thus, the use of PS-*b*-PMMA block copolymers as template materials allowed the synthesis of various nanomaterials. These pioneering studies with PS-*b*-PMMA system spurred interest in research to explore new potential for nanoporous PS-*b*-PMMA block copolymer thin films other than its use as nanolithographic templates.

PS-*b*-PMMA block copolymer films prepared on a solid porous support have also been used as free-standing membranes for separation and filtration purposes. Yang *et al.* have reported the filtration of human rhino virus (HRV) using PS-*b*-PMMA derived nanoporous membranes.[7] HRV (30 nm in diameter) was trapped by the PS-*b*-PMMA derived nanopores (~15 nm in diameter) while smaller protein molecules (bovine serum albumin) could pass through the nanopores. Kim *et al.* later developed PS-*b*-PMMA nanoporous membranes that are mechanically and chemically more robust. Crosslinking of the PS matrix and mixed nanopore orientation inside the membrane improved the stability. This avoided the damage of the membrane by application of pressure (2 bar) or by exposure to acidic, basic and organic solutions.

PS-*b*-PMMA derived recessed nanoelectrode array electrodes were fabricated and characterized previously.[31] Jeoung *et al.* performed cyclic voltammetry to study the penetration of redox active molecules through the nanopores to the underlying electrode. The surface chemical properties of the inner walls of the cylindrical nanopores formed in UV treated PS-*b*-PMMA derived RNEs was characterized via cyclic voltammetry (CV) and IR in previous projects conducted by the Ito group.[25,26,32] The presence of -COOH groups lining the pore walls was shown through pH-dependent CV measurements of charged and uncharged redox molecules.[32] In addition, the nanopore surface functionalization via 1-ethyl-3-(3-dimethylaminopropyl)carbodiimide-mediated amidation of the surface -COOH groups was also demonstrated.[25] The difference in surface properties of the PS and PMMA domains in the PS-*b*-PMMA thin films was studied with chemical force microscopy and the preferential deposition of ferritin onto the nanoscale PS ridges was observed.[33] The size exclusion of Ferritin by PS-*b*-PMMA derived nanopores was shown using electrochemical measurements.[26] Ferritin, which has a diameter around 12nm, was excluded by pores ~15nm in diameter. This result made us curious to understand how would an even smaller protein behave within the nanopores? The curiosity led us to pursue the study of diffusion of cytochrome c within PS-*b*-PMMA nanopores as described in chapter 3.

Now that the background for block copolymers and in particular PS-*b*-PMMA has been discussed, the attention is diverted to another type of material: the anodic metal oxide based nanoporous materials. The discussion is as follows.

1.2.5 Anodic metal oxide based nanoporous materials

Anodic metal oxides are formed via an anodization process. Anodization is an electrolytic passivation process in which a metal; acting as an anode of an electrolytic cell, is subjected to an electrolytic oxidation in order to coat with a protective or decorative film in the form of metal oxide. Anodization could be either potentiostatic or galvanostatic: for potentiostatic anodizing, the anodizing voltage is kept constant and the current density vs. time is measured, while in case of galvanostatic anodizing, the current density is kept constant and the anodizing voltage vs. time is measured. The electrolyte composition is the factor that determines whether the film will be barrier or porous. Barrier oxide grows in neutral electrolytic solutions in which the metal oxide is hardly soluble, most commonly ammonium borate, phosphate or tartrate solutions. On the other hand, if acid electrolytes are used, porous oxide grows because oxide not only grows but also dissolves in acidic electrolytes. The most commonly used acidic electrolyte is sulfuric acid, while oxalic acid, phosphoric acid are also used.

Anodic metal oxides have diverse applications such as prevention of corrosion of metal substrates from its environment,[34] capacitor dielectrics,[35,36] templates for synthesis of nanomaterials.[37-39] In addition, they have also been used in many other fields such as optics, electronics and catalysis.[40-43] The best known porous anodic oxide, anodic aluminium oxide (AAO), was first reported several decades ago[44-47] and is now commercially available. AAO membranes are mainly used as filtration membranes.[48,49] They have also been used as template for synthesis of various nanomaterials such as nanowires,[50] nanoparticles[51,52] and nanotubes.[53] Porous anodic oxide films have also been achieved on surfaces of many other metals, sometimes the so-called valve metals, e.g. titanium,[54,55] hafnium,[56] niobium,[57] tantalum,[58] tungsten,[59] vanadium,[60] and zirconium.[61] Through the study described in this dissertation in chapter 4, we have been able to add another name to this list i.e. gallium.

It has been widely accepted that formation of the pores in anodic metal oxides is based on two continuous processes, one is oxide dissolution at the electrolyte/oxide interface and the other

is oxidation of metal at the oxide/metal interface. In fact, the formation mechanism of these pores, often hexagonally ordered, is much more complicated than the normal prediction. Although the formation mechanism, pore ordering, pore size control have been extensively studied[62,63] and many efforts have been made to optimize the anodization conditions for these films,[64-66] there is still much work to do in order to fully understand the electrochemical process during the anodization.

1.2.5.1 Anodic porous alumina

Self-organized anodic porous alumina can be grown by the anodization of aluminum to form a densely-packed, hexagonal array of cylindrical nanopores as shown in **Figure 1.3**. Through the optimization of anodization conditions like electrolyte solution compositions and applied potentials; the pore diameter, density and wall thickness of anodic alumina can be controlled.

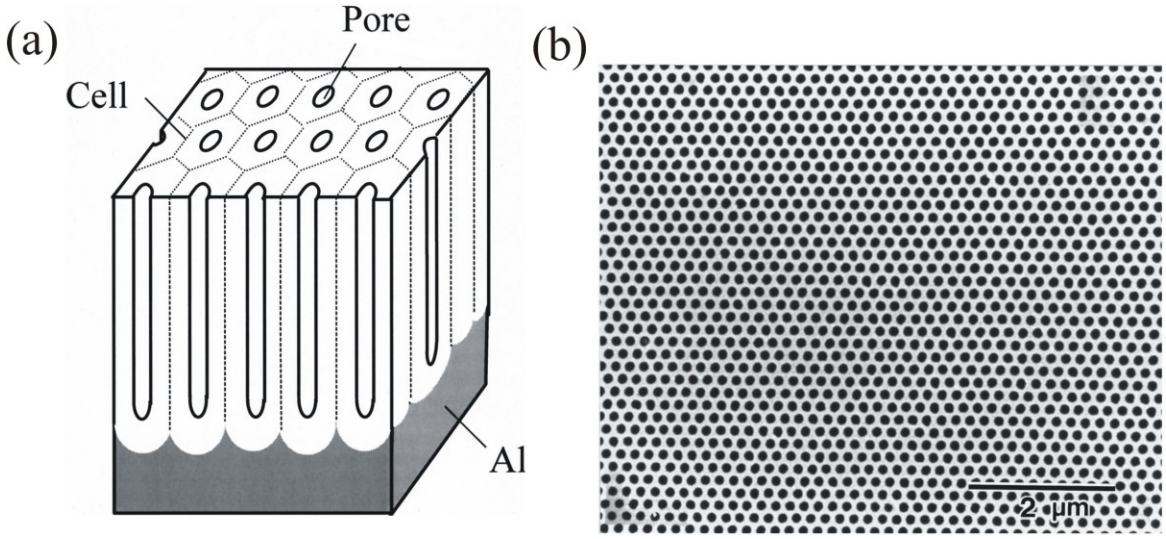

Figure 1.3 (a) Schematic illustration of a nanoporous anodic alumina film formed on aluminum substrate. (b) Typical SEM image of the surface of a nanoporous anodic alumina film. (Reproduced from ref. 73 by permission of The Electrochemical Society, Copyright © 2001.)

Some of the typical conditions used to obtain anodic porous alumina are summarized in **Table 1.1** as shown below with the types of electrolytes and their concentration, the anodizing voltages used together with the hexagonal cell size and the appropriate reference.

Table 1.1 Anodization parameters for various anodizing electrolytes

Electrolyte & Concentration	Anodization Voltage (V)	Hexagonal Cell Size (nm)	Reference
0.5 M H_2SO_4	25-27	65	[67]
0.3 M $H_2C_2O_4$	40	100	[64,68]
0.3 M H_3PO_4	195	500	[69]

Following the brief discussion on anodic porous alumina above, the next few sections will describe the mechanism of nanopore formation, different methods used to improve the pore ordering (2-step method and the pretexturing method), the kinetics of porous oxide growth and the dependence of parameters like pore density, pore spacing and pore diameter on anodizing voltage and electrolyte concentration.

1.2.5.1.1 Mechanisms of Nanoporous Anodic Oxide Formation

The anodic formation of a nanoporous Al_2O_3 layer at acidic pH (**Figure 1.4(a)**) and that of a compact barrier-type layer at neutral to basic pH (**Figure 1.4(b)**) has been previously shown.[70,71]

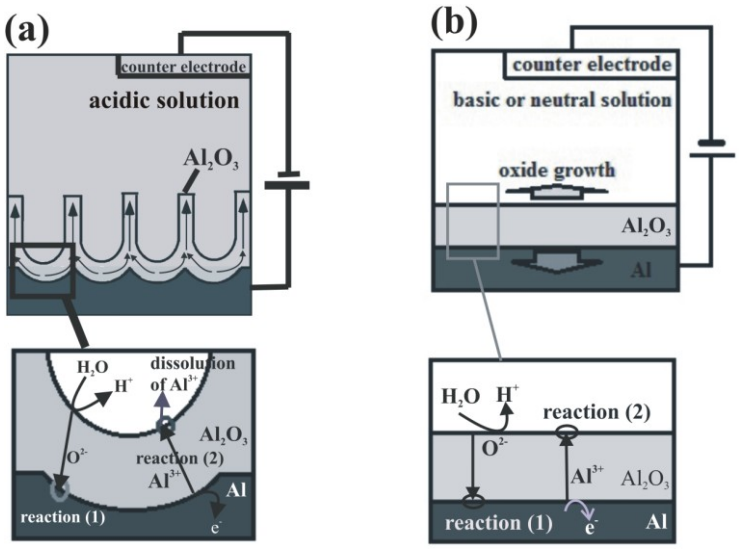

Figure 1.4 Schematic illustrations of (a) anodic nanoporous layer formation and (b) anodic compact barrier-type formation. (Drawn after a reference.[70])

It is important to understand the chemical reactions at oxide/metal and solution/oxide interfaces. It is believed that the anodic oxide layers grow at the oxide/metal and solution/oxide interfaces by the following anodization reactions:[70]

Al_2O_3 formation at the oxide/metal interface: $2Al + 3\ O^{2-} \longrightarrow Al_2O_3 + 6e^-$ (1)

Al_2O_3 formation at the solution/oxide interface: $2Al^{3+} + 3H_2O \longrightarrow Al_2O_3 + 6H^+$ (2)

When electric field is applied, aluminum at the oxide/metal interface will be oxidized into Al^{3+} cations. Some of these cations migrate across the oxide layer and are dissolved into the electrolyte (in case of porous aluminum oxide) or form oxide at the electrolyte/oxide interface (in case of a barrier layer aluminum oxide) as shown in **Figure 1.4**. Some of these cations remain at the oxide/metal interface, forming Al_2O_3 with the oxide anions migrated from the electrolyte/oxide interface. The growth rates of these two interfaces are thus determined by the mobilities of Al^{3+} and O^{2-} within the oxide layer. Because of the larger transport number of O^{2-} (0.56) than that of Al^{3+} (0.44),[70] an Al_2O_3 layer grows more quickly at the oxide/metal interface. In the case of nanoporous Al_2O_3 formation, one more chemical process is essential: field-assisted dissolution of Al^{3+} from the oxide to the solution during anodization (**Figure 1.4(a)**; i.e., the reverse of reaction (2) as shown above). Acidic conditions (e.g. H_2SO_4 (0.1 ~ 8 M), $H_2C_2O_4$ (0.03 ~0.9 M), H_3PO_4 (0.04 ~ 1.1 M)) are required for efficient Al^{3+} dissolution.[70]

1.2.5.1.2 Long-range pore ordering of anodic porous alumina

In anodic alumina, the degree of the ordering of the pores at the surface is low because the pores develop randomly at the initial stage of the anodization. However, when anodization is carried out under predetermined conditions after initiation points have been formed on the aluminium surface, the ordered pores are formed. The improvement of the ordering of the pores has been achieved by either the two-step anodization method[64,68] or the pre-texturing method.[72-74] In the two-step anodization method, the porous alumina layer formed after the first anodization step is dissolved to obtain bottom sections of fine pores as shown in **Figure 1.5(a)**. These fine pores act as an initiation point during the second anodization step leading to well ordered pores. On the other hand, the pre-texturing method uses a mould such as SiC single crystal wafer which has the required mechanical strength and smoothness.[75] An array of shallow concaves is formed on aluminum by imprinting the mould, and these concaves serve as initiation sites for the pore development at the initial stage of the anodization. The anodization of this pre-textured

aluminum gives anodic porous aluminum with long-range ordered pores. The two-step anodization method is cost-effective and is generally the preferred method.

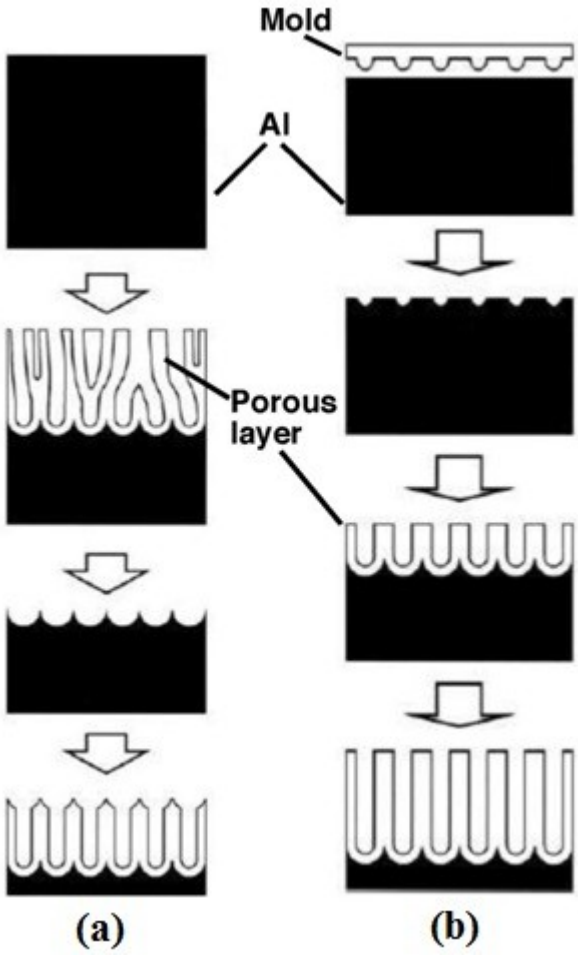

Figure 1.5 Schematic drawing of the preparation of anodic porous alumina with ideally ordered pores using (a) two-step anodization and (b) pretexturing method. (Reproduced from ref. 75 by permission of Springer Science + Business Media, Inc. Copyright © 2005.)

1.2.5.1.3 Pores initiation and porous oxide growth

Several theories exist that explain the porous film growth. Singh et al.[76] attributed the pore initiation and self organization of the porous structures in aluminum oxide films at the initial stage to the significant elastic stress in the oxide layer. The main element of this theory is the Butler-Volmer relation[77] describing an exponential dependence of the current on the overpotential and a dependence of the activation energies of the oxide-electrolyte interfacial reactions on the Laplace pressure and the elastic stress in the oxide layer. In the case when the effect of elastic stress is negligible, a weakly nonlinear analysis leads to formation of spatially

irregular pore arrays that have been observed in experiments. In the case when the effect of elastic stress in the oxide layer is significant, the instability can transform from a long-wave type to a short-wave type. A weakly nonlinear analysis of the short-wave instability shows that it leads to the growth of spatially regular, hexagonally ordered pore arrays.

Vorobyova et al.[78] considered distribution of an applied voltage in three main components of an electrochemical bath system: a growing oxide layer; a Helmholtz layer at electrolyte/oxide interface; and a Gouy–Chapman space charge layer, which extends to the quasi-neutral electrolyte region. It is found that the transformation of the Helmholtz layer is due to self-organization effects in the Gouy–Chapman layer, leading to a growth of highly ordered pores.

Although the principle of the pore ordering has been investigated extensively,[45,47,64,76,78-80] the most commonly accepted model is based on mechanical stress during the oxidation process.[47,81] The ionic density of Al^{3+} in anodic alumina ($3.66\times10^{22}/cm^3$) corresponding to the weight density of approximately 3.1 g/cm^3 [82] is significantly lower than the atomic density of aluminum metal of $6.02\times10^{22}/cm^3$. The mechanical stress coming from volume expansion during oxide formation at the oxide/metal interface could be a possible origin of a repulsive force between neighboring pores. Jessensky et al.[47] proposed that this repulsive force should be accounted for the self-organized formation of hexagonal pore arrays. It was also suggested that neither too large nor too small expansion would result in a long range ordering of the pores. Only a medium volume expansion of 1.2 times from aluminum to alumina, independent of the specific anodization conditions, could lead to an ordering.[83] In case of anodic gallium oxide described in chapter 4 in this dissertation, volume expansion of 1.4 times from gallium to gallium oxide occurs. This value is similar to that for alumina and consequently ordered porous anodic gallium oxide structures were observed.

Thus, it can be concluded that pore initiation and pore growth in anodic oxide formation is still a topic of debate. Different theories have been proposed by different research groups and a common consensus has not been reached. So, this still remains a topic for research and investigation even today.

1.2.5.1.4 Current-time curves

The current-time curve under the constant potential regime for porous anodic alumina is discussed in this section. The *I-t* curves that we obtained for our anodic gallium oxide had a

similar shape and thus the theory described here is quite useful for the discussion of *I-t* curves in chapter 4.

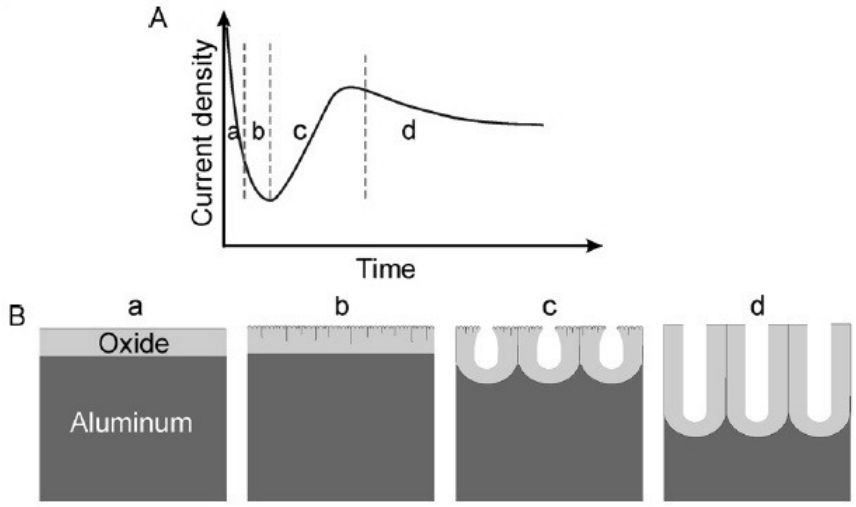

Figure 1.6 Schematic illustration of the kinetics of porous oxide growth in (A) potentiostatic regime, together with (B) stages of anodic porous oxide development. (Reproduced from ref. 70 by permission of Wiley-VCH Verlag GmbH & Co. Copyright © 2008.)

At the start of the process conducted under the constant anodizing potential, current density decrease rapidly with time (**stage a**, **Figure 1.6**) corresponding to a thin barrier oxide film formation, after which a minimum of current density is quickly achieved (**stage b**, **Figure 1.6**) as cracks start to form from surface defects. A linear increase then leads to a local maximum (**stage c**, **Figure 1.6**) indicating the formation of porous oxide as it strives to achieve a dynamic equilibrium between oxide growth and dissolution. After reaching the maximum, the current density decreases slightly and a steady-state growth of the porous oxide proceeds (**stage d**, **Figure 1.6**) to give nanoporous structures of certain thickness.

1.2.5.1.5 Dependence of pore parameter on anodizing voltage and electrolyte concentration

The cell and pore diameter are generally considered to be proportional to the applied voltage. By assuming a hemispherical pore bottom, Parkhutik and Shershulsky[84] established a theoretical model and found that the cell size, R_m, is a linear function of the applied potential U_0. R_m = 2.5 nm/V was calculated for a mild anodization case where the electric field strength across the barrier is about 0.77 V/nm.[85] When large-area hexagonal pore arrays were measured, an interpore distance (D_{int}) = 63 nm was obtained when sulfuric acid (H_2SO_4) was used as

electrolyte and working voltage was 25 V,[83,86] D_{int} = 100 nm for the case when oxalic acid ($H_2C_2O_4$) was used as electrolyte and voltage was 40 V,[64,86] D_{int} = 90-140 nm with an aged sulfuric acid solution, a high anodization potential up to 70 V and a high current density up to 200 mA/cm^2,[87] D_{int} = 220-300 nm with oxalic acid at 110-150 V, [85]D_{int} = 500 nm when using phosphoric acid (H_3PO_4) and applying 195 V.[69,86]

Previous study found that the concentration of the electrolyte does not significantly influence the pore diameter.[45] However, more recently it has been suggested that the pore diameter decreases with decreasing pH of the solution.[84] A decrease in pore diameter with increasing concentration of the acidic electrolyte or decreasing pH can be attributed to the decreasing threshold potential for a field-assisted dissolution of oxide at pore bottoms, resulting in an enhanced rate of anodic oxide formation.[86]

A summary of the influence of anodizing parameters on the pore diameter of an anodic oxide nanostructures formed under potentiostatic conditions is presented schematically in **Figure 1.7** below.

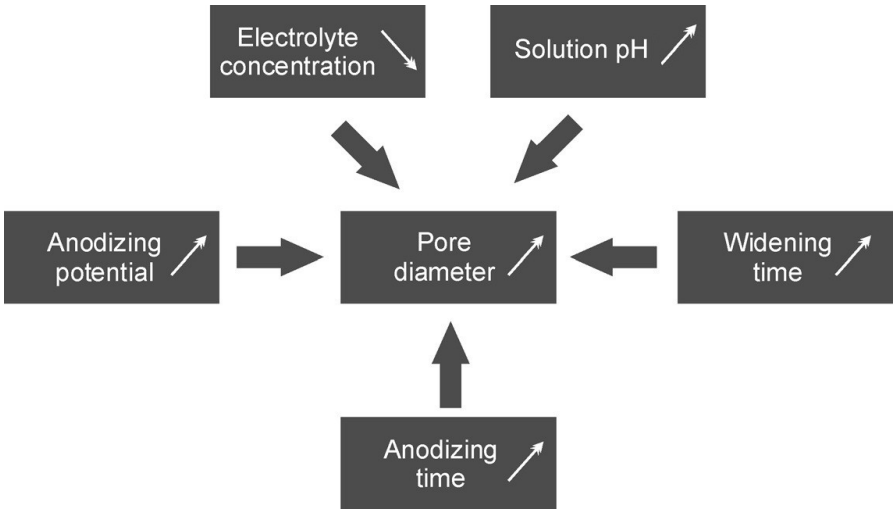

Figure 1.7 The influence of parameters on the pore diameter of nanostructure formed by anodization of aluminum at potentiostatic conditions. (Reproduced from ref. 70 by permission of Wiley-VCH Verlag GmbH & Co. Copyright © 2008.)

1.2.5.2 Anodic titanium oxide

Porous anodic oxide films have also been achieved on the surface of a titanium metal. However, in contrast to anodic aluminum oxide that has a continuous film with an array of pores,

a typical anodic titanium oxide consists of separated nanotubes as shown in **Figure 1.8(a)**. At first, it was difficult to elucidate the formation of gap between the nanotubes. However, the gap formation in the anodic titanium oxide (ATO) has been easier to explain since the discovery of a double layer wall of ATO nanotubes as shown in **Figure 1.8(b)** .[79] Initially, there is no gap between the nanotubes. As shown in **Figure 1.8(c)**, a hydroxide layer forms in between the nanotubes. The density of this layer is lower than that of titania. Thus, when it decomposes into titania, a volume contraction occurs. Depending on the contraction direction, the nanotubes are either separated or form a series of O-rings with a constant distance. If the contraction is perpendicular to the wall, the nanotubes are separated (**Figure 1.8(d)**) while contraction parallel to the wall leads to ridges on the surface of the nanotubes that form a series of O-rings with a constant distance (**Figure 1.8(e)**).

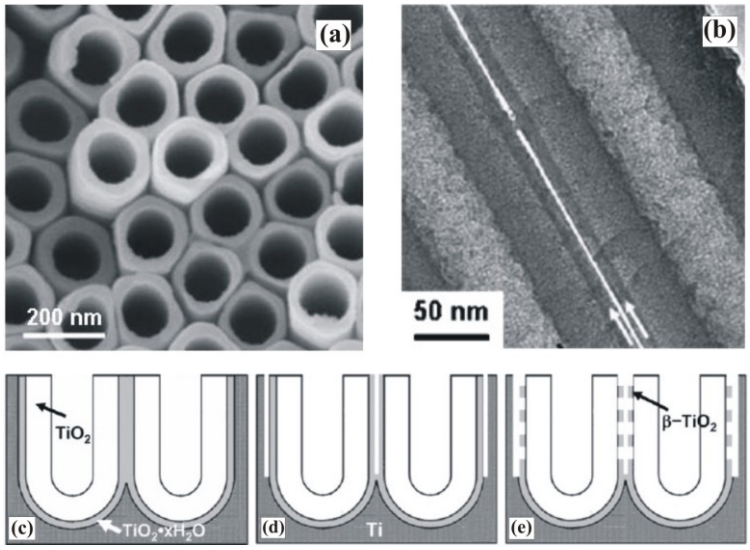

Figure 1.8 (a) Typical top-view SEM image of Anodic Titanium Oxide film. (b) TEM images of the lower part of ATO nanotubes, showing outer layers of titanium hydroxide indicated by two arrows. (c)−(e) Schematics showing the formation of a titanium hydroxide outer layer (c), its partial dehydration into two separated layers (d) and its further dehydration into clusters of titania nanocrystallites. (Reprduced from ref. 79 by permission of Wiley and Sons Inc. Copyright © 2008.)

The anodization of titanium in chromic acid and hydrofluoric acid was reported by Zwilling et al. for the first time in 1999.[88] Since then, great achievements have been made in the fabrication, characterization, formation mechanisms of ATO,[89] and their applications. Many

recent studies have explored applications of anodic titanium oxide nanotubes in photocatalysis,[90,91] gas sensing,[92-95] photoelectrolysis,[42,96,97] and photovoltaics.[43,98-100]

1.2.5.3 Other anodic metal oxides

There are a number of other metals that have been anodized so as to produce self-organized porous oxide films. Hafnium, niobium, tantalum, tungsten, vanadium are some of the other metals that have been anodized to form porous oxides. For these metals, there occurs an optimum volume expansion when the metal is converted to metal oxide during anodization leading to ordered porous structure. To this list of metals forming porous metal oxides upon anodization, one more metal i.e. gallium has been added as will be shown by the study described in this dissertation.

Tsuchiya and Schmuki successfully obtained the self-organized porous hafnium oxide layers via anodization of hafnium at about 50 V in 1 M H_2SO_4 + 0.2 wt% NaF at room temperature.[56] Anodization of niobium has been studied in various electrolytes.[101,102] Self-organized porous anodic niobium oxide films were successfully obtained by Sieber[57] and Karlinsey[103] in 1 M H_2SO_4 + 1 wt% HF and 1.5 wt % HF respectively. Anodization of tantalum in 1 M H_2SO_4 + 2 wt% HF for 2 h after a potential ramp from the open-circuit potential to 20 V with a sweep rate 100 mV/s led to the formation of self-organized porous anodic tantalum oxide with a reasonable narrow size distribution as shown by Sieber et al.[58,104] Nanoporous anodic tungsten oxide was obtained by galvanostatic anodization in oxalic acid by Mukherjee et al., although the regularity of the pores was rather poor.[59] In case of anodization of vanadium, glacial acetic acid with small percentages of water and sodium tetraborate has been found to be the most suitable electrolyte.[105-107] Formation of self-organized porous zirconium oxide layers produced by anodization of Zr at 30 V in an electrolyte of 1 M H_2SO_4 + 0.2 wt% NH_4F has been reported by Tsuchiya et al.[61,108]

The study described in this dissertation shows that anodization of gallium metal in 4 and 6 M H_2SO_4 solution at 10 and 15 V formed nanoporous anodic gallium oxide. The low melting point of gallium made it possible to incorporate gallium inside confined space like the end of a silica capillary. The fact that gallium is in the same group as aluminum made it reasonably easy to hypothesize that the anodization conditions used for aluminum would work for gallium too. Our results suggested that this hypothesis is true. Details on the gallium anodization are presented in chapter 4.

Now that the anodic metal oxides based nanoporous structures have been reviewed, a brief discussion of the property of the gallium metal and its electrochemistry follows. Since this dissertation describes the anodization of gallium metal, it would be worthwhile to briefly introduce gallium metal at this point.

1.3 Gallium and its electrochemistry

Gallium was first discovered by Hans Christian Oersted in 1825. Gallium is a P block, Group 13, Period 4 element. The number of electrons in each of Gallium's shells is 2, 8, 18, 3 and its electronic configuration is [Ar] $3d^{10}$ $4s^2 4p^1$. The gallium atom has a radius of 122.1 pm and its Van der Waals radius is 187 pm. Gallium is not toxic. Besides mercury and cesium, gallium is one of the three elements that naturally occur as a liquid at room temperature (m.p. 29.8 °C).

The low melting point of gallium allows its easy incorporation into micrometer-scale channels.[109-111] Using gallium and eutectic alloy of gallium and indium, Whitesides and his group have been able to fabricate microelectrodes within microfluidic channels[110] as shown in **Figure 1.9**. Charge transfer and rectification in tunneling junctions were studied; the junctions had liquid-metal top-electrodes stabilized in microchannels and ultraflat (template-stripped) bottom electrodes. Dickey and coworkers designed a simple way to fabricate microelectrodes by injecting low melting point alloys, such as eutectic gallium indium into microchannels at room temperature (or just above room temperature).[111] Such electrodes offered mechanical stability over all of the conditions explored (both non-aqueous and aqueous systems).

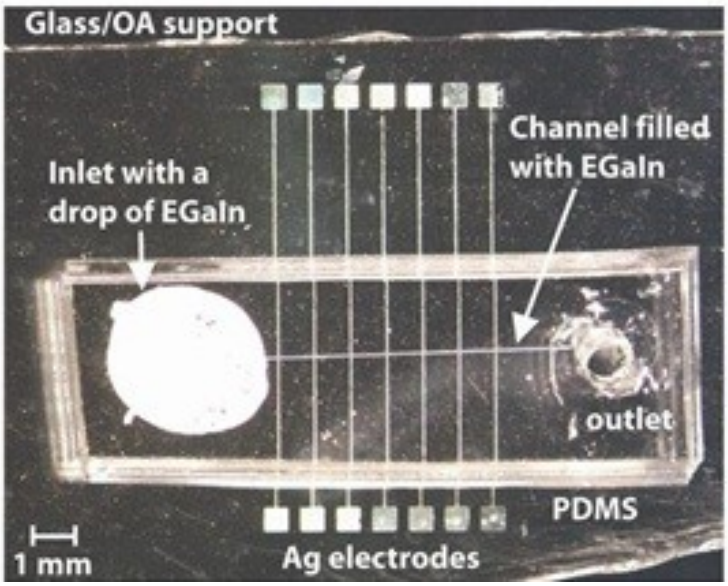

Figure 1.9 Optical micrographs of a microfluidic device that incorporate the eutectic alloy of gallium and indium within the microchannels. (Reproduced from ref. 110 by permission of American Chemical Society, Copyright © 2010)

The fusible nature of gallium aroused interest in us and we have incorporated them inside a silica capillary and studied the anodization of capillary-incorporated gallium as described in chapter 4.

In air, gallium is always coated with a thin oxide film which protects it from further oxidation. From its melting point to 600 °C,[112] gallium is alloyable with several metals. Metals such as platinum, copper, nickel, gold, iron, indium, and mercury readily combine with gallium to form intermetallic compounds and solid solutions. Gallium is fairly rapidly dissolved by strong base, but it is only slowly soluble in refluxed strong mineral acids. The rate of dissolution in mineral acids decreases with increasing metal purity above 99.9%. Aqua regia is probably one of the best solvents for the metal.

The stable oxidation state of gallium is +3, corresponding to solvated Ga^{3+} in acidic solution and $H_2GaO_3^-$, or gallate in alkaline solution. In acidic and basic solutions Ga (III) has a pronounced tendency to form highly structured polynuclear moietes. Depending on the pH value, the trivalent ions Ga^{3+}, $Ga(OH)^{2+}$, GaO^+, GaO_2^-, $H_2GaO_3^-$, $Ga(OH)_4^-$, and $HGaO_3^{2+}$ may exist in equilibrated aqueous solutions. Laubengayer and Schirmer[113] have indicated that compounds of Ga(II) with halides or sulfurs can be obtained. Neogi and Nandi[114] have determined that GaO does not exist, as it is immediately oxidized by water. Sidgwick[115] has denied the existence of

monovalent gallium. Corbett and McMullan[116,117] have however, shown that salts of monovalent gallium can be obtained in alkaline solutions due to its slow oxidation rate to the trivalent state.

The gallium equilibrium electrode potential (reduction half-reaction) was investigated by Regnauld[118] and by Richards and Boyer.[119] Bergkampf[120] reported E^0_{Ga} = -0.520 V (NHE) using the Ga(III) + $3e^-$ = Ga(Hg) couple. The dropping type of electrode was used by Challenger[121] who obtained E^0_{Ga} = -0.577 V (NHE) at 29.78 °C. Saltman and Nachtrieb[122] used the cell $Ga_{sol}/GaCl_3$:HCl/Pt(H_2) to obtain E^0_{Ga} = -0.530 V (NHE), a value adopted by the American Bureau of Standards.

According to the early work of Fricke and Meyring,[123] the forms of the Ga(III) dissociation constants are:

$$GaOH^{2+} = Ga^{3+} + OH^-;\ K = 4 \times 10^{-12} \quad (1.1)$$

$$Ga(OH)_2^+ = Ga(OH)^{2+} + OH^-;\ K = 1.6 \times 10^{-11} \quad (1.2)$$

$$HGaO_3^{2+} = GaO_3^{3-} + H^+;\ K = 2 \times 10^{-12} \quad (1.3)$$

$$H_2GaO_3^- = HGaO_3^{2+} + H^+;\ K = 4.8 \times 10^{-11} \quad (1.4)$$

From these K's and the data of Frickle and Blenke[124] on gallium hydroxide solubility in acids and bases, Porter and Browning[125] estimated the solubility product constants for $Ga(OH)_3$:

$$Ga(OH)_3(s) = Ga^{3+} + 3OH^-;\ K_S = 5 \times 10^{-37} \quad (1.5)$$

The solubility product constant for $Ga(OH)_3$ will be used in chapter 4 to explain the formation as well as dissolution of anodic gallium oxide.

Now that gallium and its electrochemistry have been briefly discussed, the use of metal oxides as pH electrodes will be discussed next. As mentioned earlier, anodic gallium oxide has been studied as a potential sensor material using potentiometric methods. So, literature review on metal oxides based pH electrodes should be very helpful.

1.4 Potentiometric Studies on Metal Oxide Electrodes

For a metal/metal oxide electrode to be useful as a pH sensor, it should satisfy several important criteria.[126] For example, the metal must be noble enough to resist attack by all solutions over a useful pH range, and its oxide must be electrically conducting and be able to come into equilibrium with the solution without appreciable dissolution.[127] As these basic requirements are somewhat difficult to achieve, most of the metal/metal oxide electrodes used

for pH indication represent a trade-off between the nobility of the metal and the stability of the oxide.

There are a considerable amount of studies focused on the development, fabrication and characterization of metal/metal oxide pH electrodes.[128,129] Compared to conventional glass electrodes, the pH electrodes employing metal/metal oxide as sensing materials are typically all-solid-state and offer several advantages. Unlike the glass pH electrodes which require a high input impedance pH meter, the metal oxide-based pH sensor has low electrode impedance. In contrast to the slow response of glass pH electrodes especially in non-aqueous solvents, the solid-state metal oxide pH sensor presents a faster pH response. The slow response of the glass electrode has been attributed to the hygroscopic gel-layer present at the glass surface.[130] The metal-metal oxide electrodes do not have such a layer and equilibrium potential is reached quickly in their case. The method to prepare a metal/metal oxide-based pH electrode is compatible with thin film and microelectromechanical systems (MEMS) manufacturing technologies and provides capability of mass production and miniaturization.

A variety of materials have been explored for use as pH sensing layers that show ideal or near-ideal Nernstian responses. Some examples are IrOx,[131,132] Ru_2O,[133,134] nanoporous PtO_2,[135] RuO_2-TiO_2,[136] TiO_2-PVC,[137] Pd/PdO,[138] Sb/Sb_2O_3,[139] WO_3,[140] PbO_2,[141] Co_3O_4,[142] and SnO_2.[143,144] Among all these pH sensitive oxides, iridium oxide (IrOx) shows high conductivity, good chemical stability, and superior biocompatibility, making it the most popular pH microelectrode material. In addition to IrOx, oxide of antimony has received renewed interest. The glass microelectrodes are difficult to manufacture, especially if a very fine tip is desired for applications such as *in vivo* pH determination. In such cases, antimony can be used as an alternative to the glass electrode. The antimony electrode provides a stable and reproducible means for the determination of intramuscular pH.

Fabrication methods and conditions that determine the structure and composition of iridium oxide affect the pH response characteristics of resultant pH sensors. A comparison between fabrication method and pH sensing characteristics of some typical iridium oxide-based pH electrodes has been made by Madou's group.[145] Marzouk[146] described a modified method to prepare the iridium oxide layer on etched titanium substrate to enhance the stability of the pH sensitive layer. Micro-tip pH electrodes based on iridium oxide on a tapered glass micropipette with a tip of 3−10 μm in diameter[147] and on a carbon fiber[148] have been reported. The iridium

oxide coated glass micropipette electrode has a short response time ranging from 1 to 17 s in the pH range of 4−10 with an accuracy of 0.05 pH. The iridium oxide coated carbon fiber electrode has a fast response time of only 50 ms, and an equilibrium value is reached within 30 s. In a study on a planar thin film iridium oxide-based pH sensor, Ges *et al.*[131] reported ageing effects on IrOx plating solution on the sensor's sensitivity. Iridium oxide films deposited from fresh plating solution showed maximum sensitivity, while those from one-month-old showed decrease of 10-15% in sensitivity.

Yao and coworkers[145] reported a pH electrode based on lithium carbonate melt-oxidized iridium oxide with the composition of $Li_xIrO_y \cdot nH_2O$. The electrode based on this oxide film exhibits promising pH sensing performance and high chemical stability, with an ideal Nernstian response 58.9 mV/pH over the pH range of 1−13. The electrode also shows a fast potential response with a 90% response time less than 0.2 s, and a low open-circuit potential drift of 0.1 mV/day measured in pH 6.6 solution. The reproducibility in terms of the Nernst slopes and the apparent electrode potentials has been improved among electrodes within the same batch.

Although the redox reaction mechanisms of iridium oxide are still not clear, most researchers believe that the proton exchange associated with oxidation states of metal oxides is one of the possible pH sensing mechanisms.[128,131,145,149] During electrochemical reactions, oxidation state changes in the hydrated iridium oxide layer are accompanied by the injection/ejection of H^+. The possible reactions involved in the electrode processes are:

Hydration of iridium oxide

$$Ir_2O_3 + 3H_2O \rightarrow 2Ir(OH)_3 \qquad (1.6)$$

Charge transfer and injection/ejection of hydrogen ion

$$2Ir(OH)_3 \rightarrow 2IrO_2.H_2O + 2H^+ + 2e^- \qquad (1.7)$$

Depending on the fabrication techniques and deposition parameters, the pH sensitive slope of IrOx electrodes varies from near-Nernstian (about 59 mV/pH) to super-Nernstian (about 70 mV/pH or higher). Since the compounds in the oxide layers are possibly mixed in stoichiometry and oxidation states, most reported iridium oxide reactions use *x, y* in the chemical formulas, such as $Ir_2O_3 \cdot xH_2O$. Such mixed oxidation states in IrOx compounds may induce more H^+ ion transfer per electron, which has been attributed to causing super-Nernstian pH responses.[131]

1.5 Dissertation Outline

The dissertation has the following major sections:

Chapter 1− gives a general introduction about the topics covered in this dissertation. It explains the objectives and motivation for the studies performed. This is followed by a brief overview of the self-organized nanoporous materials used. Gallium and its electrochemistry have been briefly explained. Background/literature review discusses the achievements in this field and highlights the unique aspect of the studies performed in this dissertation.

Chapter 2 – describes the analytical techniques and instrumentation used to carry out the studies. These include spectroscopic ellipsometry, cyclic voltammetry, finite element simulation, scanning electron microscopy and potentiometry.

Chapter 3 − an accepted paper, published in *Electrochimica Acta*. This study describes the diffusion of cytochrome c within the nanopores of block copolymer derived recessed nanodisk electrodes (RNEs). We found that cytochrome c molecules could penetrate through the nanopores and reach the underlying bottom electrodes. However, they were more strongly adsorbed onto the smaller RNE nanopores. The results reported in this study will provide guidance in designing RNEs for size-based chemical sensing.

Chapter 4− an accepted paper, published in *Langmuir.* This chapter explains the formation of self-organized nanoporous gallium oxide by anodization of solid gallium metal. The fusible nature of gallium metal allowed its incorporation at the end of a glass capillary. The anodization of the capillary incorporated gallium monolith to form self-organized nanoporous monolith without any cracks or leaks was successfully demonstrated. Nanoporous anodic oxide monoliths formed from a fusible metal will lead to future development of unique devices for chemical sensing and catalysis.

Chapter 5 – manuscript in preparation. In this study, the surface chemical property of the nanoporous anodic gallium oxide, bare planar gallium substrate and barrier layer gallium oxide is explored through potentiometric measurements. The nanoporous anodic and barrier layer gallium oxide structures showed slow potentiometric response only at acidic pH (≤ 4), in contrast to metallic gallium substrates that exhibited a positive potentiometric response to H^+ over the pH range examined (3-10). The potentiometric response at acidic pH probably reflects some chemical processes between gallium oxide and HCl.

Chapter 6 – summarizes the major findings of the studies described in this dissertation. Finally, a general conclusion is presented and possible future research directions are discussed.

References

(1) Guarini, K. W.; Black, C. T.; Milkove, K. R.; Sandstrom, R. L. *J. Vac. Sci. Technol. B* **2001**, *19*, 2784.

(2) Park, M.; Harrison, C.; Chaikin, P. M.; Register, R. A.; Adamson, D. H. *Science* **1997**, *276*, 1401.

(3) Thurn-Albrecht, T.; Schotter, J.; Kastle, C. A.; Emley, N.; Shibauchi, T.; Krusin-Elbaum, L.; Guarini, K.; Black, C. T.; Tuominen, M. T.; Russell, T. P. *Science* **2000**, *290*, 2126.

(4) Kim, H. C.; Jia, X. Q.; Stafford, C. M.; Kim, D. H.; McCarthy, T. J.; Tuominen, M.; Hawker, C. J.; Russell, T. P. *Adv. Mater.* **2001**, *13*, 795.

(5) Crossland, E. J. W.; Ludwigs, S.; Hillmyer, M. A.; Steiner, U. *Soft Matter* **2007**, *3*, 94.

(6) Zhang, Q. L.; Xu, T.; Butterfield, D.; Misner, M. J.; Ryu, D. Y.; Emrick, T.; Russell, T. P. *Nano Lett.* **2005**, *5*, 357.

(7) Yang, S. Y.; Ryu, I.; Kim, H. Y.; Kim, J. K.; Jang, S. K.; Russell, T. P. *Adv. Mater.* **2006**, *18*, 709.

(8) Castelletto, V.; Hamley, I. W. *Curr. Opin. Solid State Mater. Sci.* **2004**, *8*, 426.

(9) Lee, J. S.; Hirao, A.; Nakahama, S. *Macromolecules* **1988**, *21*, 274.

(10) Lee, J. S.; Hirao, A.; Nakahama, S. *Macromolecules* **1989**, *22*, 2602.

(11) Hedrick, J.; Labadie, J.; Russell, T.; Hofer, D.; Wakharker, V. *Polymer* **1993**, *34*, 4717.

(12) Mansky, P.; Chaikin, P.; Thomas, E. L. *J. Mater. Sci.* **1995**, *30*, 1987.

(13) Mansky, P.; Harrison, C. K.; Chaikin, P. M.; Register, R. A.; Yao, N. *Appl. Phys. Lett.* **1996**, *68*, 2586.

(14) Liu, G. J.; Ding, J. F.; Guo, A.; Herfort, M.; BazettJones, D. *Macromolecules* **1997**, *30*, 1851.

(15) Hashimoto, T.; Tsutsumi, K.; Funaki, Y. *Langmuir* **1997**, *13*, 6869.

(16) Harrison, C.; Park, M.; Chaikin, P. M.; Register, R. A.; Adamson, D. H. *J. Vac. Sci. Technol. B* **1998**, *16*, 544.

(17) Thurn-Albrecht, T.; Steiner, R.; DeRouchey, J.; Stafford, C. M.; Huang, E.; Bal, M.; Tuominen, M.; Hawker, C. J.; Russell, T. *Adv. Mater.* **2000**, *12*, 787.

(18) Park, M.; Chaikin, P. M.; Register, R. A.; Adamson, D. H. *Appl. Phys. Lett.* **2001**, *79*, 257.

(19) Hamley, I. W. In *Developments in Block Copolymer Science and Technology*; John Wiley & Sons, Ltd: Chichester, UK, 2004, p 1.

(20) Li, M. Q.; Coenjarts, C. A.; Ober, C. K. *Adv. Polym. Sci.* **2005**, *190*, 183.

(21) Fasolka, M. J.; Mayes, A. M. *Annu. Rev. Mater. Res.*, *31*, 323.

(22) Hillmyer, M. A. *Adv. Polym. Sci.* **2005**, *190*, 137.

(23) Olson, D. A.; Chen, L.; Hillmyer, M. A. *Chem. Mater.* **2008**, *20*, 869.

(24) Mercier, L.; Pinnavaia, T. J. *Adv. Mater.* **1997**, *9*, 500.

(25) Li, Y.; Ito, T. *Langmuir* **2008**, *24*, 8959.

(26) Li, Y.; Ito, T. *Anal. Chem.* **2009**, *81*, 851.

(27) Nuxoll, E. E.; Hillmyer, M. A.; Wang, R.; Leighton, C.; Siegel, R. A. *Acs Appl. Mater. Interfaces* **2009**, *1*, 888.

(28) Darling, S. B.; Yufa, N. A.; Cisse, A. L.; Bader, S. D.; Sibener, S. J. *Adv. Mater.* **2005**, *17*, 2446.

(29) Darling, S. B. *Surf. Sci.* **2007**, *601*, 2555.

(30) Zhang, Q. L.; Gupta, S.; Emrick, T.; Russell, T. P. *J. Am. Chem. Soc.* **2006**, *128*, 3898.

(31) Jeoung, E.; Galow, T. H.; Schotter, J.; Bal, M.; Ursache, A.; Tuominen, M. T.; Stafford, C. M.; Russell, T. P.; Rotello, V. M. *Langmuir* **2001**, *17*, 6396.

(32) Li, Y.; Maire, H. C.; Ito, T. *Langmuir* **2007**, *23*, 12771.

(33) Ibrahim, S.; Ito, T. *Langmuir* **2010**, *26*, 2119.

(34) Bengough, G. D.; Sutton, H. The Protection of Aluminum and its Alloys Against Corrosion by Anodic Oxidation. *Engineering: An Illustrated Weekly Journal* [Online Early Access]. Published Online: 1926.

(35) Jason, A. C.; Wood, J. L. Some Electrical Effects of the Adsorption of Water Vapor by Anodized Aluminum. *Proc. Phys. Soc. B* [Online Early Access]. Published Online: 1955.

(36) Dell'Oka, C. J.; Pulfrey, D. L.; Young, L. *Physics of Thin Films*; Academic Press: New York, 1971; Vol. 6.

(37) Liang, J. Y.; Chik, H.; Yin, A. J.; Xu, J. *J. Appl. Phys.* **2002**, *91*, 2544.

(38) Li, J.; Papadopoulos, C.; Xu, J. M.; Moskovits, M. *Appl. Phys. Lett.* **1999**, *75*, 367.

(39) Li, J.; Papadopoulos, C.; Xu, J. *Nature* **1999**, *402*, 253.

(40) Basu, S.; Chatterjee, S.; Saha, M.; Bandyopadhay, S.; Mistry, K. K.; Sengupta, K. *Sensor Actuat. B-Chem.* **2001**, *79*, 182.

(41) Yang, B. C.; Uchida, M.; Kim, H. M.; Zhang, X. D.; Kokubo, T. *Biomaterials* **2004**, *25*, 1003.

(42) Mor, G. K.; Shankar, K.; Paulose, M.; Varghese, O. K.; Grimes, C. A. *Nano Lett.* **2005**, *5*, 191.

(43) Mor, G. K.; Shankar, K.; Paulose, M.; Varghese, O. K.; Grimes, C. A. *Nano Lett.* **2006**, *6*, 215.

(44) Keller, F.; Hunter, M. S.; Robinson, D. L. *J. Electrochem. Soc.* **1953**, *100*, 411.

(45) O'Sullivan, J. P.; Wood, G. C. *Proc. Roy. Soc. Lond. A* **1970**, *317*, 511.

(46) Thompson, G. E.; Furneaux, R. C.; Wood, G. C.; Richardson, J. A.; Goode, J. S. *Nature* **1978**, *272*, 433.

(47) Jessensky, O.; Müller, F.; Gösele, U. *Appl. Phys. Lett.* **1998**, *72*, 1173.

(48) Lee, S. B.; Mitchell, D. T.; Trofin, L.; Nevanen, T. K.; Soderlund, H.; Martin, C. R. *Science* **2002**, *296*, 2198.

(49) Mitchell, D. T.; Lee, S. B.; Trofin, L.; Li, N. C.; Nevanen, T. K.; Soderlund, H.; Martin, C. R. *J. Am. Chem. Soc.* **2002**, *124*, 11864.

(50) Yi, J. B.; Pan, H.; Lin, J. Y.; Ding, J.; Feng, Y. P.; Thongmee, S.; Liu, T.; Gong, H.; Wang, L. *Adv. Mater.* **2008**, *20*, 1170.

(51) Guo, Y. G.; Hu, J. S.; Liang, H. P.; Wan, L. J.; Bai, C. L. *Chem. Mater.* **2003**, *15*, 4332.

(52) Wang, G.; Shi, C.; Zhao, N.; Du, X. *Mater. Lett.* **2007**, *61*, 3795.

(53) Sui, Y. C.; Acosta, D. R.; Gonzalez-Leon, J. A.; Bermudez, A.; Feuchtwanger, J.; Cui, B. Z.; Flores, J. O.; Saniger, J. M. *J. Phys. Chem. B* **2001**, *105*, 1523.

(54) Macak, J. M.; Tsuchiya, H.; Schmuki, P. *Angew. Chem. Int. Ed.* **2005**, *44*, 2100.

(55) Paulose, M.; Shankar, K.; Yoriya, S.; Prakasam, H. E.; Varghese, O. K.; Mor, G. K.; Latempa, T. A.; Fitzgerald, A.; Grimes, C. A. *J. Phys. Chem. B* **2006**, *110*, 16179.

(56) Tsuchiya, H.; Schmuki, P. *Electrochem. Comm.* **2005**, *7*, 49.

(57) Sieber, I.; Hildebrand, H.; Friedrich, A.; Schmuki, P. *Electrochem. Comm.* **2005**, *7*, 97.

(58) Sieber, I.; Kannan, B.; Schmuki, P. *Electrochem. Solid-State Lett.* **2005**, *8*, J10.

(59) Mukherjee, N.; Paulose, M.; Varghese, O. K.; Mor, G. K.; Grimes, C. A. *J. Mater. Res.* **2003**, *18*, 2296.

(60) Stefanovich, G. B.; Pergament, A. L.; Velichko, A. A.; Stefanovich, L. A. *J. Phys.: Condens. Matter* **2004**, *16*, 4013.

(61) Tsuchiya, H.; Macak, J. M.; Sieber, I.; Schmuki, P. *Small* **2005**, *1*, 722.

(62) Hoar, T. P.; Mott, N. F. *J. Phys. Chem. Solids* **1959**, *9*, 97.

(63) Heber, K. V. *Electrochim. Acta* **1978**, *23*, 127.

(64) Masuda, H.; Fukuda, K. *Science* **1995**, *268*, 1466.

(65) Masuda, H.; Yosuya, M.; Ishida, M. *Jpn. J. Appl. Phys.* **1998**, *37*, 1090.

(66) Macak, J. M.; Tsuchiya, H.; Taveira, L.; Aldabergerova, S.; Schmuki, P. *Angew. Chem. Int. Ed.* **2005**, *44*, 7463.

(67) Masuda, H.; Hasegwa, F.; Ono, S. *J. Electrochem. Soc.* **1997**, *144*, L127.

(68) Masuda, H.; Satoh, M. *Jpn. J. Appl. Phys.* **1996**, *35*, L126.

(69) Masuda, H.; Yada, K.; Osaka, A. *Jpn. J. Appl. Phys.* **1998**, *37*, L1340.

(70) Sulka, G. D. In *Nanostructured Materials in Electrochemistry*; Eftekhari, A., Ed.; Wiley-VCH Verlag GmbH & Co: Weinheim, 2008, p 1.

(71) Diggle, J. W.; Downie, T. C.; Goulding, C. W. *Chem. Rev.* **1969**, *69*, 365.

(72) Masuda, H.; Yamada, H.; Satoh, M.; Asoh, H.; Nakao, M.; Tamamura, T. *Appl. Phys. Lett.* **1997**, *71*, 2770.

(73) Asoh, H.; Nishio, K.; Nakao, M.; Tamamura, T.; Masuda, H. *J. Electrochem. Soc.* **2001**, *148*, B152.

(74) Asoh, H.; Nishio, K.; Nakao, M.; Yokoo, A.; Tamamura, T.; Masuda, H. *J. Vac. Sci. Technol. B* **2001**, *19*, 569.

(75) Masuda, H. In *Ordered Porous Nanostructures and Applications*; Wehrspohn, R. B., Ed.; Springer Science+Business Media, Inc.: New York, 2005, p 37.

(76) Singh, G. K.; Golovin, A. A.; Aranson, I. S. *Phys. Rev. B* **2006**, *73*.

(77) Bard, A. J.; Faulkner, L. R. *Electrochemical Methods: Fundamentals and Applications*; 2nd ed.; Wiley: New York, 2001.

(78) Vorobyova, A. I.; Outkina, E. A.; Khodin, A. A. *Russian Microelectronics* **2007**, *36*, 384.

(79) Su, Z.; Zhou, W. *Adv. Mat.* **2008**, *20*, 3663.

(80) Yuzhakov, V. V.; Chang, H. C.; Miller, A. E. *Phys. Rev. B* **1997**, *56*, 12608.

(81) Garcia-Vergara, S. C.; Igleasia-Rubianes, L.; Blanco-Pinzon, C. E.; Skeldon, P.; Thompson, G. E.; Campestrini, P. *Proc. R. Soc. A* **2006**, *462*, 2345.

(82) Skeldon, P.; Shimizu, K.; Thompson, G. E.; Wood, G. C. *Surf. Interface Anal.* **1983**, *5*, 247.

(83) Li, A. P.; Müller, F.; Birner, A.; Nielsch, K.; Gösele, U. *J. Appl. Phys.* **1998**, *84*, 6023.

(84) Parkhutik, V. P.; Shershulsky, V. I. *J. Phys. D: Appl. Phys.* **1992**, *25*, 1258.

(85) Lee, W.; Ji, R.; Gösele, U.; Nielsch, K. *Nature Mater.* **2006**, *5*, 741.

(86) Nielsch, K.; Choi, J.; Schwirn, K.; Wehrspohn, R. B.; Gosele, U. *Nano Lett.* **2002**, *2*, 677.

(87) Chu, S. Z.; Wada, K.; Inoue, S.; Isogai, M.; Yasumori, A. *Adv. Mater.* **2005**, *17*, 2115.

(88) Zwilling, V.; Aucouturier, M.; Darque-Ceretti, E. *Electrochim. Acta* **1999**, *45*, 921.

(89) Mor, G. K.; Varghese, O. K.; Paulose, M.; Shankar, K.; Grimes, C. A. *Sol. Energy Mater. Sol. Cells* **2006**, *90*, 2011.

(90) Adachi, M.; Murata, Y.; Harada, M.; Yoshikawa, S. *Chem. Lett.* **2000**, 942.

(91) Chu, S. Z.; Inoue, S.; Wada, K.; Li, D.; Haneda, H.; Awatsu, S. *J. Phys. Chem. B* **2003**, *107*, 6586.

(92) Varghese, O. K.; Gong, D. W.; Paulose, M.; Ong, K. G.; Dickey, E. C.; Grimes, C. A. *Adv. Mater.* **2003**, *15*, 624.

(93) Mor, G. K.; Carvalho, M. A.; Varghese, O. K.; Pishko, M. V.; Grimes, C. A. *J. Mater. Res.* **2004**, *19*, 628.

(94) Varghese, O. K.; Mor, G. K.; Grimes, C. A.; Paulose, M.; Mukherjee, N. *J. Nanosci. Nanotech.* **2004**, *4*, 733.

(95) Paulose, M.; Varghese, O. K.; Mor, G. K.; Grimes, C. A.; Ong, K. G. *Nanotech.* **2006**, *17*, 398.

(96) Mor, G. K.; Shankar, K.; Varghese, O. K.; Grimes, C. A. *J. Mater. Res.* **2004**, *19*, 2989.

(97) Varghese, O. K.; Paulose, M.; Shankar, K.; Mor, G. K.; Grimes, C. A. *J. Nanosci. Nanotech.* **2005**, *5*, 1158.

(98) Uchida, S.; Chiba, R.; Tomiha, M.; Masaki, N.; Shirai, M. *Electrochem.* **2002**, *70*, 418.

(99) Adachi, M.; Murata, Y.; Okada, I.; Yoshikawa, S. *J. Electrochem. Soc.* **2003**, *150*, G488.

(100) Paulose, M.; Shankar, K.; Varghese, O. K.; Mor, G. K.; Hardin, B.; Grimes, C. A. *Nanotech.* **2006**, *17*, 1446.

(101) D'Alkaine, C. V.; de Souza, L. M. M.; Nart, F. C. *Corros. Sci.* **1993**, *34*, 109.

(102) Young, L. *Anodic Oxide Films*; Academic Press: London, 1961.

(103) Karlinsey, R. L. *Electrochem. Commun.* **2005**, *7*, 1190.

(104) Sieber, I. V.; Schmuki, P. *J. Electrochem. Soc.* **2005**, *152*, C639.

(105) Keil, R. G. *J. Electrochem. Soc.* **1965**, *112*, 643.

(106) Keil, R. G.; Salomon, R. E. *J. Electrochem. Soc.* **1968**, *115*, 628.

(107) Ellis, B. H.; Hopper, M. A.; Desmet, D. J. *J. Electrochem. Soc.* **1971**, *118*, 860.

(108) Tsuchiya, H.; Schmuki, P. *Electrochem. Commun.* **2004**, *6*, 1131.

(109) Dickey, M. D.; Chiechi, R. C.; Larsen, R. J.; Weiss, E. A.; Weitz, D. A.; Whitesides, G. M. *Adv. Funct. Mater.* **2008**, *18*, 1097.

(110) Nijhuis, C. A.; Reus, W. F.; Barber, J. R.; Dickey, M. D.; Whitesides, G. M. *Nano Lett.* **2010**, *10*, 3611.

(111) So, J.-H.; Dickey, M. D. *Lab Chip* **2011**, *11*, 905.

(112) Dymov, A. M.; Savostin, A. P. *Analytical Chemistry of Gallium*; Ann Arbor Science Publishers: Ann Arbor, Michigan, 1970.

(113) Laubengayer, A. N.; Schirmer, F. B. *J. Am. Chem. Soc.* **1940**, *62*, 1578.

(114) Neogi, P.; Nandi, S. K. *J. Ind. Chem. Soc.* **1936**, *13*.

(115) Sidgwick, N. N. *Z. Anorg. Allg. Chem.* **1932**, *203*, 23.

(116) Corbett, J. D.; McMullan, R. K. *J. Am. Chem. Soc.* **1955**, *77*, 4217.

(117) Corbett, J. D.; McMullan, R. K. *J. Am. Chem. Soc.* **1956**, *78*, 2906.

(118) Regnauld, J. *C. R. Acad. Sci.* **1878**, *86*, 577.

(119) Richards, T. W.; Boyer, S. *J. Am. Chem. Soc.* **1919**, *41*, 133.

(120) Bergkampf, S. v. *Z. Anal. Chem.* **1932**, *90*, 338.

(121) Challenger, G., Harvard, 1945.

(122) Saltman, W. H.; Nachtrieb, N. H. *J. Electrochem. Soc.* **1953**, *100*, 126.

(123) Fricke, R.; Meyring, K. *Z. Anorg. Allg. Chem.* **1928**, *176*, 325.

(124) Fricke, R.; Blencke, W. *Z. Anorg. Allg. Chem.* **1925**, *143*, 184.

(125) Porter, L. F.; Browning, P. E. *J. Am. Chem. Soc.* **1919**, *41*, 1491.

(126) Ives, D. J. G.; Janz, G. J. *Reference Electrodes*; Academic Press: New York, 1969.

(127) Glab, S.; Hulanicki, A.; Edwall, G.; Ingman, F. *Crit. Rev. Anal. Chem.* **1989**, *21*, 29.

(128) Fog, A.; Buck, R. P. *Sens. Actuators* **1984**, *5*, 137.

(129) Kreider, K. G.; Tarlov, M. J.; Cline, J. P. *Sens. Actuators B* **1995**, *28*, 167.

(130) Izutsu, K.; Yamamoto, H. *Anal. Sci.* **1996**, *12*, 905.

(131) Ges, I. A.; Ivanov, B. L.; Schaffer, D. K.; Lima, E. A.; Werdich, A. A.; Baudenbacher, F. J. *Biosens. Bioelectron.* **2005**, *21*, 248.

(132) Hitchman, M. L.; Ramanathan, S. *Analyst* **1988**, *113*, 35.

(133) Koncki, R.; Mascini, M. *Anal. Chim. Acta* **1997**, *351*, 143.

(134) Vonau, W.; Enseleit, U.; Gerlach, F.; Herrmann, S. *Electrochim. Acta* **2004**, *49*, 3745.

(135) Park, S.; Boo, H.; Kim, Y.; Han, J. H.; Kim, H. C.; Chung, T. D. *Anal. Chem.* **2005**, *77*, 7695.

(136) Pocrifka, L. A.; Gonclaves, C.; Grossi, P.; Colpa, P. C.; Pereira, E. C. *Sens. Actuators B* **2006**, *113*, 1012.

(137) Gac, A.; Atkinson, J. K.; Zhang, Z.; Sexton, C. J.; Lewis, S. M.; Please, C. P.; Sion, R. *Microelectronics Int.* **2004**, *21*, 44.

(138) Liu, C. C.; Bocchicchio, B. C.; Overmyer, P. A.; Neuman, M. R. *Science* **1980**, *207*, 188.

(139) Jones, R. D.; Neuman, M. R.; Sanders, G.; Cross, F. S. *Ann. Thoracic Surg.* **1982**, *33*, 491.

(140) Yamamoto, K.; Shi, G. Y.; Zhou, T. S.; Xu, F.; Zhu, M.; Liu, M.; Kato, T.; Jin, J. Y.; Jin, L. T. *Anal. Chim. Acta* **2003**, *480*, 109.

(141) Eftekhari, A. *Sens. Actuators B.* **2003**, *88*, 234.

(142) Li, Q. W.; Luo, G. A.; Shu, Y. Q. *Anal. Chim. Acta* **2000**, *409*, 137.

(143) Pan, C. W.; Chou, J. C.; Sun, T. P.; Hsiung, S. K. *Sens. Actuators B.* **2005**, *108*, 870.

(144) Tsai, C. N.; Chou, J. C.; Sun, T. P.; Hsiung, S. K. *Sens. Actuators B.* **2005**, *108*, 877.

(145) Yao, S.; Wang, M.; Madou, M. *J. Electrochem. Soc.* **2001**, *148*, H29.

(146) Marzouk, S. A. M. *Anal. Chem.* **2003**, *75*, 1258.

(147) Bezbaruah, A. N.; Zhang, T. C. *Anal. Chem.* **2002**, *74*, 5726.

(148) Wipf, D. O.; Ge, F. Y.; Spaine, T. W.; Bauer, J. E. *Anal. Chem.* **2000**, *72*, 4921.

(149) Papeschi, G.; Merigliano, S.; Zaninotto, G.; Baessato, M.; Ancona, E.; Larini, M. *J. Med. Eng. Technol.* **1984**, *8*, 221.

Chapter 2 - Analytical Techniques used in the Characterization of Nanoporous Materials

This chapter discusses the analytical techniques used for characterization of the nanoporous materials prepared to carry out this research. The nanoporous materials were characterized via spectroscopic methods, electrochemical methods and microscopic methods. Spectroscopic ellipsometry was used to measure the thickness of PS-*b*-PMMA films spin coated on gold coated Si wafers. Energy Dispersive X-ray Spectroscopy (EDX) was used to assess the surface elemental composition of the anodic gallium oxide. Among the electrochemical methods, cyclic voltammetry and potentiometry were used. Cyclic Voltammetry was used in assessing the active surface area of the electrodes fabricated from PS-*b*-PMMA nanoporous films on gold substrate. In addition, CV was used to study the diffusion modes of redox molecules like 1.1' ferrocenedimethanol and cytochrome c inside the nanoporous structures. Potentiometric methods were employed to study the use of gallium oxide as a sensor material. Scanning Electron Microscopy (SEM) was used to assess the surface morphology of the anodic gallium oxide structures.

2.1 Spectroscopic Ellipsometry[1-3]

Ellipsometry is a non-destructive and contactless technique used for measuring the thickness and refractive index of a thin film on a solid surface. Thin films having thickness ranging from a few tens of nanometer to ca. 10 μm can be measured accurately and quickly with this method. In ellipsometry, the state of polarization of light reflecting from a surface is analyzed and using the laws of electromagnetism (specifically, Maxwell's equations), the thickness and refractive index of the nanofilm is determined.

Ellipsometry involves the reflection of light from a surface or the interface between two mediums. Let us consider a model reflective surface coated with a nanofilm of thickness d (**Figure 2.1**). In this model system, several phenomena occur at the interface when light passes from one medium to a second medium. Some of the light is reflected from the surface and some enters the second medium. When a linearly polarized light reflects off a surface, a phase shift occurs in both the parallel and perpendicular components (i.e., the s- and p-polarized components).

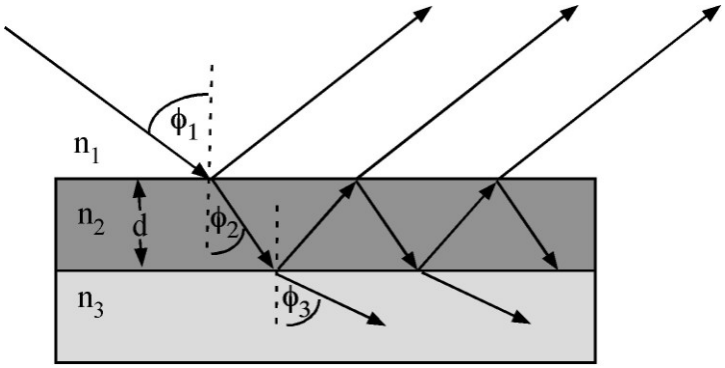

Figure 2.1 The reflection, refraction, and transmission of light through a model multiple interface system. The n_i represents the refractive index of each phase.

There may also be an amplitude difference between incident and reflected beams in both components. In fact, the amplitude difference and phase shift are usually not the same for both components. Thus, the reflected beam is elliptically polarized. The ellipticity depends on the optical properties of the substrate (reflecting surface) as well as the optical properties and thickness of any overlying films. One optical property of importance is the refractive index (RI), also denoted as n.

In order to understand how ellipsometry is used to obtain thickness values for thin nanofilm, optical parameters Del (Δ) and Psi (ψ) need to be understood. The optical parameter Del (Δ) is defined as the phase difference between the p-polarized and s-polarized components of the incident light upon reflection. In other words, Δ is the resulting change in the phase difference between the s and p waves as the light is reflected from the sample as described by equation 2.1.

$$\Delta = \delta_1 - \delta_2 \tag{2.1}$$

where δ_1 and δ_2 are the phase difference between the p-polarized component and the s-polarized component of the incident light and the reflected light respectively. The second fundamental ellipsometric optical parameter Psi (ψ) is defined as the angle whose tangent is the ratio of the magnitudes of the total reflection coefficients as given by equation 2.2.

$$\tan\psi = \frac{\left|R^p\right|}{\left|R^s\right|} \tag{2.2}$$

An additional complex quantity ρ can be defined as the ratio of the total reflection coefficients as shown in equation 2.3.

$$\rho = \frac{R^p}{R^S} \tag{2.3}$$

Combining the three equations, the fundamental equation of ellipsometry can be obtained:

$$\rho = \frac{R^p}{R^s} = \tan\psi e^{i\Delta} \tag{2.4}$$

Δ and ψ are the experimental quantities measured by the ellipsometer and fitted to a computer model to yield refractive index and film thickness.

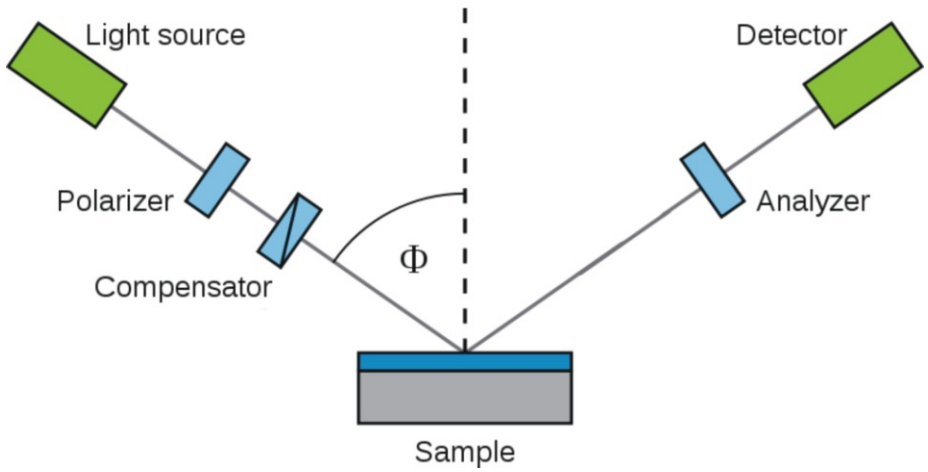

Figure 2.2 Schematic Diagram of a Polarizer-Compensator-Analyzer-Detector type ellipsometer.

Figure 2.2 shows the components of an ellipsometer which has a polarizer-compensator-sample-analyzer-detector configuration. The light source emits an incident light beam with a known polarization state on the sample. According to the properties of the sample, the polarization of the incident beam is changed. The detector detects the change in polarization of the reflected beam of light and experimental results are expressed as Δ and ψ parameters.

In spectroscopic ellipsometry, Psi and Delta values are acquired as a function of wavelength. After an ellipsometric spectrum is generated for the film, a model layer is created and fitting with the ellipsometric spectrum performed to extract parameters such as film thickness and refractive index of the material. The thickness of the PS-*b*-PMMA film was determined by adding a Cauchy layer on top of the artificial layer on Au. For the fitting, the

Cauchy model which gives the empirical relationship between refractive index and wavelength was used

$$n = A + \frac{B}{\lambda^2} + \frac{C}{\lambda^4} \tag{2.5}$$

where n is the refractive index, λ (μm) is the wavelength, A, B and C are coefficients that can be determined for a material by fitting the equation to measured refractive indices at known wavelengths.

Using an iterative procedure, unknown optical constants and/or the coefficients shown above are varied, and Δ and ψ parameters are calculated. The desired film parameters are obtained when the calculated and experimental data match with a minimized mean square error.

2.2 Energy-Dispersive X-ray Spectroscopy[4]

Energy-dispersive X-ray spectroscopy (EDS or EDX) is an analytical technique used for the chemical characterization of a sample. In other words, EDS gives information about the elemental composition and their relative proportions (atomic % for example). The fundamental principle that each element has a unique atomic structure allowing unique set of peaks on its X-ray spectrum governs the characterization capability of EDS. X-rays produced by a sample placed in an electron beam are detected in EDS measurements. The electron beam excites the atoms in the sample that subsequently produce X-rays to discharge the excess energy. The energy of the X-rays is characteristics of the atoms that produced them, forming peaks in the spectrum. The number and energy of the X-rays emitted from a specimen is measured by energy-dispersive spectrometer.

EDS is used in conjunction with scanning electron microscopy (SEM). EDS analysis usually involves the generation of an X-ray spectrum from the entire scan area of the SEM. The EDS spectrum itself shows the counts (number of X-rays received and processed) on the y-axis while the x-axis shows the energy level of those counts. Generally, the EDS software is capable of associating the energy level of the X-rays with the elements and shell level that generated them.

EDS can provide rapid qualitative, or with adequate standards, quantitative analysis of elemental composition with a sampling depth of 1-2 microns. X-rays can also be used to form maps or line profiles, showing the elemental distribution in a sample surface. The accuracy of EDS spectrum can be affected by various factors. Many elements will have overlapping peaks

(e.g., Mn K_β and Fe K_α) and thus EDS spectra may not be so accurate. The nature of the sample also affects the accuracy. The likelihood of an X-ray escaping the specimen, and thus being able to detect and measure, depends on the energy of the X-ray and the amount and density of material it has to pass through. This can result in reduced accuracy especially in non-homogeneous and rough samples. The elemental composition of nanoporous gallium oxide as described in chapter 4 was qualitatively determined using EDS.

2.3 Cyclic Voltammetry[5-8]

2.3.1 General principles

Cyclic voltammetry (CV) is a potential sweep method, where potential is changed as a linear function of time, to obtain a current-potential (*i-E*) curve. Cyclic voltammetry is generally used for examining the electrochemical properties of a chemical substance or material. This technique is very helpful in explaining the reversibility of a reaction, diffusion/adsorption of an analyte to the electrode surface, diffusion coefficient (D_0) for a reactant, and estimation of the number of electrons involved in the electrode reaction i.e. n. A unique aspect of this technique is the three electrodes used, which consist of a working electrode, a reference electrode, and a counter electrode. In CV, potential between the working and the reference electrode is controlled and current passed between the working and the counter electrode is measured. Electrolyte is generally added to the test solution to ensure sufficient conductivity. **Figure 2.3** is a typical CV obtained for a reversible one electrode reaction: $O + e^- \leftrightarrows R$

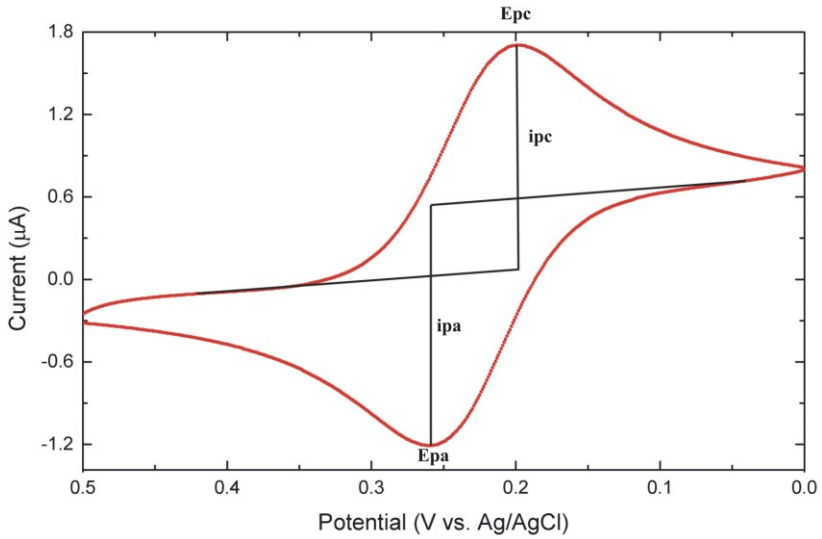

Figure 2.3 A Typical Cyclic Voltammogram

As shown in **Figure 2.3**, the scan begins from the left hand side of the current/voltage plot where no current flows. The species "O" is the only species in the initial solution. As the voltage is swept further to the right (to more reductive values), after the initial flow of capacitive currents, faradic current begins to flow and eventually reaches a peak before dropping. The corresponding peak current and the peak potential are the cathodic peak current and cathodic peak potential respectively. Faradic current begins to flow when the potential is near $E^{0'}$ (formal potential) due to the reduction of the species "O" (oxidized form). A rapid increase in the current occurs as the surface concentrtaion of "O" becomes smaller and smaller. The current at the peak is made up of two components. One is the initial current surge required to adjust the surface concentration of the reactant to its equilibrium concentration as given by the Nernst equation. The second is the normal diffusion-controlled current. The first current then decays rapidly and the diffusion layer is extended farther and farther away from the electrode surface. When the potential scan is reversed to more oxidative/ positive potential, the reduced form "R" begins to get oxidized. This is because of the larger concentration of "R" on the electrode surface at that particular moment. As the potential approaches $E^{0'}$, a peak due to oxidation of "R" appears. The corresponding peak current and the peak potential are the anodic peak current and anodic peak potential respectively. While performing CV measurements, initial and switching potentials must be carefully chosen. This requires the knowledge of the redox potentials of the molecule used. Initial potential should be chosen such that there are no other interfering electrode reactions occuring at that potential (open-circuit potential).

2.3.2 Instrumentation

A cyclic voltammogram system consists of an electrolysis cell, a potentiostat, a current-to-voltage converter, and a data acquisition system. The electrolysis cell consists of a working electrode, counter electrode, reference electrode, and electrolytic solution (supporting electrolytes and redox species). The working electrode's potential is varied linearly with time, while the reference electrode maintains a constant potential. The counter electrode conducts electricity from the signal source to the working electrode. The purpose of the supporting electrolyte is to provide sufficient conductivity as well as suppress migration of charged reactants and products. A potentiostat is an electronic device which uses a dc power source to

produce a potential which can be maintained and accurately determined, while allowing small current to be drawn into the system without changing the voltage. The current-to-voltage converter measures the resulting current, and the data acquisition system produces the resulting voltammogram.

In this dissertation, the three electrode cell setup consisted of a working electrode (recessed nanoporous array electrodes based on PS-*b*-PMMA), a reference electrode (Ag/AgCl) and a counter electrode (Pt wire). Depending on the scan rate, the working electrode type (different nanopore size) and the nature of the redox molecules (1,1' ferrocenedimethanol and cytochrome c), CVs obtained had different shapes. This allowed investigating the diffusion/adsorption mode of the redox molecules to the electrode surface.

2.3.3 Diffusion modes to electrode surface

In case of the RNEs based on PS-*b*-PMMA films used in this dissertation, three distinct voltammetric response regimes are possible depending on the scan rate and pore spacing as shown in **Figure 2.4(b) – (d)**. At slower scan rates, provided the pore spacing is small enough, the radial diffusion boundary layers totally overlap giving a linear diffusion (**Figure 2.4(b)**) similar to that for a macroelectrode (**Figure 2.4(a)**).

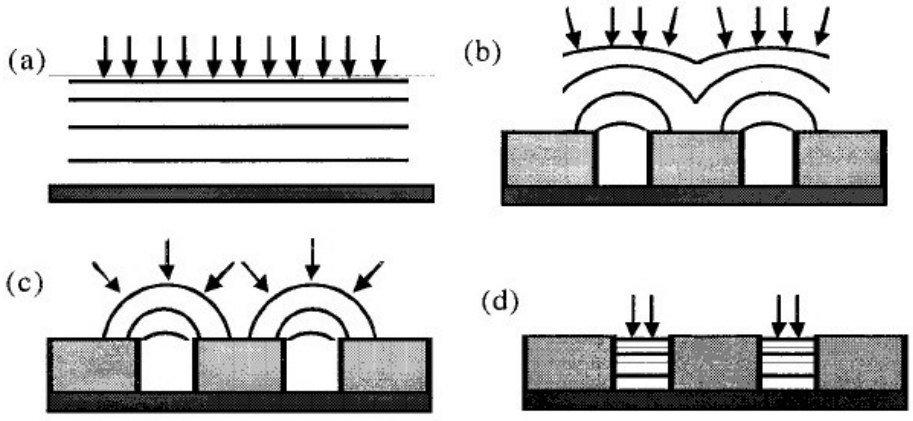

Figure 2.4 Schematic diagrams showing various diffusion modes to electrodes: (a) linear diffusion to planar electrode, (b) overlapping radial diffusion to porous electrode, (c) radial diffusion to porous electrode and (d) linear diffusion inside the nanopores of a porous electrode. (Reproduced from ref. 5 by permission of The American Chemical Society. Copyright © 2001.)

However, when the spacing between the pores is large, radial diffusion at each pore dominates the current response and each RNEs behave as individual entities (**Figure 2.4(c)**). For fast scans, the current response is governed by linear diffusion within the nanopores (**Figure 2.4(d)**).

2.3.4 Equations

A reversible redox reaction at a planar electrode gives a peak-shaped CV, regardless of the scan rate. This is due to the linear diffusion of the analyte to the electrode surface (**Figure 2.4(a)**). The peak current i_p is described by the Randles-Sevcik equation, equation 2.6 as given below. It should be noted that the peak current i_p is directly proportional to $v^{1/2}$, where v is the scan rate in V/s.

$$i_p = (2.69 \times 10^5) n^{3/2} A D_0^{1/2} C_0^* v^{1/2} \tag{2.6}$$

In the above equation, n is the number of electrons transferred, A is the area of the electrode (cm^2), D_0 is the diffusion coefficient (cm^2/s) of the redox species, and C_0^* is the bulk concentration of the redox species (mol/cm^3). Using the slope of the linear fit of the plot of peak current against the square root of the scan rate, the parameters given above can be easily determined; say for example, D_0 can be calculated from the slope if the area of the electrode A and the concentration C_0^* are known.

A recessed nanoporous array electrodes (RNEs) based on PS-*b*-PMMA has been used as a working electrode in the studies performed in chapter 3. When the pores are close to each other, the diffusion boundary layers totally overlap as shown in **Figure 2.4(b)**. A peak shaped CV is observed and the peak current in this case is also described by equation 2.6. In the case of large spacing between the pores, radial diffusion at each pore dominates the current response and each RNEs behave as individual entities (**Figure 2.4(c)**). A sigmoidal CV is observed and the limiting current is described by equation 2.7 as shown below.

$$i_{\lim} = \frac{4\pi nFCDa^2 N}{4L + \pi a} \tag{2.7}$$

In equation 2.7 above, n is the number of electrons transferred, F is Faraday's constant (96485 C/mol), C is the bulk concentration of the redox species (mol/cm^3), D is the diffusion coefficient (cm^2/s) of the redox species, a is the pore radius (cm), N is the number of pores involving the redox reaction and L is the pore length.

It has to be noted that in cases where the diffusion layers overlap as in **Figure 2.4(b)**, use of RNEs compared to the conventional electrode proves advantageous as they provide a better signal to noise ratio. If we consider a linear sweep voltammetric experiments involving a redox couple, peak currents (the signal) and capacitive currents (the main component of the noise, N) are given by equations 2.8 and 2.9, where A_{geom} is the total geometric area of the ensemble (nanodisks and insulator) and A_{act} is the active area (nanodisks' surface).

$$S = i_p = (2.69 \times 10^5) n^{3/2} A_{geom} D_0^{1/2} C_0^* \nu^{1/2} \quad (2.8)$$

$$N = i_c = A_{act} \nu C_d \quad (2.9)$$

At a conventional electrode in the same experimental conditions, equations 2.10 and 2.11 hold.

$$S = i_p = (2.69 \times 10^5) n^{3/2} A_{geom} D_0^{1/2} C_0^* \nu^{1/2} \quad (2.10)$$

$$N = i_c = A_{geom} \nu C_d \quad (2.11)$$

Combining equations 2.6 and 2.8 – 2.11 gives equation 2.12

$$(S/N)_{RNE} = (S/N)_{conv} A_{geom} / A_{act} \quad (2.12)$$

Since $A_{geom} > A_{act}$, it can be concluded from equation 2.12 that the signal to noise ratio at the RNEs is higher than that at a conventional electrode of the same geometric area by a factor $f = A_{geom}/A_{act}$.

2.3.5 Electrochemical responses of adsorbed monolayers

The electrochemical response (e.g., the voltammetric *i-E* curve) for the electrode reaction O + $ne \rightarrow$ R can be affected quite significantly by the adsorption of O or R. In the experiments described in chapter 3, CV measurements were influenced by the adsorption of the electroactive adsorbate to the electrode surface. Thus, CVs for *specific adsorption*, where a strong interaction between an electroactive adsorbate and the electrode causes the formation of a layer on the electrode surface, is described briefly here. For the adsorbed case, an ideal Nernstian reaction under Langmuir isotherm conditions would give a symmetric CV with $E_{pa} = E_{pc}$, and peak current given by

$$i_p = \frac{n^2 F^2}{4RT} \nu A \Gamma_0^* \quad (2.13)$$

where Γ_0^* is the surface coverage of the electrode by adsorbate, while all other parameters are the same as described for equation 2.6.

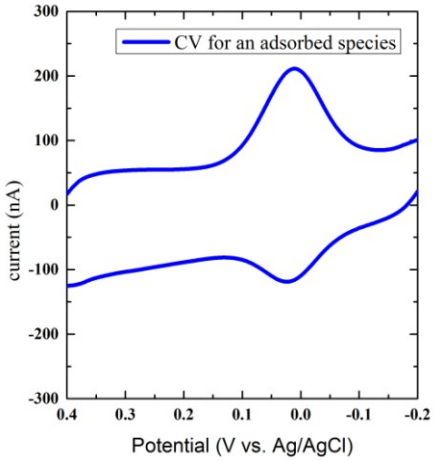

Figure 2.5 Cyclic Voltammogram for reduction and oxidation of cytochrome c adsorbed on a thioctic acid modified planar Au electrode. The thioctic acid modified planar Au substrate was dipped in cytochrome c solution for 1 hr, washed thoroughly and the CV recorded in solution containing the pH 7 phosphate buffer alone. Scan rate was 100 mV/s and the electrode area was 0.34 cm^2.

A typical CV encountered experimentally in phosphate buffer alone for a thioctic acid SAM covered gold electrode dipped in a cytochrome c solution for 1 hr, is shown in **Figure 2.5**. The CV peaks are somewhat symmetrical; with $E_{pa} \sim E_{pc}$ and the quasireversible nature led to a smaller peak current in the reversed scan.

It should be noted that in the case of CVs for adsorbed species, i_p is proportional to ν, in contrast to the $\nu^{1/2}$ dependence for the diffusing species. This means that if the logarithm of the peak current is plotted against the logarithm of the scan rate and the slope of the plot analyzed, CVs dominated by the diffusing species should have a slope close to 0.5 while a slope close to 1 is expected for CVs controlled by the adsorbed species as shown in the **Figure 2.6**. This approach of data analysis is followed in chapter 3.

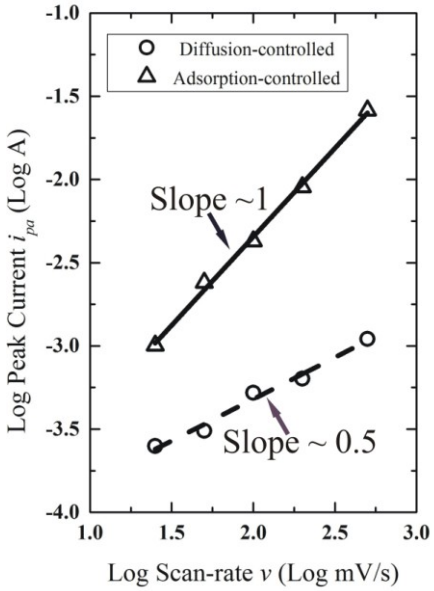

Figure 2.6 Plots of log i_p vs. log v for CVs dominated by diffusion (open circles) and those dominated by adsorption (open triangles).

2.4 Potentiometry[9]

2.4.1 General principles

Analytical methods that are based on potential measurements are called potentiometric methods, or potentiometry. Potentiometric methods are based on measuring the potential of an electrochemical cell without drawing appreciable current. Potentiometric measurements involve a reference electrode, an indicator electrode, and a potential-measuring device. **Figure 2.7** shows a typical cell for potentiometric analysis. This cell can be depicted as

$$\underbrace{\text{reference electrode}}_{E_{\text{ref}}} \,\big|\, \underbrace{\text{salt bridge}}_{E_{\text{j}}} \,\big|\, \underbrace{\text{analyte solution} \,\big|\, \text{indicator electrode}}_{E_{\text{ind}}}$$

The reference electrode in **Figure 2.7** is a half-cell with an accurately known electrode potential. E_{ref}, that is independent of the concentration of the analyte or any other ions in the solution under study. By convention, the reference electrode is always treated as the left-hand electrode in potentiometric measurements. The indicator electrode, which is immersed in a solution of the analyte, develops a potential, E_{ind}, that depends on the activity of the analyte. Most indicator electrodes used in potentiometry are highly selective in their responses. The third component of a potentiometric cell is a salt bridge that prevents the components of the analyte solution from

mixing with those of the reference electrode. A potential develops across the liquid junctions at each end of the salt bridge and the net potential across the salt bridge is the liquid junction potential E_j.

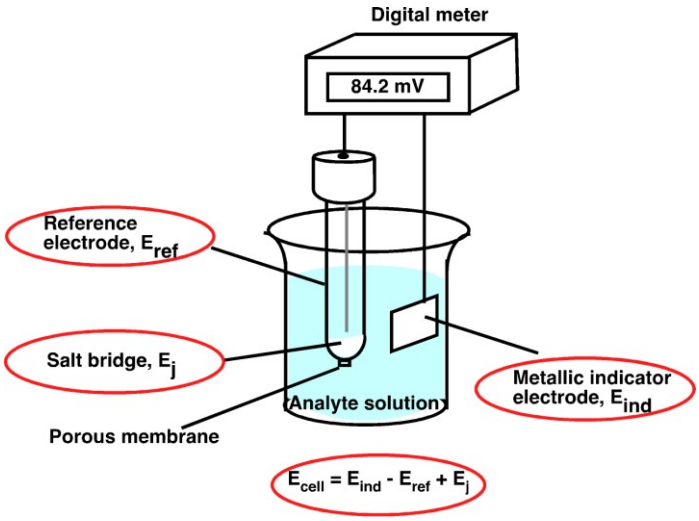

Figure 2.7 A cell for potentiometric measurements. (Drawn after a reference.[11])

The potential of the cell just described is given by the equation

$$E_{cell} = E_{ind} - E_{ref} + E_j \qquad (2.14)$$

The first term in this equation, E_{ind}, contains the information about the concentration of the analyte. A potentiometric determination of an analyte, then, involves measuring a cell potential, correcting this potential for the reference and junction potentials, and computing the analyte concentration from the indicator electrode potential.

2.4.2 Reference electrodes

An ideal reference electrode has a potential that is accurately known, constant and completely insensitive to the composition of the analyte solution. In addition, this electrode should be rugged, be easy to assemble, and be able to maintain a constant potential while passing small currents. Although standard hydrogen electrode can function as a reference electrode, it is seldom used as a reference electrode for day-to-day potentiometric measurements because it is somewhat inconvenient and also a fire hazard. A silver/silver chloride reference electrode was used for the studies described in this dissertation and is briefly explained next.

2.4.2.1 Silver/Silver Chloride Reference Electrodes

A silver/silver chloride reference electrode consists of a silver electrode immersed in a solution that is saturated in both potassium chloride and silver chloride:

$$Ag \mid AgCl(sat'd), KCl\ (sat'd) \parallel$$

The half-reaction is

$$AgCl + e^- \leftrightarrows Ag(s) + Cl^-$$

The potential of this electrode is 0.199 V versus the standard hydrogen electrode at 25 °C.

In Ito's group, we prepare a home-made silver/silver chloride reference electrode by depositing AgCl to a clean Ag wire in a 3.0 M KCl solution using chronoamperometry. The AgCl deposition is stopped when the Ag wire turns brown. Thus prepared Ag/AgCl is then dipped into a glass tube containing 3.0 M KCl with one end closed with a porous glass frit which acts as a salt bridge. The potential of this home-made Ag/AgCl (3.0 M KCl) reference electrode is 0.194 V versus the standard hydrogen electrode at 25 °C.

2.4.3 Liquid junction potential

A liquid-junction potential is the potential associated with the interface between two liquids that have different composition. Liquid junction potentials originate from the concentration gradient and/or difference in ionic mobility. **Figure 2.9** shows a very simple liquid junction consisting of a NaCl solution in contact with water. Both sodium ions and chloride ions tend to diffuse from NaCl solution side to the water side. The driving force for each ion is proportional to its mobility. In this example, chloride ions are more mobile than the sodium ions. Thus, chloride ions diffuse more rapidly to the right than sodium ions, and, as shown in **Figure 2.8**, a separation of charge results. The potential difference resulting from this charge separation may be several hundredths of a volt.

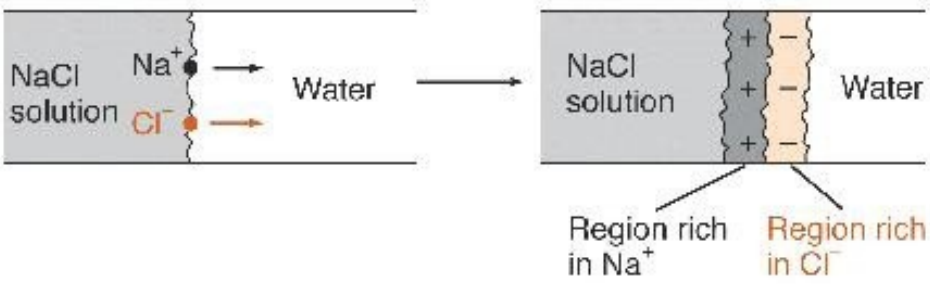

Figure 2.8 Schematic representation of a liquid junction potential

The magnitude of the liquid-junction potential can be minimized by placing a salt bridge between the two solutions. The salt bridge is most effective if the mobilities of the negative and positive ions in the bridge are nearly equal and if their concentrations are large. A 3.0 M KCl solution was used in the reference electrode for studies described in this dissertation which is good from both standpoints: mobilities of K^+ and Cl^- are nearly equal and the concentration used is large. The net-junction potential with such a salt bridge is typically a few millivolts.

2.4.4 Indicator electrodes

An indicator electrode responds rapidly and reproducibly to changes in the concentration of an analyte ion (or group of analyte ions). Although no indicator electrode is absolutely specific in its response, a few are now available that are remarkably selective. Indicator electrodes for potentiometry can be categorized into either metallic or ion-selective.

For **metal** electrodes, electrode potential is defined by the redox reactions as shown by equation 2.15 and the potential follows the Nernst equation as shown in 2.16.

$$Ox + ne^- \leftrightarrow \mathrm{Re}\,d \tag{2.15}$$

$$E = E^0 - \frac{RT}{nF}\ln\frac{a_{\mathrm{Re}\,d}}{a_{Ox}} \tag{2.16}$$

where E^0 is the standard electrode potential, R is the universal gas constant, T is temperature in Kelvin, n is the number of electrons involved, F is the Faraday constant and a is the activity.

The **metal** electrodes are mainly used for redox titrations. The measured potential is the open-circuit potential. The equilibrium potential of metal electrodes is sometimes important for voltammetry.

In the case of i**on-selective** electrodes, electrode potential is defined by the distribution of ions. pH glass electrode, solid-state membrane electrode and liquid membrane electrode are the most common types of **ion-selective** electrodes. The electrode potential follows equation 2.17.

For $M_i^{z_i+}$, $emf = (const) + \frac{RT}{z_i F}\ln a_1^{\alpha} = (const) + \frac{0.0592}{z_i}\log a_1^{\alpha}$ (2.17)

where z is the charge on the ion, α is the phase and all other parameters are the same as described in equation 2.16. The same experimental setup is used for both the metal and ion-selective indicator electrodes. The only difference is the mechanism involving potential generation.

Now that the general principles of potentiometry have been described, it is worthwhile to mention that the anodic gallium oxide was used as a type of indicator electrode and its potentiometric response was measured as described in chapter 5.

2.5 Scanning Electron Microscopy[4,10,11]

Electron microscopy, as the name suggests, uses an electron beam to form magnified images of specimens. The principle advantage of using electrons, rather than light, to form images is that electrons provide as much as a thousand-fold increase in resolving power — i.e., the ability to distinguish between two closely spaced points. In light microscopy, the use of light as the image-forming source limits the resolution. However, for an SEM, the diameter of the beam is the ultimate limiting factor affecting resolution. Only features whose spacing is larger or similar to the diameter of the beam can be resolved. The resolving power of a light microscope is, at best, 200 nm, whereas an SEM can resolve detail to approximately 3 nm. The increased resolving power is the main reason for using a scanning electron microscope.

2.5.1 Instrumental Components of an SEM

A basic diagram of an SEM is shown in **Figure 2.9**. The essential components of an SEM include the electron sources (gun), electron lenses, apertures, sample stage and the detectors. A brief description of each of these components follows.

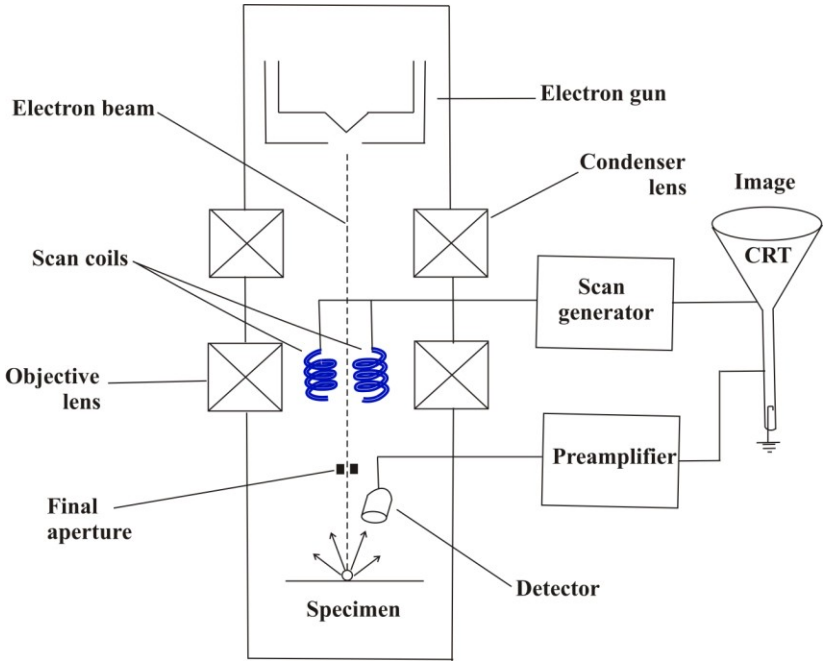

Figure 2.9 Schematic of a scanning electron microscope. (Drawn after a reference.[13])

Electron gun: They produce a steady stream of electrons that is necessary for SEMs to operate. Electron guns are typically one of two types. **Thermionic guns**, which are the most common type, apply thermal energy to a filament (usually a tungsten, which has a high melting point) to move the electrons away from the gun and toward the specimen under examination. **Field emission guns**, on the other hand, create a strong electrical field to pull electrons away from the atoms they are associated with. High brightness, high coherence and small energy dispersion are the factors that enable an SEM equipped with a field-emission gun to give far superior resolution than that of an SEM equipped with a thermionic gun. Electron guns are usually located at the very top of an SEM instrument and fire electrons to the specimen under examination. Their path is controlled by the lenses as described next.

Electron lenses: After the beam of electrons has been formed, it is controlled by the lenses. These lenses, made up of electromagnets which are controlled or focused by varying the passage of electrical current, are capable of bending the path of electrons. An electromagnetic lens performs functions similar to those of a glass lens in a light microscope. As a condenser lens, it can condense the beam of electrons; as an objective lens, it can focus on the specimen.

Apertures: Apertures are used in conjunction with electromagnetic lenses in a scanning electron microscope. An aperture is a piece of metal with a small round hole, having a diameter that varies from 30 μm to 1000 μm, depending on the placement and specific functions. Apertures are primarily used to control the diameter of the beam of electrons or to eliminate stray or widely scattered electrons.

Sample stage: Sample stage is the place where the specimen being examined is placed. For the microscope to produce clear images, the specimen must be kept extremely still. Thus, the sample stage must be very sturdy and insulated from vibration. One thing to note is that the sample stage does more than keep the specimen still. It is also equipped with the ability to rotate samples and place them at different angles so that constant remounting is not necessary to take different images.

Detectors: These devices detect the various ways that the electron beam interacts with the sample. It is worthwhile to talk about the specimen beam interaction and the mechanism of signal generation in an SEM to understand the different detectors used.

When the electron beam hits a sample, it interacts with the atoms in that sample. During these interactions, which could be repeated random scattering as well as absorption, the primary electrons lose energy within a teardrop-shaped volume of the specimen known as the interaction volume as shown in **Figure 2.10**. The interaction volume extends from less than 100 nm to around 5 µm into the surface. The penetration depth depends on the electron energy, the atomic number of the specimen and the specimen density.

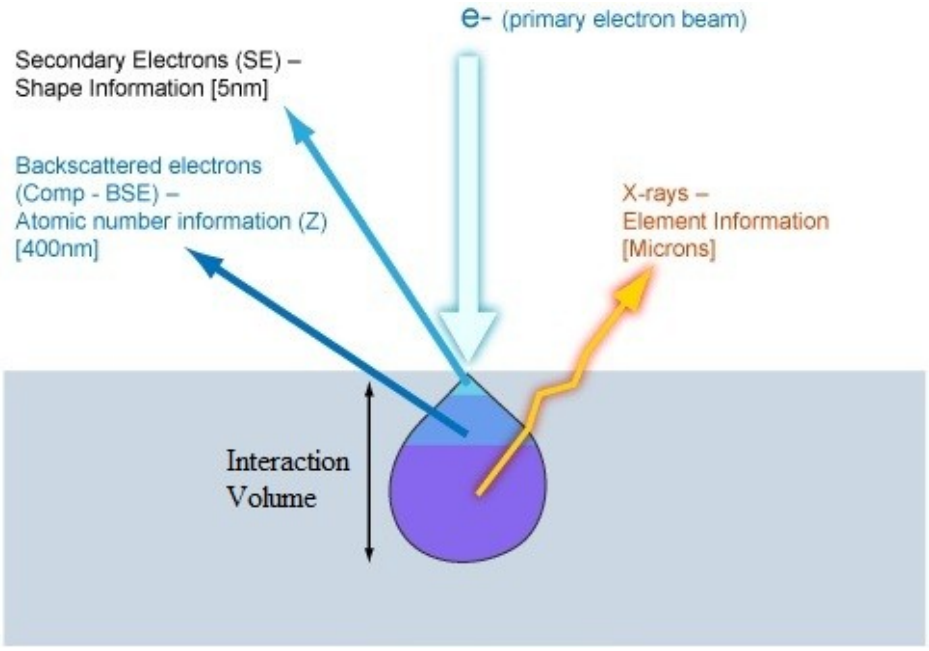

Figure 2.10 Schematic of electron-matter interactions showing the typical spatial resolution of different signals; secondary electrons, backscattered electrons and X-rays in the scanning electron microscope.

Mainly, three types of signal (secondary electrons, backscattered electrons and X-rays) as shown in **Figure 2.10** are measured in the SEM providing different information about the sample.

Secondary electrons are produced by inelastic interactions between incident electrons and weakly bound conduction band electrons in the atoms of the sample. The average energy of secondary electrons is about 3 eV to 5 eV. Because of their low energy, secondary electrons only escape from the sample if they are generated close to the surface: within a distance of 2 – 5 nm of the surface in most materials. Therefore, secondary electron images provide topographic

information. The standard secondary electron detector is an Everhart-Thornley detector, a type of scintillator-photomultiplier system, where a positively charged grid attracts the secondary electrons and accelerates them to sufficiently high energies to create a high pulse striking a scintillator. Another SEM detector is the in-lens detector, where the secondary electrons passing through the column aperture are accelerated towards a solid state detector. The in-lens detector complements the Everhart-Thornley detector by being more efficient at short working distances.

Backscattered electrons are incidental electrons that are reflected or back-scattered out of the specimen interaction volume by elastic scattering interactions with specimen atoms. Since heavy elements with a high atomic number backscatter electrons more strongly than light elements with a low atomic weight, backscattered electrons are used to detect contrast between areas with different chemical compositions. Backscatter detectors are usually either of scintillator or of semiconductor types. They provide compositional data related to element and compound detection. Although topographic information can be obtained using a backscatter detector, it is not as accurate as a secondary electron detector.

X-rays, emitted from beneath the sample surface, which are produced by the interaction of electrons with the sample, may also be detected in an SEM equipped for energy-dispersive X-ray spectroscopy (EDS). Interaction of the primary beam with atoms in the sample causes shell transitions which result in the emission of an X-ray. The emitted X-ray has an energy characteristic of the parent element, which can be detected using an EDS detector as explained in section 2.2.

2.5.2 Working Principle of an SEM

The SEM images for the studies described in chapter 4 was obtained with FE-SEM instrument in which field emission gun (as described earlier) was the source of electrons. The electron gun produces a beam of electrons typically having an energy ranging from 0.2 keV to 40 keV. These electron beams are condensed by the condenser lens and then focused as a very small point (a spot about 0.4 nm to 5 nm) on the specimen by the objective lens. A set of small coils of wire, called the scan coils, is located within the objective lens. A varying voltage produced by the scan generator energizes these coils creating a magnetic field that deflects the beam of electrons back and forth in a controlled pattern called raster.

The varying voltage from the scan generator is also applied to a set of deflection coils around the neck of a cathode-ray-tube (CRT). The magnetic field from this coil causes the deflection of a spot of light back and forth on the surface of the CRT, which is exactly the same pattern as the deflection of the beam of electrons on the sample.

When the beam of electrons strikes the sample, a complex series of interactions occurs, resulting in the production of secondary electrons from the sample, which are collected by the detector, converted to a voltage, and amplified. The amplified voltage is then applied to the grid of the CRT which modulates or changes the intensity of the spot of light on the surface. For example, if at a given instant the beam is on a projection on the surface, a large amount of secondary electrons will be detected, causing a large voltage in the detector that results in a bright spot on the surface of the CRT. If the beam of electrons then moves to a depression on the sample, fewer electrons will be detected and a smaller voltage will be developed in the detector, resulting in a darker spot on the surface of the CRT. The SEM image, then, consists of thousands of spots of varying intensity on the face of a CRT that corresponds to the topography of the sample. The secondary electron detector used for the SEM images shown in chapter 4 was obtained with an in-lens detector. When imaging the samples, short working distances were used and the in-lens detector is more efficient at short working distances and was thus the preferred choice.

2.5.3 Strengths and Limitations of an SEM

The SEM is a very useful instrument when it comes to characterization of solid materials. The strengths of SEMs include its detailed three-dimensional topographical imaging, versatile information obtained from different detectors, comparatively easy operation; with user-friendly interfaces and minimal sample preparation. On the other hand, SEMs are expensive and large requiring an area free of any possible electric, magnetic or vibration interference. In addition, samples must be solid, dehydrated, able to withstand high vacuum and they must fit into the microscope chamber.

References

(1) Tompkins, H. G., Irene, E. A., Eds.; William Andrew, Inc.: New York, 2005.

(2) Azzam, R. M. A.; Bashara, N. M. *Ellipsometry and Polarized Light*; Elsevier Science B. V.: Amsterdam, The Netherlands, 1987.

(3) Johal, M. S. *Understanding Nanometrials*; Taylor & Francis Group: Boca Raton, FL, 2011.

(4) Goldstein, G. I.; Newbury, D. E.; Echlin, P.; Joy, D. C.; Fiori, C.; Lifshin, E. *Scanning Electron Microscopy and X-ray Microanalysis*; Plenum Press: New York, 1981.

(5) Bard, A. J.; Faulkner, L. R. *Electrochemical Methods: Fundamentals and Applications*; 2nd ed.; Wiley: New York, 2001.

(6) Jeoung, E.; Galow, T. H.; Schotter, J.; Bal, M.; Ursache, A.; Tuominen, M. T.; Stafford, C. M.; Russell, T. P.; Rotello, V. M. *Langmuir* **2001**, *17*, 6396.

(7) Ugo, P.; Moretto, L. M.; Vezza, F. *ChemPhysChem* **2002**, *3*, 917.

(8) Ito, T.; Audi, A. A.; Dible, G. P. *Anal. Chem.* **2006**, *78*, 7048.

(9) Skoog, D. A.; West, D. M.; Holler, F. J.; Crouch, S. R. *Analytical Chemistry An Introduction*; 7th ed.; Thomson Learning, Inc.: Boston, 1999.

(10) Flegler, S. L.; Heckman, J. W. J.; Klomparens, K. L. *Scanning and Transmission Electron Microscopy : An Introduction*; Oxford University Press: New York, 1993.

(11) Garratt-Reed, A. J.; Bell, D. C. *Energy Dispersive X-ray Analysis in the Electron Microscope*; BIOS Scientific Publishers Limited: Oxford, 2003.

Chapter 3 - Electrochemical Study of the Diffusion of Cytochrome c within Nanoscale Pores Derived from Cylinder-Forming Polystyrene-Poly(methylmethacrylate) Diblock Copolymers

Reproduced by permission of the Elsevier B.V.
Published as: Pandey, B.; Tran-Ba, K. H.; Li, Y.; Diaz, R.; Ito T. *Electrochimica Acta*, **2011**, *56*, 10185-10190.

3.1 Introduction

Nanoporous materials derived from cylinder-forming block copolymers have received much attention as membranes for chemical separations [1,2] in addition to lithographic masks for fabricating nanoscale structures and templates for nanomaterials synthesis [3-5]. These monoliths comprise an array of uniform cylindrical nanopores penetrating through the monoliths, which are fabricated via selective etching of cylindrical domains formed by the phase separation of a cylinder-forming block copolymer. As with conventional track-etched polymer membranes and nanoporous anodic alumina membranes [6-9], nanoporous monoliths derived from cylinder-forming block copolymers have exhibited the efficient size-selective separation of chemical and biological species because of their uniform cylindrical pore structure and narrow pore diameter distribution [10-13]. The use of block copolymers with different molecular weights provides a simple means for varying pore diameter in a monolith to adjust the size-based selectivity in molecular penetration. Controlling the surface chemistry of block copolymer-derived nanopores makes it possible to regulate the monolith permeability based on chemical interactions. In contrast to track-etched membranes and nanoporous anodic alumina, block copolymer-derived nanoporous monoliths can be prepared as films thinner than 100 nm, possibly leading to the faster diffusion-controlled separations of chemical and biological species [14,15].

To employ these nanoporous membranes for chemical separations, filtration and drug delivery, knowledge on the rate and selectivity in the permeation of molecules being separated or delivered through the membrane is required. Such membrane permeability has been usually

assessed by measuring the flux of molecules across a membrane that is determined by monitoring their concentrations in a receiving solution [6,8,9]. This approach is versatile, but it requires mechanically-stable, flow-through membranes having sufficient thickness. Electrochemical methods employing redox-active probes have been employed as an alternative approach to investigate molecular permeation through thin insulator-based nanoporous films supported by electrodes [16-21]. Diffusion behavior of small molecules within cylindrical nanopores was electrochemically investigated using recessed nanodisk-array electrodes (RNEs) whose recessed structures were formed by monolithic layers comprising vertically-oriented nanopores such as nanoporous anodic alumina membranes [16,22-25], track-etched polymer membranes [26-29] and block copolymer-derived nanoporous films [30-34]. These studies revealed surface diffusion of redox amphiphiles localized on nanopore surface [23], as well as the influence of electrostatic interactions [29,31,32] and steric effects [33] on molecular permeation through the nanopores.

In this study, the effects of nanopore diameter on the diffusion of cytochrome c were investigated by cyclic voltammetry (CV) at RNEs based on nanoporous films derived from cylinder-forming polystyrene-poly(methylmethacrylate) diblock copolymers (CF-PS-*b*-PMMA; 0.3 as the PMMA volume fraction) [30-34]. CV measurements were performed in the presence of relatively high supporting electrolyte (75 mM) so that the measured voltammograms were primarily controlled by the diffusion of redox species rather than migration. RNEs were fabricated by selectively removing cylindrical PMMA domains in annealed CF-PS-*b*-PMMA films on planar gold substrates [31,34-36]. RNEs with 11-, 14- or 24-nm diameter pores were prepared from CF-PS-*b*-PMMA with three different molecular weights. The nanopore surfaces were covalently functionalized with poly(ethylene glycol) to reduce the nonspecific adsorption of the biomolecules [33,37,38]. Here, cytochrome c was used as a model biomolecule for the following reasons. First, its one-electron redox reaction is (quasi-) reversible in the presence of appropriate promoters, which simplify the measurements and interpretation of voltammograms [39,40]. In contrast, the redox reaction of ferritin, which was used in our previous study to demonstrate the size-exclusion properties of similar nanopores [33], involves irreversible Fe(II) release from the protein core [41], and thus only one voltammogram could be measured on each RNE. Second, the ratio of its hydrodynamic diameter (ca. 4 nm, measured with dynamic light scattering) [42] to the diameter of the RNE nanopores employed (11–24 nm) is in the range of

0.16–0.36. According to hydrodynamic models [6,43], the diffusion coefficient of cytochrome c inside the nanopores is estimated to decrease by a factor of 2-10 compared to the bulk diffusion coefficient value. The decreased diffusion coefficient will permit the discussion of the hindered diffusion of cytochrome c within these nanopores [6]. In addition, simultaneous penetration of multiple cytochrome c molecules is geometrically restricted within 11-nm pores, whereas it is more feasible within 24-nm pores as suggested by diffusion-controlled voltammograms of cytochrome c at a RNE based on a nanoporous anodic alumina membrane with 30-nm pores [25]. CVs of cytochrome c were compared with those of 1,1'-ferrocenedimethanol. 1,1'-Ferrocenedimethanol is uncharged and smaller in size (hydrodynamic diameter of ≈ 0.7 nm) than the pore diameter (11 ~ 24 nm), and thus its diffusion within the nanopores will not be significantly affected by electrostatic and steric effects. The geometrically restricted diffusion will be the basic principle of single file diffusion recently reported on flow-through nanoporous membranes derived from block copolymers [13].

3.2 Experimental

3.2.1 Chemicals and Materials

All aqueous solutions were prepared with water having a resistivity of 18 MΩ cm or higher (Barnstead Nanopure Systems). Three types of CF-PS-*b*-PMMA (71K CF-PS-*b*-PMMA: M_n = 50 000 g/mol for PS and 21 000 g/mol for PMMA, M_w/M_n = 1.08; 43K CF-PS-*b*-PMMA: M_n = 31 400 g/mol for PS and 11 500 g/mol for PMMA, M_w/M_n = 1.06; 31K CF-PS-*b*-PMMA: M_n = 21 500 g/mol for PS and 10 000 g/mol for PMMA, M_w/M_n = 1.06) were purchased from Polymer Source and used as received. Sodium dihydrogen phosphate (Fisher Chemical), sodium hydroxide (Fisher Chemical), sodium hydrogen phosphate (Fisher Chemical), potassium nitrate (Fisher Chemical), 1,1'-ferrocenedimethanol (Aldrich Chemical), *DL*-thioctic acid (TCI-EP), 1-ethyl-3-(3-dimethylaminopropyl)carbodiimide hydrochloride (EDC; Chem-impex International), *N*-hydroxysuccinimide (NHS; Acros Organics), and triethyleneglycol monoamine ($(PEO)_3NH_2$; Molecular Biosciences Inc.) were of reagent grade quality or better and used without further purification. Horse heart cytochrome c (Sigma-Aldrich) was purified on a CM-52 cellulose column (Whatman) at 4 °C according to the method reported by Brautigan et al. [44] and used within two weeks [45]. The concentration of the purified cytochrome c was determined

spectrophotometrically at 410 nm with an extinction coefficient of ε_{410} = 106 100 $M^{-1}cm^{-1}$ using a Hewlett-Packard HP 8453 UV-Vis spectrometer [46]. Gold-coated silicon wafers, which were prepared by sputtering 10 nm of Ti followed by 200 nm of Au onto Si (100) wafers, were purchased from LGA thin films (Foster City, CA).

3.2.2 Electrode Preparation and Electrochemical Measurements

RNEs based on CF-PS-*b*-PMMA-derived nanoporous films on gold substrates were prepared according to procedures reported previously [31-34]. Briefly, thin films of CF-PS-*b*-PMMA were prepared by spin-casting from toluene solution (*ca.* 0.75 wt%) on clean gold-coated Si substrates (*ca.* 12 x 15 mm^2) and then annealed at 180 °C in vacuum (~0.3 Torr) for 60 h. Film thickness was measured to be ~25-35 nm by spectroscopic ellipsometry (J.A. Woollam Alpha-SE). The surface of annealed films was characterized using Tapping-mode atomic force microscopy (AFM) to measure the diameter of vertically-oriented cylindrical PMMA domains exposed to the film surface. The cylindrical PMMA domains in the film were removed via UV irradiation (254 nm, 20 mW/cm^2, 80 min) under an Ar atmosphere and subsequent rinsing with glacial acetic acid. The nanopore surface in the resulting film was covalently modified with triethyleneglycol moieties via EDC-mediated amidation of the surface –COOH groups with $(PEO)_3NH_2$ [32,33] to reduce the nonspecific protein adsorption onto the nanopore surface [47]. The substrate was immobilized at the bottom of the electrochemical cell as reported previously [31-34]. The RNE was then treated with an ethanolic solution of thioctic acid (10 mM) for 12 h followed by washing with ethanol and water to modify the exposed gold surface with a self-assembled monolayer of thioctic acid [48,49]. CF-PS-*b*-PMMA-derived nanoporous films on planar gold substrates were not damaged during the immersion in the ethanol solution because of the crosslinking of PS matrix during the UV irradiation [11,50]. As a control experiment, a thioctic acid-modified planar gold substrate was similarly prepared in the cell. During the interval of CV measurements in the solutions of 1,1'-ferrocenedimethanol and cytochrome c, the substrate immobilized in the cell was treated with a thioctic acid solution to maintain the sufficient thioctic acid coverage. CV measurements were performed in a three-electrode cell containing a Ag/AgCl (3 M KCl) reference electrode, a Pt counter electrode using a CH Instruments model 720C electrochemical analyzer. The film area exposed to the solution was defined by an O-ring (0.66

cm in diameter). The solutions of 1,1'-ferrocenedimethanol and cytochrome c were bubbled by Ar, and electrochemical measurements were performed under Ar atmosphere. The redox current of cytochrome c measured at a RNE was obtained by drawing the background as shown in **Figure 3.1**.

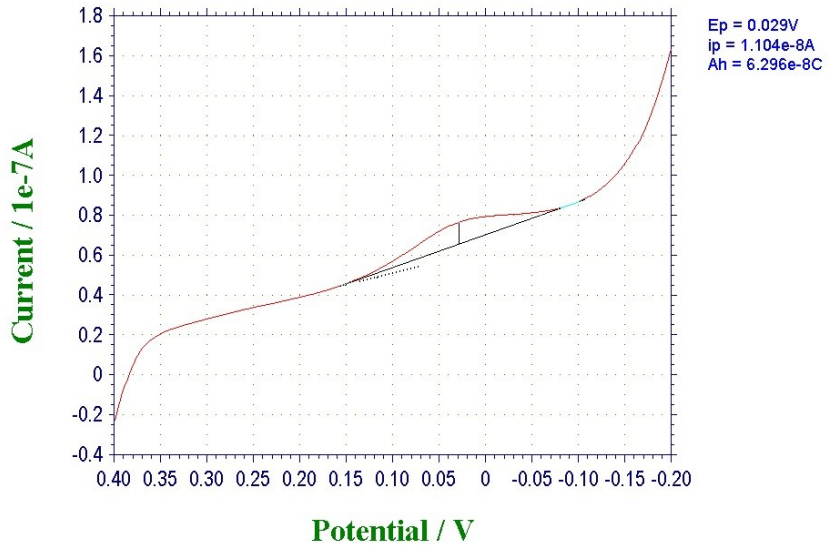

Figure 3.1 One of the CVs shown in Figure 3.5 (b) (v = 0.01 V/s) (*vide infra*), showing the way to measure the peak current.

The formation of thioctic acid SAMs on planar and nanoporous electrodes was verified as a decrease in charging current measured in 0.1 M KNO_3. A double layer capacitance, calculated from a charging current decreased by a factor of 3.21 ± 0.32 for planar electrode and by factors of 2.21± 0.62, 2.49 ± 0.51 and 1.91 ± 0.23 for films with 11, 14 and 24 nm diameter pores respectively.

3.2.3 COMSOL Multiphysics® Simulation of Voltammetric Responses

Voltammetric responses were simulated by Khanh Hoa Tran Ba according to the method previously employed by Lavacchi et coworkers [51] and based on the model developed by Davies and Compton [52]. **Figure 3.2** shows the model geometries used in our simulation for a RNE based on hexagonally-distributed nanopores. It should be noted that the model represents a simplified system where the experimentally observed pore spacing heterogeneity has not been incorporated. The diameter of a nanopore, and thus a nanodisk electrode, 2a was 24 nm, the

recession depth L was 30 nm, and the interpore spacing 2s was varied from 44 to 2304 nm. To simulate the semi-infinite boundary condition of the experiment, the cell height was fixed to 480 μm [52]. A cylindrical coordinate system was used to model the nanodisk electrode at the bottom of the nanopore, and the origin of it was set at the center of the nanopore opening. Simulations were performed using COMSOL Multiphysics ver 4.1 with the Chemical Engineering Module (COMSOL, Inc.) operated on a Dell Optiplex GX520 (Pentium 4 CPU, 3 GHZ, 4 GB RAM).

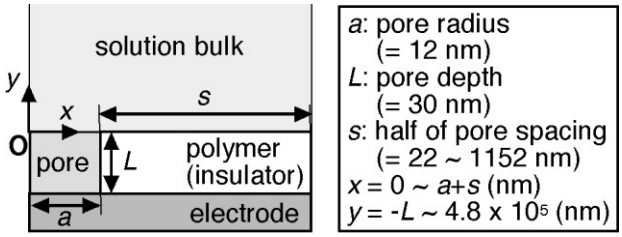

Figure 3.2 Schematic simulation geometry of a RNE: *a* is the radius of pore and electrode, *s* is half of the spacing between adjacent nanopores, and *L* is the recess depth (film thickness). The origin of the cylindrical coordinate system was set to the center of the pore opening.

3.2.4 Equations Employed in the Simulations

A simple single electron transfer was assumed in the simulation for 1,1'-ferrocenedimethanol and cytochrome c:

$$A + e^- \rightleftharpoons B \tag{3.1}$$

Additionally, we assumed that the transport was solely based on diffusion as described by a couple of Fick's second law equations:

$$\frac{\partial c_i}{\partial t} + \nabla \cdot (-D_i \nabla c_i) = 0 \tag{3.2}$$

where c_i is the concentration (mol/m^3) of species i (A or B); D_i the diffusion coefficient (m^2/s) of species i; t is the time (s). At the electrode surface, the electron flux, J (mol/m^{2}s), the number of moles crossing the unit surface for one second, was described by [51]:

$$J = c_{A,s} \cdot K_f - c_{B,s} \cdot K_b \tag{3.3}$$

where $c_{i,s}$ (mol/m^3) is the concentrations of species i at the electrode surface ($x = 0 \sim a$, $y = -L$). K_f and K_b are forward and backward electron transfer rate constants (m/s), respectively:

$$K_f = K_{het} \cdot \exp\left(\frac{\alpha_A nF(E - E^0)}{RT}\right) \tag{3.4}$$

$$K_b = K_{het} \cdot \exp\left(-\frac{\alpha_B nF(E - E^0)}{RT}\right) \tag{3.5}$$

In these equations, K_{het} is the heterogeneous electron transfer rate constant (m/s), α_i is the electron transfer coefficients of species *i* (= 0.5 in this simulation), *n* is the number of exchanged electrons (*n* = 1 for the redox-active species used in this study), *F* is the Faraday constant (= 96485 C/mol), *E* is the electrode potential, E^0 is the voltammetric half-wave potential against Ag/AgCl (= 0.22 V for 1,1'-ferrocenedimethanol [53] and = 0.01 V for cytochrome c) [54] and *R* is the gas constant (*R* = 8.31 J/Kmol). According to literatures, K_{het} was 0.070 m/s for 1,1'-ferrocenedimethanol [53] and 8.7 x 10^{-5} m/s for cytochrome c [54]. The diffusion coefficients and K_{het} were assumed to be identical for a redox species in its oxidized and reduced forms.

The triangular shape potential waveform of the cyclic voltammetry experiment was modeled by [55]:

$$E(t) = \left(\frac{\nu \cdot t_0 + 2E_{initial}}{2}\right) + \sum_n -\frac{4\nu \cdot t_0}{n^2\pi^2}\cos\left(\frac{n\pi \cdot t}{t_0}\right) \tag{3.6}$$

$$t_0 = \frac{E_{high} - E_{low}}{\nu} \tag{3.7}$$

where $E_{initial}$ is the initial, E_{high} is the highest and E_{low} is the lowest applied potential (*E*) in the cyclic voltammetric experiment; *v* is the potential scan rate (V/s); *t* is the time (s) and *n* are odd valued integers from 1 to 15. To obtain the current of the voltammetric response, the flux of the redox molecule at the electrode interface was integrated according to [56]:

$$i = 2\pi FD \cdot \int_0^a r \cdot \left[\frac{\partial c_{A,s}}{\partial y}\right]_{y=-L} dr \tag{3.8}$$

3.2.5 Computation

In the COMSOL Model Builder, the space dimension was chosen as 2D axial symmetric to reduce the computational time. The Fick's second law was solved using a time dependent solver and the Physics Model 'Transport of Diluted Species' was employed. In the model, the 'No Flux' boundary conditions have been set for boundaries 5, 6, 7 and 8 (**Figure 3.3**). The

'Axial Symmetry' conditions have been chosen for boundaries 3 and 1. According to Eq 3, the 'Flux' boundary condition has been set for boundary 2. For species A and B, the 'Inward Flux' was $-c_{bulk,\,A}\,K_F+(c_{bulk,\,A}-c_{A,s})\,K_B$ and $-c_{bulk,\,B}\,K_B+(c_{bulk,\,B}-c_{B,s})\,K_F$, respectively, where K_F and K_B are the 'Mass transfer coefficient' of A and B; c_{bulk} was 3.1 mM (1,1'-ferrocenedimethanol) or 16 µM (cytochrome c). No condition has been selected for boundary 4. 'Initial Values' have been set for the whole geometry (Domains I + II) determining the initial bulk concentration of A (1,1'-ferrocenedimethanol: 3.1 mM, cytochrome c: 0 M) and B (1,1'-ferrocenedimethanol: 0 M, cytochrome c: 16 µM). To simulate different diffusion coefficients in different regions of the RNE, two separate 'Diffusion' conditions were selected for domains I and II. Thus, for each domain, a couple of Fick's second law equations with different diffusion coefficients (Eq 2) have been solved. The bulk diffusion coefficients of 1,1'-ferrocenedimethanol and cytochrome c ($D_{FcDM,bulk}$ and $D_{cytc,bulk}$) employed in Domain I were 6.4×10^{-10} m^2/s [57] and 1.1×10^{-10} m^2/s [42], respectively.

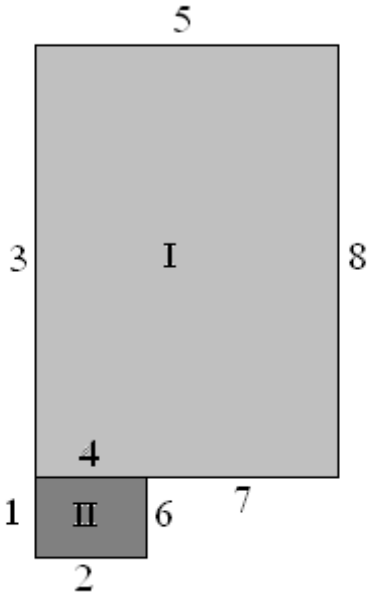

Figure 3.3 Schematic model geometry showing eight boundaries (1-8) and two domains (I, II).

For the overall mesh, a maximum element size of 1 µm, a minimum element size of 9.6 nm, a mesh grow rate of 1.2 and mesh curvature factor of 0.2 were chosen. For the mesh refinement at boundary 2, 4 and edges of domain II, a maximum element size of 0.05 nm, a

minimum element size of 0.01 nm, a mesh grow rate of 1.1 and mesh curvature factor of 0.2 were employed. The mesh was refined locally at the electrode and edge areas until no further change in the current was observed. Thus, the 'Regular refinement' function was chosen to refine Domain II (# of refinement = 1). **Figure 3.4** shows a mesh employed for the simulations corresponding to a simulation cell with 12 nm pore radius (a = 12 nm; 24 nm in pore diameter), 68 nm interpore spacing (s = 68/2 -12 = 22 nm), 30 nm recession (L = 30 nm) and a cell height of 480 μm (out of the range in **Figure 3.4**). In this example, there are 79555 triangular elements and 5595 edge elements. For a potential increment size of 0.05 V/s and the relative and absolutes tolerances of 1 x 10^{-5}, the one cycle CV simulation required ~16 minutes.

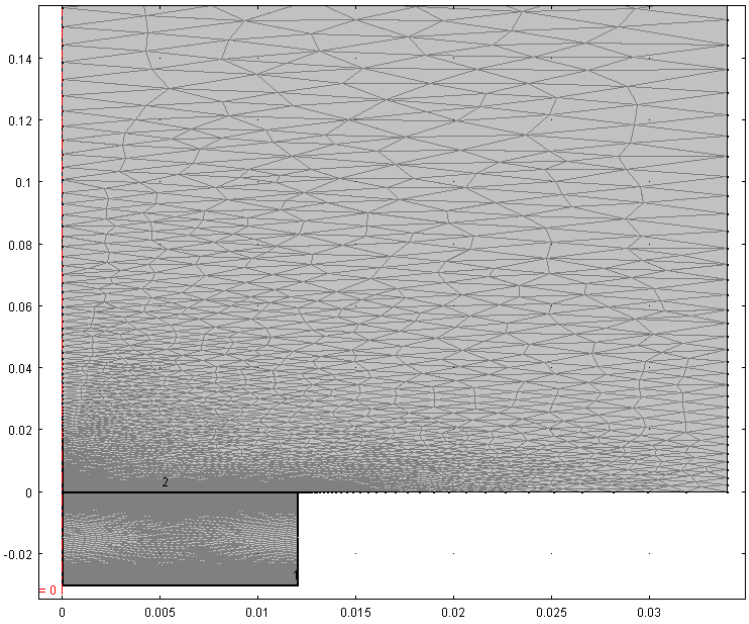

Figure 3.4 An example mesh of a simulation cell for a RNE with 12 nm pore radius (a = 12 nm), 68 nm interpore distance (s = 22 nm), 30 nm recession (L = 30 nm) and a cell height of 480 μm.

3.3 Results and Discussion

In this study, CVs of cytochrome c were measured on RNEs to obtain insight into the diffusion of biomolecules within CF-PS-*b*-PMMA-derived nanoporous films. Thioctic acid SAMs were employed as a promoter to measure the faradic current of cytochrome c. (Quasi-) reversible CVs of cytochrome c were reported on gold electrodes modified with COOH-terminated SAMs [45,58], including thioctic acid SAMs [59]. CVs of 1,1'-ferrocenedimethanol and

cytochrome c were measured on each electrode to compensate for variations in the density of active nanodisk electrodes. Such variations are attributable to the metastable nature of the vertical orientation of the PMMA domains in gold-supported CF-PS-*b*-PMMA films [34,36]. Here, the concentration-normalized ratio of the faradic peak currents of the two species, R_{diff}(cytc/FcDM), measured on the same electrode at a fixed v (= 0.05 V/s) was employed to discuss CV data because of the variation in the active electrode area of different RNEs:

$$R_{diff}(cytc/FcDM) \equiv \frac{i_{p,cytc}/C_{cytc}}{i_{p,FcDM}/C_{FcDM}} \qquad (3.9)$$

In Eq (3.9), $i_{p,cytc}$ and $i_{p,FcDM}$ are the peak currents in CVs at 0.05 V/s for the reduction of cytochrome c and the oxidation of 1,1'-ferrocenedimethanol, C_{cytc} and C_{FcDM} are the concentrations of cytochrome c and 1,1'-ferrocenedimethanol in the solutions employed.

3.3.1 CVs on Planar Thioctic Acid-Modified Gold Electrodes

CVs were first recorded on planar electrodes without nanoporous films to verify the electrochemical behavior of the two redox species on thioctic acid-modified gold surfaces. **Figure 3.5(a)** shows typical CVs of 1,1'-ferrocenedimethanol on a thioctic acid-modified gold electrode at different scan rates. These CVs were quasi-reversible as indicated by the relatively large difference in redox peak potentials (ΔE_p = 132 mV at 0.05 V/s). The presence of a thioctic acid SAM on the electrode probably reduced the electrode reaction kinetics for 1,1'-ferrocenedimethanol. The slope of the log–log plot of the oxidation peak current of 1,1'-ferrocenedimethanol against scan rate (**Figure 3.5(c)** (open circles)) was close to 0.5 (**Table 3.1**), consistent with the slope expected in CVs controlled by linear diffusion of redox species [60]. As compared to the CVs of 1,1'-ferrocenedimethanol, CVs of cytochrome c on the same electrode (**Figure 3.5(b)**) exhibited a smaller ΔE_p (67 mV at 0.05 V/s). However, the reduction peak currents were significantly (> 30%) larger than the oxidation peak currents, as sometimes observed in CVs of cytochrome c on gold electrodes modified with COOH-terminated SAMs [45,58,59]. The slope of the log–log plot (**Figure 3.5(c)** (filled circles)) was slightly larger than 0.5 (**Table 3.1**), suggesting a dominant contribution by linearly-diffusing cytochrome c molecules and a minor contribution by adsorbed species.

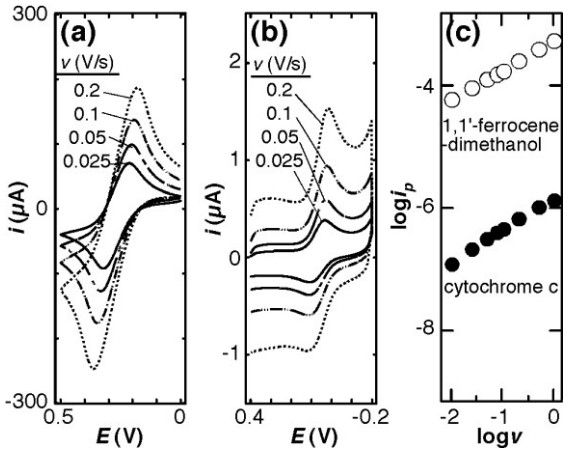

Figure 3.5 Typical CVs of (a) 3.1 mM 1,1'-ferrocenedimethanol (in 0.1 M KNO_3) and (b) 24 μM purified horse heart cytochrome c (in 75 mM NaH_2PO_4-Na_2HPO_4 buffer (pH 7.0)) on a planar gold electrode modified with a thioctic acid-SAM at four different scan rates (v = 0.025, 0.05, 0.1 and 0.2 V/s). (c) Plots of logi_p vs log$v$ (i_p: anodic peak current for 1,1'-ferrocenedimethanol and cathodic peak current for cytochrome c) obtained from the gold electrode.

For a reversible CV controlled by linear diffusion, the peak current, i_p (A), at scan rate, v (V/s), is given by the following equation [60]:

$$i_p = 0.446nFAC\sqrt{\frac{nFDv}{RT}} \tag{3.10}$$

where n is the number of electrons (n = 1 for the redox-active species used in this study), F is the Faraday constant (= 96485 C/mol), R is the gas constant (= 8.31 J/K mol), T is the temperature (= 298 K), A (cm^2) is the electrode area, D (cm^2/s) is the diffusion coefficient of the redox-active species, and C (mol/cm^3) is its concentration. For peak-shaped, linear-diffusion-controlled CVs, Eqs (9) and (10) give the following relationship between R_{diff}(cytc/FcDM) and the diffusion coefficients:

$$R_{diff}(cytc/FcDM) = \sqrt{\frac{D_{cytc}}{D_{FcDM}}} \tag{3.11}$$

where D_{cytc} and D_{FcDM} are the effective diffusion coefficients of cytochrome c and 1,1'-ferrocenedimethanol. The R_{diff}(cytc/FcDM) value obtained on the planar thioctic acid-modified gold electrodes (0.36 ± 0.04, **Table 3.1**) was close to the value (0.41) estimated from the diffusion coefficients of 1,1'-ferrocenedimethanol (6.4 x 10^{-6} cm^2/s) [57] and cytochrome c (1.1 x

10^{-6} cm^2/s) [42] in the solution bulk ($D_{FcDM,bulk}$ and $D_{cytc,bulk}$, respectively), even though the CVs measured were neither perfectly reversible (for 1,1'-ferrocenedimethanol) nor completely diffusion-controlled (for cytochrome c). This result suggests that R_{diff}(cytc/FcDM) can be used to discuss the diffusion behavior of the redox species onto electrode surface.

Table 3.1 Electrochemical Data on Planar and Recessed Nanodisk-Array Gold Electrodes.

electrodes	pore dia. (nm)[a]	N_{dif}/N_{ads}[b]	$Slope_{diff\text{-}FcDM}$[c]	$Slope_{diff\text{-}cytc}$[c]	$Slope_{ads\text{-}FcDM}$[d]	$Slope_{ads\text{-}cytc}$[d]	R_{diff}(cytc/FcDM)[e]
planar	–	3/0	0.48 ± 0.01	0.57 ± 0.06	–	–	0.36 ± .04
71K	24 ± 3	4/1	0.29 ± 0.03	0.38 ± 0.15	0.35[f]	0.67[f]	0.091 ± 0.057
43K	14 ± 1	1/3	0.31[f]	0.27[f]	0.28 ± 0.04	0.64 ± 0.04	0.13[f]
31K	11 ± 2	0/3	–	–	0.29 ± 0.05	0.62 ± 0.17	–

[a] The average and standard deviation of surface-exposed vertical PMMA domains measured using Tapping-mode AFM. [b] Numbers of electrodes that gave CVs of cytochrome c diffusing from the solution (N_{dif}) and those of adsorbed cytochrome c (N_{ads}). [c] The average and standard deviation of the slopes of logi_p vs log$v$ plots (**Figures 3.5(c)**, **3.6(c)** and **3.8(c)**) obtained from the electrodes that gave diffusion-controlled CVs for cytochrome c. [d] The average and standard deviation of the slopes of logi_p vs log$v$ plots (**Figures 3.5(c)**, **3.6(c)** and **3.8(c)**) obtained from the electrodes that gave CVs reflecting adsorbed cytochrome c. [e] The average and standard deviation of the ratio of i_p/C (i_p: the cathodic and anodic peak currents of cytochrome c and 1,1'-ferrocenedimethanol, respectively, measured at 0.05 V/s; C: the molar concentration of redox species; see Eq (3.9)) obtained from the electrodes that gave diffusion-controlled CVs for cytochrome c. [f] Obtained from the single sample.

3.3.2 CVs on RNEs with CF-PS-b-PMMA-Derived Nanoporous Films

Figure 3.6(a) shows CVs of 1,1'-ferrocenedimethanol on a RNE with 24-nm diameter pores, which were derived from 71K CF-PS-*b*-PMMA. The CVs were peak-shaped and quasi-reversible (i.e., ΔE_p = 145 mV at 0.05 V/s) as with those on planar electrodes. However, the peak current was smaller by the factor of 2–3 [31] than the theoretical prediction for a densely-packed array of nanodisk electrodes [60,61]. The slope in the log–log plot (**Figure 3.6(c)** (open circles)) was significantly smaller than 0.5 (0.29 ± 0.03; **Table 3.1**), suggesting the unavoidable involvement of radial diffusion on individual RNEs. These observations have the following two

possible explanations: First, the density of open nanopores, and thus active nanodisk electrodes, is not high enough to support a perfectly linear diffusion profile [18]. Second, the diffusion coefficient of 1,1'-ferrocenedimethanol within the nanopores is smaller than in bulk solution. Finite-element computer simulations suggest effects from the latter mechanism are more significant (*vide infra*).

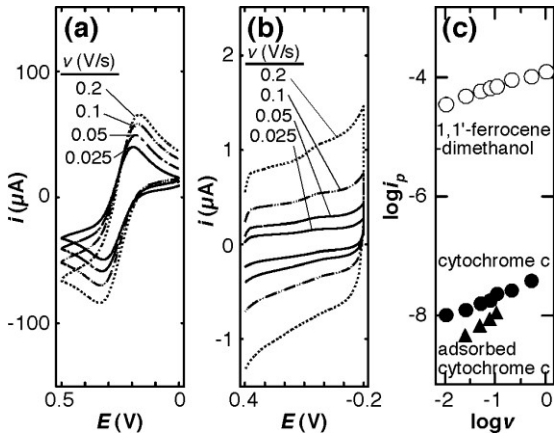

Figure 3.6 Typical CVs (v = 0.025, 0.05, 0.1 and 0.2 V/s) of (a) 3.1 mM 1,1'-ferrocenedimethanol (in 0.1 M KNO_3) and (b) 16 μM cytochrome c (in 75 mM NaH_2PO_4-Na_2HPO_4 buffer (pH 7.0)) on a thioctic acid-modified RNE derived from 71K CF-PS-*b*-PMMA (pore diameter: 24 nm; thickness: 36 nm). (c) Plots of logi_p vs log$v$ (i_p: anodic peak current for 1,1'-ferrocenedimethanol and cathodic peak current for cytochrome c) obtained from the thioctic acid-modified RNE with 24 nm-diameter nanopores.

Figure 3.6(b) shows CVs of cytochrome c on the same RNE. The reduction potential of cytochrome c (36 mV at 0.05 V/s) was close to that measured on the planar electrode (33 mV at 0.05 V/s, **Figure 3.5(b)**), but the ΔE_p was slightly larger (130 vs. 100 mV at 0.05 V/s). The slope in the log–log plot for cytochrome c (**Figure 3.6(c)** (filled circles)) was smaller than 0.5, but was larger than that for 1,1'-ferrocenedimethanol (**Table 3.1**). The larger slope is attributable to contributions from the reduction of adsorbed cytochrome c. Indeed, experiments performed on a RNE that had previously been exposed to cytochrome c also showed a reduction peak for adsorbed species (**Figure 3.7**). In this case, the cell was filled with a buffer containing no cytochrome c. However, the reduction current at the slower v in **Figure 3.6(b)** was mainly determined by cytochrome c diffusing from the solution bulk, as the current from the adsorbed cytochrome c was 20% of the total current at 0.05 V/s (**Figure 3.6(c)** (filled triangles)).

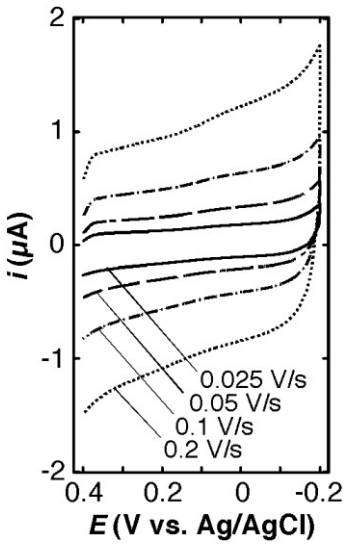

Figure 3.7 CVs (v = 0.025, 0.05, 0.1 and 0.2 V/s) measured in 75 mM NaH_2PO_4-Na_2HPO_4 buffer (pH 7.0) on the thioctic acid-modified RNE after the CV measurements in the cytochrome c solution as shown in Figure 3.6b.

In contrast to RNEs with 24-nm diameter pores, RNEs with the smaller pores gave CVs reflecting adsorbed cytochrome c, as indicated by the statistics (N_{dif}/N_{ads}) given in **Table 3.1**. **Figure 3.8(a)** and **(b)** shows CVs of 1,1'-ferrocenedimethanol and cytochrome c, respectively, on a RNE with 11-nm diameter pores. These were derived from 31K CF-PS-*b*-PMMA. These results show that diffusion-controlled CVs are obtained for 1,1'-ferrocenedimethanol, regardless of pore diameter. The data obtained from 24- and 11- nm pores are similar in terms of their reversibility and peak current values, and produce similar log–log plots (**Figure 3.8(a)**, **Figure 3.8(c)** (open circles) and **Table 3.1**). At first glance, the CVs of cytochrome c shown in **Figure 3.8(b)** appear very similar to those in **Figure 3.6(b)**. However, the slope of the log–log plot was significantly larger than 0.5 (**Figure 3.8(c)** (filled circles) and **Table 3.1**), suggesting that the reduction current measured on these RNEs was largely determined by adsorbed cytochrome c. Most RNEs with 14-nm nanopores also gave CVs reflecting adsorbed cytochrome c (**Table 3.1**). The more frequent observation of adsorption-controlled CVs within the smaller nanopores may reflect the suppressed release of cytochrome c from the SAM surface due to the geometrical diffusion restriction within the confining nanopores. It may also result from the geometrical restrictions imposed by the simultaneous penetration of multiple cytochrome c molecules into single nanopores.

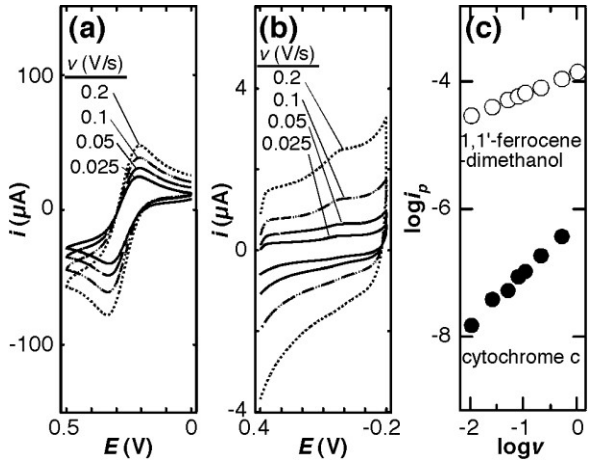

Figure 3.8 Typical CVs (v = 0.025, 0.05, 0.1 and 0.2 V/s) of (a) 3.1 mM 1,1'-ferrocenedimethanol (in 0.1 M KNO_3) and (b) 16 μM cytochrome c (in 75 mM NaH_2PO_4-Na_2HPO_4 buffer (pH 7.0)) on a thioctic acid-modified RNE derived from 31K CF-PS-*b*-PMMA (pore diameter: 11 nm; thickness: 34 nm). (c) Plots of logi_p vs log$v$ (i_p: anodic peak current for 1,1'-ferrocenedimethanol and cathodic peak current for cytochrome c) obtained from the thioctic acid-modified RNE of 11 nm-diameter nanopores.

Table 3.1 summarizes R_{diff}(cytc/FcDM) values for RNEs that gave diffusion-controlled CVs for cytochrome c. The R_{diff}(cytc/FcDM) values (~0.1) were significantly smaller than those obtained on planar thioctic acid-modified electrodes (0.36), suggesting that the effective diffusion coefficient of cytochrome c is decreased more effectively than that of 1,1'-ferrocenedimethanol within the nanopores. This observation is attributable to the larger size of cytochrome c molecules, which leads to greater hindrance of its diffusion within the nanopores. However, the measured R_{diff}(cytc/FcDM) values cannot be used to quantitatively assess $D_{cytc,pore}/D_{FcDM,pore}$ (Eq (3)) because of the contributions of radial diffusion to the measured CVs. For radial diffusion, Eq (2) is not applicable and a limiting current is proportional to D rather than $D^{1/2}$ [60]. The finite-element simulations were thus employed for more quantitative discussion on the decrease in D within the nanopores.

3.3.3 Finite-Element Computer Simulations of CVs on RNEs with 24-nm Diameter Pores

Here, the CVs obtained from the RNEs were simulated using methods previously employed to model CVs from microdisk array electrodes [51,52]. Simulations were performed for 24 nm diameter pores that were 30 nm in length, closely mimicking the properties of pores derived from 71K CF-PS-*b*-PMMA. The simulations were carried out to address the following two questions: (A) What properties of the nanoporous films could lead to the smaller faradic current of 1,1'-ferrocenedimethanol and smaller slopes in the log–log plots as compared to the theoretical prediction [31,60,61]? (B) Can the CVs measured on 71K-CF-PS-*b*-PMMA-derived RNEs provide quantitative information on the diffusion of redox species within the 24-nm nanopores?

Figure 3.2 shows the model geometry used in our simulation of CVs on a RNE comprising hexagonally-distributed nanopores [52]. The simulations were performed by varying the spacing between adjacent pores, $2s$ (s = 22 ~ 1152 nm), or by varying the diffusion coefficient of redox species within the nanopore cavity, D_{pore}. The minimum pore spacing ($2s$ = 44 nm; 280 pores/μm^2) was estimated from the reduction charge for adsorbed cytochrome c (**Figure 3.7**) under the following two assumptions: (i) Only cytochrome c molecules in the first layer could participate in electrode reaction; (ii) Each pore was occupied by 20 cytochrome c molecules, which was estimated from the diameters of the molecule (4 nm) and nanopore (24 nm). The simulated CVs show the relationship between current density defined by the geometrical electrode area and overpotential ($= E - E^0$).

3.3.4 Effects of Interpore Spacing and Diffusion Coefficient within Nanopore Cavity on the CVs of 1,1'-Ferrocenedimethanol

As described in chapter 3, the measured CVs of 1,1'-ferrocenedimethanol on the CF-PS-*b*-PMMA-derived RNEs [31] were not perfectly consistent with the theory which predicts that the peak current for a recessed nanodisk electrode is proportional to the geometrical electrode area rather than the active electrode area [60,61]. The peak current was significantly smaller than that estimated from the geometrical electrode area. The small slope of the log–log plots (0.3~0.4, in **Table 1**) obtained from experimental data suggests that radial diffusion plays a role. The importance of radial diffusion may be enhanced by a larger-than-expected spacing between adjacent nanopores, $2s$ [62], and/or a smaller diffusion coefficient within nanopores, D_{pore}, than in

bulk solution, D_{bulk}. The computer simulations were carried out to verify the effects of these two parameters on CVs.

Figure 3.9(a) shows simulated CVs of 1,1'-ferrocenedimethanol (at 0.05 V/s) on RNEs at different *s* under the assumption of $D_{FcDM,pore} = D_{FcDM,bulk}$ (= 6.4 x 10^{-6} cm^2/s) [57]. It should be noted that the current from all simulated CVs was normalized to the geometrical area rather than the active electrode area. As theoretically predicted [60,61], peak-shaped CVs were obtained for smaller *s*, reflecting the overlapped diffusion layers expanded from individual nanopores. However, the peak current gradually decreased with increasing *s* for $s > 12a$, indicating that the small experimental i_p could be explained by large *s* due to the incomplete removal of degraded polymer from the electrode surface within the nanopores. Indeed, the experimental CVs and log–log plot could be reproduced at *s* = 284 nm (**Figures 3.10(a)** and **3.11**), which corresponds to a much lower pore density (3.6 pores/μm^2) than that estimated from atomic force microscopy (AFM) images of the film surface (700 pores/μm^2) [32]. A further increase in *s* (*s* = 1152 nm) led to a sigmoidal CV, even though the interpore spacing was significantly smaller than the diffusion layer thickness at 0.05 V/s (≈ 26 μm). This result reflects the limitation of the number of molecules that can react on the nanoscale electrode per unit time.

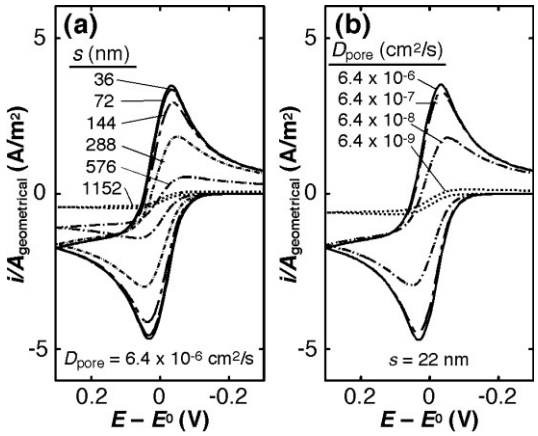

Figure 3.9 Simulated CVs (v = 0.05 V/s) of 3.1 mM 1,1'-ferrocenedimethanol (E^0 = 0.22 V vs. Ag/AgCl) on RNEs. (a) CVs obtained at different interpore spacing (*s* = 36 nm – 1152 nm) with $D_{FcDM,pore} = D_{FcDM,bulk}$. Note that almost identical CVs were obtained at *s* < 72 nm. (b) CVs at *s* = 22 nm with different $D_{FcDM,pore}$ (6.4 x 10^{-6} cm^2/s – 6.4 x 10^{-9} cm^2/s). The current was normalized to the geometrical electrode area. Simulations performed by Khanh Hoa Tran Ba.

Figure 3.9(b) shows simulated CVs of 1,1'-ferrocenedimethanol (at 0.05 V/s) on a RNE at different $D_{FcDM,pore}$ and constant s (= 22 nm). For $D_{FcDM,pore} \geq 0.1D_{FcDM,bulk}$, peak-shaped CVs with i_p close to the theoretically predicted value were observed. In contrast, for $D_{FcDM,pore} < 0.1D_{FcDM,bulk}$, i_p decreased with decreasing $D_{FcDM,pore}$ probably because i_p was more dominantly controlled by diffusion rather than electrode reaction kinetics. Simulation results consistent with the experimental CVs and log–log plot were obtained at $D_{FcDM,pore} = 6.7 \times 10^{-8}$ cm^2/s (**Figures 3.10(b)** and **3.11**), two orders of magnitude smaller than $D_{FcDM,bulk}$. The very small $D_{FcDM,pore}$ is experimentally possible if the molecular diffusion is obstructed based on chemical and steric interactions, in particular, due to the incomplete removal of the PMMA domains or imperfect cylindrical shape.

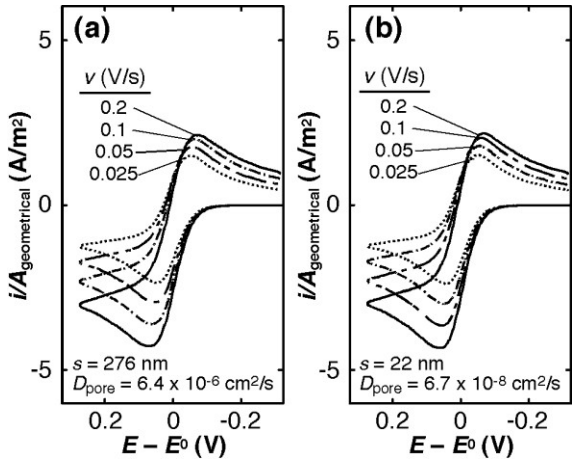

Figure 3.10 Simulated CVs of 1,1'-ferrocenedimethanol (3.1 mM) on RNEs (pore diameter: $2a$ = 24 nm; pore length: L = 30 nm) at different scan rates: (a) s = 276 nm, $D_{FcDM,pore}$ = 6.4 x 10^{-6} cm^2/s; (b) s = 22 nm, $D_{FcDM,pore}$ = 6.7 x 10^{-8} cm^2/s. Simulations performed by Khanh Hoa Tran Ba.

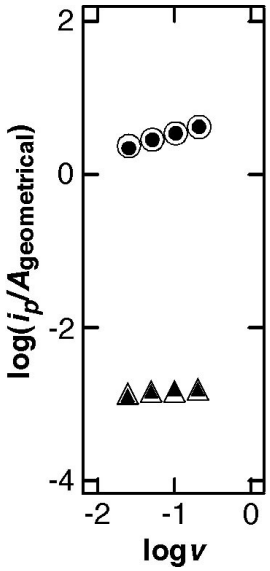

Figure 3.11 Plots of log($i_p/A_{geometrical}$) vs log$v$ (i_p: anodic peak current for 1,1'-ferrocenedimethanol and cathodic peak current for cytochrome c) obtained from the RNEs simulated in Figure 3.10 and Figure 3.12: 1,1'-ferrocenedimethanol at s = 22 nm (open circles); 1,1'-ferrocenedimethanol at s = 276 nm (filled circles); cytochrome c at s = 22 nm (open triangles); cytochrome c at s = 276 nm (filled triangles). The experimental data for cytochrome c (Figure 3.3b in chapter 3) showed a larger slope probably due to the contribution of adsorbed cytochrome c molecules to the measured reduction current. Simulations performed by Khanh Hoa Tran Ba.

These simulation results suggest that the experimental CVs of 1,1'-ferrocenedimethanol on the RNEs reflect lower pore density and/or small $D_{FcDM,pore}$. However, it was not possible to obtain specific pore density and $D_{FcDM,pore}$ values by simple comparison of the experimental and simulated CVs of 1,1'-ferrocenedimethanol, because these two parameters independently affect CVs as indicated by **Figure 3.9**.

3.3.5 Diffusion of Cytochrome c within 24-nm-Diameter Nanopores

Subsequently, CVs of cytochrome c on RNEs comprising 24-nm diameter pores were simulated to estimate $D_{cytc,pore}$ from the experimental data. Then, the $D_{cytc,pore}$ values were compared with the hindered diffusion coefficient $D_{cytc,hindered}$ obtained using the Renkin equation.[43]

$$\frac{D_{hindered}}{D_{bulk}} = (1-\lambda)^2(1-2.1044\lambda+2.089\lambda^3-0.948\lambda^5) \qquad (3.12)$$

where $D_{hindered}$ and D_{bulk} are the hindered and bulk diffusion coefficients respectively, and λ (= r_s/r_p) is the solute-to-pore size ratio.

For cytochrome c within 24-nm diameter pores, the ratio of solute diameter to pore diameter, λ, is 0.16, and $D_{cytc,hindered} = 5.2 \times 10^{-7}$ cm^2/s. The following two models were examined, because they provided simulated CVs of 1,1'-ferrocenedimethanol similar to the experimental ones (*vide supra*): RNEs with s = 284 nm (Model A) and s = 22 nm (Model B).

Figure 3.12(a) shows simulated CVs of cytochrome c under Model A at different $D_{cytc,pore}$. The reduction peak current decreased with decreasing $D_{cytc,pore}$, and the experimentally observed R_{diff}(cytc/FcDM) (~ 0.1) was obtained at $D_{cytc,pore} = 2.4 \times 10^{-7}$ cm^2/s. The obtained $D_{cytc,pore}$ was close to $D_{cytc,hindered}$. However, as compared with experimental CVs showing the reduction peak potential close to that on planar electrodes (**Figure 3.5(b)** vs. **Figure 3.6(b)**), the simulated CV at the $D_{cytc,pore}$ exhibited a reduction peak at more negative potential.

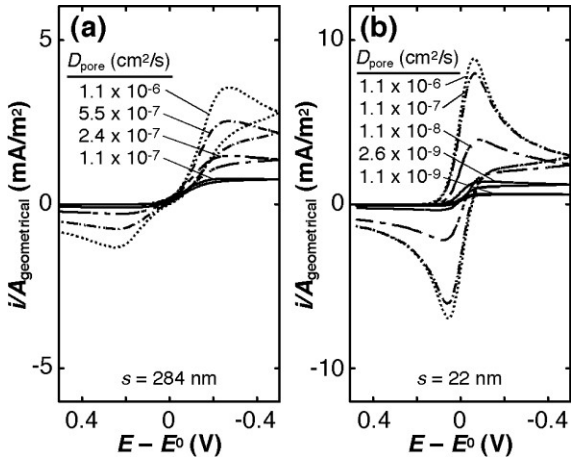

Figure 3.12 Simulated CVs (v = 0.05 V/s) of 16 μM cytochrome c (E^0 = 0.01 V vs. Ag/AgCl) on RNEs at different $D_{cytc,pore}$. (a) s = 284 nm; (b) s = 22 nm. The current was normalized to the geometrical electrode area. Simulations performed by Khanh Hoa Tran Ba.

Figure 3.12(b) shows simulated CVs of cytochrome c under Model B at different $D_{cytc,pore}$. The reduction peak current decreased at the smaller $D_{cytc,pore}$, and the experimentally observed R_{diff}(cytc/FcDM) (~ 0.1) could be obtained at $D_{cytc,pore} = 2.6 \times 10^{-9}$ cm^2/s. The obtained $D_{cytc,pore}$ was much smaller than $D_{cytc,hindered}$. However, the reduction peak potential was close to that observed in the experimental CVs (**Figure 3.6(b)**). This result suggests that the properties of the

nanoporous film are closer to Model B: The pore density was relatively high and D_{pore} of redox species was smaller than D_{bulk}.

Importantly, both models showed a greater reduction in D_{pore} for cytochrome c as compared to 1,1'-ferrocenedimethanol. $D_{FcDM,pore}/D_{cytc,pore}$ values obtained from simulations based on Models A and B were 27 and 26, respectively. These are 4-5 times larger than $D_{FcDM,bulk}/D_{cytc,bulk}$ (= 5.8). Thus, regardless of the model, it can be concluded that the smaller R_{diff}(cytc/FcDM) on the RNEs results from a greater decrease in the effective diffusion coefficient of cytochrome c within the nanopores. The decrease in D_{pore} for cytochrome c reflects chemical interactions between cytochrome c and the nanopore surface in addition to hindered diffusion, considering that the latter reduces diffusion coefficient by the factor of 2 ($D_{cytc,hindered}/D_{cytc,bulk}$ = 0.47 for λ = 0.16). The residual surface –COOH groups on CF-PS-*b*-PMMA-derived nanopores functionalized with poly(ethylene glycol) moieties [32] could lead to smaller R_{diff}(cytc/FcDM) values through electrostatic interactions with cationic cytochrome c molecules (pI ~ 11) [39] at pH 7.

3.4 Conclusions

This study reports diffusion of cytochrome c within the nanopores of block copolymer-derived RNEs. The results were compared to those obtained for 1,1'-ferrocenedimethanol diffusion through the same nanopores. Finite element simulations afforded the means to estimate diffusion coefficients and pore spacings by comparison with the experimental data. The results also showed the difference in diffusion behavior of the biomolecule according to the diameters of the nanopores. Although cytochrome c molecules could penetrate through the nanopores and reach the underlying electrodes, they were more strongly adsorbed onto the smaller RNE nanopores. Within 24-nm diameter nanopores, cytochrome c exhibited diffusion-controlled CVs. However, its effective diffusion coefficient was greatly decreased due to chemical interactions with negatively-charged nanopores in addition to steric effect. The results reported in this study will provide guidance in designing RNEs for size-based chemical sensing [18,33] and also for controlled immobilization of biomolecules within nanoporous media for biosensors and bioreactors [20,63].

It should be noted that the results obtained in the present study differ somewhat from those of "flow-through" nanopores. In flux measurements with flow-through nanopores, the protein

concentration at the exits is defined by that in the receiving solution, and thus keeps being significantly lower than that at the blocked end of RNE nanopores. The low concentration of the receiving solution probably made it possible to observe single-file protein diffusion with negligible nonspecific adsorption of proteins onto the nanopores [13].

References

(1) Ito, T.; Perera, D. In *Trace Analysis with Nanomaterials*; Pierce, D. T., Zhao, J. X., Eds.; Wiley-VCH: Weinheim, 2010, p 341.

(2) Jackson, E. A.; Hillmyer, M. A. *ACS Nano* **2010**, *4*, 3548.

(3) Hillmyer, M. A. *Adv. Polym. Sci.* **2005**, *190*, 137.

(4) Olson, D. A.; Chen, L.; Hillmyer, M. A. *Chem. Mater.* **2008**, *20*, 869.

(5) Bang, J.; Jeong, U.; Ryu, D. Y.; Russell, T. P.; Hawker, C. J. *Adv. Mater.* **2009**, *21*, 4769.

(6) Deen, W. M. *AIChE J.* **1987**, *33*, 1409.

(7) Yu, S.; Lee, S. B.; Kang, M.; Martin, C. R. *Nano Lett.* **2001**, *1*, 495.

(8) Baker, L. A.; Jin, P.; Martin, C. R. *Crit. Rev. Solid State Mater. Sci.* **2005**, *30*, 183.

(9) Bruening, M. L.; Dotzauer, D. M.; Jain, P.; Ouyang, L.; Baker, G. L. *Langmuir* **2008**, *24*, 7663.

(10) Yang, S. Y.; Ryu, I.; Kim, H. Y.; Kim, J. K.; Jang, S. K.; Russell, T. P. *Adv. Mater.* **2006**, *18*, 709.

(11) Yang, S. Y.; Park, J.; Yoon, J.; Ree, M.; Jang, S. K.; Kim, J. K. *Adv. Funct. Mater.* **2008**, *18*, 1371.

(12) Nuxoll, E. E.; Hillmyer, M. A.; Wang, R.; Leighton, C.; Siegel, R. A. *ACS Appl. Mater. Interfaces* **2009**, *1*, 888.

(13) Yang, S. Y.; Yang, J.-A.; Kim, E.-S.; Jeon, G.; Oh, E. J.; Choi, K. Y.; Hahn, S. K.; Kim, J. K. *ACS Nano* **2010**, *4*, 3817.

(14) Phillip, W. A.; Rzayev, J.; Hillmyer, M. A.; Cussler, E. L. *J. Membr. Sci.* **2006**, *286*, 144.

(15) Phillip, W. A.; O'Neill, B.; Rodwogin, M.; Hillmyer, M. A.; Cussler, E. L. *ACS Appl. Mater. Interfaces* **2010**, *2*, 847.

(16) Majda, M. In *Molecular Design of Electrode Surfaces*; Murray, R. W., Ed.; Wiley & Sons: New York, 1992, p 159.

(17) Andrieux, C. P.; Saveant, J.-M. In *Molecular Design of Electrode Surfaces*; Murray, R. W., Ed.; Wiley & Sons: New York, 1992, p 207.

(18) Chailapakul, O.; Crooks, R. M. *Langmuir* **1995**, *11*, 1329.

(19) Massari, A. M.; Gurney, R. W.; Schwartz, C. P.; Nguyen, S. T.; Hupp, J. T. *Langmuir* **2004**, *20*, 4422.

(20) Walcarius, A.; Mandler, D.; Cox, J. A.; Collinson, M.; Lev, O. *J. Mater. Chem.* **2005**, *15*, 3663.

(21) Newton, M. R.; Bohaty, A. K.; White, H. S.; Zharov, I. *J. Am. Chem. Soc.* **2005**, *127*, 7268.

(22) Miller, C. J.; Majda, M. *J. Am. Chem. Soc.* **1985**, *107*, 1419.

(23) Miller, C. J.; Widrig, C. A.; Charych, D. H.; Majda, M. *J. Phys. Chem.* **1988**, *92*, 1928.

(24) Brumlik, C. J.; Martin, C. R.; Tokuda, K. *Anal. Chem.* **1992**, *64*, 1201.

(25) Ikeda, O.; Ohtani, M.; Yamaguchi, T.; Komura, A. *Electrochim. Acta* **1998**, *43*, 833.

(26) Kralj, B.; Dryfe, R. A. W. *Phys. Chem. Chem. Phys.* **2001**, *3*, 3156.

(27) Ito, T.; Audi, A. A.; Dible, G. P. *Anal. Chem.* **2006**, *78*, 7048.

(28) Zoski, C. G.; Yang, N.; He, P.; Berdondini, L.; Koudelka-Hep, M. *Anal. Chem.* **2007**, *79*, 1474.

(29) Perera, D. M. N. T.; Ito, T. *Analyst* **2010**, *135*, 172.

(30) Jeoung, E.; Galow, T. H.; Schotter, J.; Bal, M.; Ursache, A.; Tuominen, M. T.; Stafford, C. M.; Russell, T. P.; Rotello, V. M. *Langmuir* **2001**, *17*, 6396.

(31) Li, Y.; Maire, H. C.; Ito, T. *Langmuir* **2007**, *23*, 12771.

(32) Li, Y.; Ito, T. *Langmuir* **2008**, *24*, 8959.

(33) Li, Y.; Ito, T. *Anal. Chem.* **2009**, *81*, 851.

(34) Maire, H. C.; Ibrahim, S.; Li, Y.; Ito, T. *Polymer* **2009**, *50*, 2273.

(35) Thurn-Albrecht, T.; Steiner, R.; DeRouchey, J.; Stafford, C. M.; Huang, E.; Bal, M.; Tuominen, M.; Hawker, C. J.; Russell, T. P. *Adv. Mater.* **2000**, *12*, 787.

(36) Perera, D. M. N. T.; Pandey, B.; Ito, T. *Langmuir* **2011**, DOI: 10.1021/la202005n.

(37) Ibrahim, S.; Ito, T. *Langmuir* **2010**, *26*, 2119.

(38) Li, F.; Diaz, R.; Ito, T. *RSC Adv.* **2011**, DOI:10.1039/C1RA00471A.

(39) Fedurco, M. *Coord. Chem. Rev.* **2000**, *209*, 263.

(40) Rusling, J. F.; Wang, B.; Yun, S.-E. In *Bioelectrochemistry: Fundametals, Experimental Techniques and Applications*; Bartlett, P. N., Ed.; John Wiley & Sons: Chichester, England, 2008, p 39.

(41) Pyon, M.-S.; Cherry, R. J.; Bjornsen, A. J.; Zapien, D. C. *Langmuir* **1999**, *15*, 7040.

(42) Sarkar, R.; Shaw, A. K.; Narayanan, S. S.; Dias, F.; Monkman, A.; Pal, S. K. *Biophys. Chem.* **2006**, *123*, 40.

(43) Davidson, M. G.; Deen, W. M. *Macromolecules* **1988**, *21*, 3474.

(44) Brautigan, D. L.; Ferguson-Miller, S.; Margoliash, E. *Methods Enzymol.* **1978**, *53*, 128.

(45) Song, S.; Clark, R. A.; Bowden, E. F.; Tarlov, M. J. *J. Phys. Chem.* **1993**, *97*, 6564.

(46) Goto, Y.; Hagihara, Y.; Hamada, D.; Hoshino, M.; Nishii, I. *Biochemistry* **1993**, *32*, 11878.

(47) Senaratne, W.; Andruzzi, L.; Ober, C. K. *Biomacromolecules* **2005**, *6*, 2427.

(48) Cheng, Q.; Brajter-Toth, A. *Anal. Chem.* **1992**, *64*, 1998.

(49) Perera, D. M. N. T.; Nagasaka, S.; Ito, T. *Supramol. Chem.* **2010**, *22*, 450.

(50) Jeong, U.; Ryu, D. Y.; Kim, J. K.; Kim, D. H.; Russell, T. P.; Hawker, C. J. *Adv. Mater.* **2003**, *15*, 1247.

(51) Lavacchi, A.; Bardi, U.; Borri, C.; Caporali, S.; Fossati, A.; Perissi, I. *J. Appl. Electrochem.* **2009**, *39*, 2159.

(52) Davies, T. J.; Compton, R. G. *J. Electroanal. Chem.* **2005**, *585*, 63.

(53) Sun, P.; Mirkin, M. V. *Anal. Chem.* **2006**, *78*, 6526.

(54) Wang, Q.; Li, N. *Electroanalysis* **2001**, *13*, 1375.

(55) Zhang, B.; Zhang, Y.; White, H. S. *Anal. Chem.* **2004**, *76*, 6229.

(56) Guo, J.; Lindner, E. *J. Electroanal. Chem.* **2009**, *629*, 180.

(57) Fan, F.-R. F. *J. Phys. Chem. B* **1998**, *102*, 9777.

(58) Tarlov, M. J.; Bowden, E. F. *J. Am. Chem. Soc.* **1991**, *113*, 1847.

(59) Ji, X.; Jin, B.; Jin, J.; Nakamura, T. *J. Electroanal. Chem.* **2006**, *590*, 173.

(60) Bard, A. J.; Faulkner, L. R. *Electrochemical Methods, Fundamentals and Applications, 2nd Ed.*; Wiley: New York, 2001.

(61) Amatore, C.; Saveant, J.-M.; Tessier, D. *J. Electroanal. Chem.* **1983**, *147*, 39.

(62) Bartlett, P. N.; Taylor, S. L. *J. Electroanal. Chem.* **1998**, *453*, 49.

(63) Oliver, B. N.; Egekeze, J. O.; Murray, R. W. *J. Am. Chem. Soc.* **1988**, *110*, 2321.

Chapter 4 - Formation of Self- Organized Nanoporous Anodic Oxide from Metallic Gallium

Reproduced by permission of the American Chemical Society.
Published as: Pandey, B.; Thapa, P.S.; Higgins, D. A.; Ito, T. *Langmuir*, **2012**, *28*, 13705-13711.

4.1 Introduction

In recent years, development of an efficient and technologically simple method for the synthesis of nanostructures over a macroscopic area has been a topic of great interest.[1] Self-organized materials with a periodic arrangement of nanopores have drawn a lot of attention due to the high expectations regarding their applications.[2] The uniform, highly dense and ordered cylindrical nanopores in these materials have been employed as templates for the synthesis of nanowires and nanotubes[3,4] that have in turn been applied for electrochemical energy storage[5] and drug delivery.[6] In addition, uniform cylindrical nanopores penetrating through the materials have led to highly-selective chemical separations based on steric and chemical interactions.[2] Furthermore, the well-defined nanoporous structures are suitable for investigating fundamental relationships between materials morphologies and mass/charge transport characteristics.[7]

Anodization of metal substrates/films has been employed as a simple approach to fabricate monolithic material comprising a densely-packed array of cylindrical nanopores.[8-11] Formation of nanoporous anodic oxides has been widely studied for aluminum.[8,9] More recently, nanoporous anodic oxides have also been formed from other valve metals (e.g. Ti, W) and their alloys, tin[13] and iron.[12,14] However, metallic gallium has not been examined for anodic formation of its self-organized nanoporous oxide, in spite of its similar chemical properties to aluminum,[15] including the formation of compact barrier-type oxides on the metal surface.[16,17] Since the melting point of gallium is much lower (29.8 °C) than that of aluminum (660.3 °C),[18] metallic gallium can be easily incorporated into microscale channels.[19] Thus, if anodization of metallic gallium leads to the formation of self-organized nanoporous structures, the resulting nanoporous oxide can be flexibly fabricated within confined spaces such as the inside of microfluidic devices. The integration of nanoporous anodic oxides with microfluidics will lead to development of unique portable devices because of the well-defined nanoporous structures

and the physicochemical properties of the oxide as well as the controlled flow profiles in the microchannels.

Gallium oxide is a wide-band-gap semiconductor (band gap ~ 4.8 eV) that can be employed for optoelectronic devices,[20] high-temperature stable gas sensors[21,22] and heterogeneous photocatalysis.[23,24] Controlled fabrication of gallium oxide in various nanoscale structures is important for these applications, as the shape and size have significant influence on the semiconductor properties.[25] The large effective surface area of nanostructured materials can enhance the performance in their applications for chemical sensing and catalysis. Previously, nanoporous gallium oxides were prepared via template-based methods with mesoporous carbon[26] and surfactant micelles.[27] Though these approaches could provide gallium oxide monoliths comprising nanopores with controlled nanoscopic shapes and diameters, it was challenging to obtain well-aligned nanopores with μm-scale thickness over a wide area. Anodization is a promising method for fabricating well-ordered, large-area nanoporous structures, as mentioned above.

In this study, anodization of solid metallic gallium films deposited on planar Si substrates was examined at different voltages and H_2SO_4 concentrations to reveal the optimal conditions required for formation of self-organized nanoporous gallium oxides. The current generated during anodization was monitored to obtain insight into the formation of the nanoporous structures. The morphology and elemental composition of anodized gallium films were measured with field-emission scanning electron microscopy (SEM) and energy dispersive X-ray spectrometry (EDX). In addition to planar films, a solid gallium monolith incorporated at the end of a glass capillary was anodized to demonstrate the formation of nanoporous anodic gallium oxide in confined structures. The materials and methods described will be useful for the fabrication of well-defined nanoporous materials within microchannels for possible applications in chemical separations and catalysis.

4.2 Experimental

4.2.1 Chemicals and Materials

All solutions were prepared with water having a resistivity of 18 MΩ cm or higher (Barnstead Nanopure Systems). High purity gallium (99.99 %) was purchased from

GalliumSource, LLC and used as received. Sulfuric acid (Fisher Chemical, Certified ACS Plus) was used without purification. Si (100) wafers (p-type) and borosilicate Pasteur pipettes were purchased from University Wafer and Fisher Scientific, respectively.

4.2.2 Fabrication of a Solid Gallium Film on a Planar Si Substrate

Under Ar atmosphere, a drop of liquid gallium was placed on a planar Si substrate (ca. 12 mm × 12 mm; cleaned in a Novascan PSD-UVT UV-ozone system for 30 min prior to use) and was spread over the whole surface. The gallium-coated surface was placed on a sterile polystyrene petridish (100 mm × 15 mm, Fisher Scientific), and then cooled on an ice pack. The substrate with frozen gallium film was detached from the petridish to obtain a mirror-like solid gallium film immobilized on a planar Si substrate. A piece of conductive copper tape (Electron Microscopy Science) was attached onto the edge of the gallium surface to make an electrical connection.

4.2.3 Fabrication of a Solid Gallium Monolith inside a Glass Capillary

Under Ar atmosphere, a small plug of liquid gallium was sucked up very carefully into the narrower end of a Pasteur pipette (1.75 mm I.D.; cleaned with Harrick plasma cleaner for 5 min prior to use) using a pipette bulb. A small piece of copper wire was dipped into the gallium to make an electrical connection. The distance between the end of copper wire and the gallium surface was adjusted to be *ca.* 1 mm using a micromanipulator. Then, the narrower end of the pipette was contacted to the surface of a polystyrene petridish on an ice pack to obtain a solid metallic gallium monolith.

4.2.4 Anodization of Metallic Gallium

Metallic gallium samples were anodized in two-electrode cells shown in **Scheme 1** with a NuVant EZstat-HV potentiostat/galvanostat (applied voltage ≤ 25 V) or a CH Instruments Model 618B electrochemical analyzer (applied voltage ≤ 10 V). Planar gallium films immobilized on Si substrates were placed at the bottom of the cell (**Scheme 1a**). The diameter of an O-ring, which defined the gallium surface area for anodization, was 0.80 cm. Capillary-incorporated gallium monoliths were dipped into H_2SO_4 solution as shown in **Scheme 1b**. Both the gallium electrode and aqueous H_2SO_4 solution were cooled by ice (ca. 0 °C, measured with a

thermometer) to prevent the gallium from melting. Anodization was performed at a constant dc voltage. The current flowing between the gallium anode and a carbon cathode (0.5 mm in diameter and dipped *ca.* 1 cm into the solution) was monitored during anodization. The effects of anodization voltage were studied in 4 M H_2SO_4 solution at four different voltages (1, 5, 10 and 15 V), while the dependence on H_2SO_4 concentration (1, 2, 4 and 6 M) was investigated at 10 V. After anodization, the gallium samples were thoroughly rinsed with ultra pure water and dried in N_2.

Scheme 1

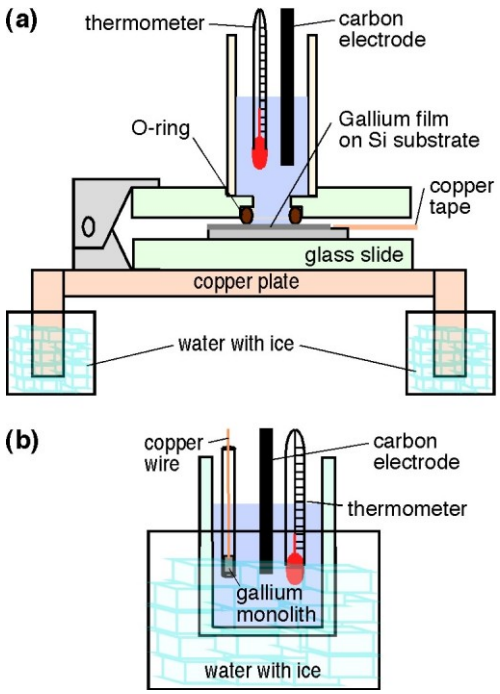

4.2.5 ICP-AES Measurements

The aqueous H_2SO_4 electrolyte solution after anodization was analyzed for the total amount of gallium species using inductively coupled plasma-atomic emission spectroscopy (ICP-AES). The measured total gallium species was compared with the amount of oxidized gallium to estimate the dissolution of oxidized gallium into the electrolyte solution. ICP-AES measurements were performed by Ms. Ranju Karna (Department of Agronomy, Kansas State University). A calibration curve was obtained using a series of Ga^{3+} standard solutions containing 3.67, 18.32, 36.67, 73.31 and 219.95 ppm Ga^{3+} respectively. To determine the Ga^{3+} in the aqueous H_2SO_4

electrolyte solution used during anodization, 10 μL sample solution was diluted to 10 mL using the acetate buffer, pH 3.5. The emission of the sample was recorded and the concentration estimated using the calibration curve.

4.2.6 SEM and EDX Measurements

A LEO 1550 field-emission scanning electron microscope at the Microscopy and Analytical Imaging Laboratory, University of Kansas was employed to obtain the surface and cross-sectional morphology as well as EDX data of anodized gallium samples. These samples were mounted on a holder with double sided conductive carbon tape (Electron Microscopy Sources). For cross-sectional imaging, the samples were fractured and similarly mounted on a holder. SEM images were obtained at an acceleration voltage ranging from 1 – 10 with an in-lens detector. EDX data were obtained using an EDX detector at an acceleration voltage of 10 kV. SEM images were analyzed with ImageJ (a public domain program developed at the RSB of NIH, USA).

4.3 Results and Discussion

In this study, solid metallic gallium was anodized in an ice-cooled aqueous H_2SO_4 solution to investigate the effects of the anodizing conditions on the resulting oxide morphology. H_2SO_4 was employed because it has been reported that nanoporous anodic aluminum oxides were obtained at relatively low anodization voltages with H_2SO_4 as an electrolyte.[10] A low anodization voltage leads to less heat generation, which is essential to keep the gallium samples from melting. Indeed, we found that a solid gallium film was removed from the underlying substrate upon anodization in an ice-cooled solution at 20 V due to melting of the metal by local Joule heating, as liquid gallium was found at the bottom of the cell. In addition, it was theoretically shown that molten metals could not provide nanoporous anodic oxides because of the absence of morphological irregularity, which was required for self-organized nanopore formation.[28]

Here, we will first discuss results obtained from planar gallium films at different anodization voltages and H_2SO_4 concentrations, and then from a capillary-incorporated gallium monolith.

4.3.1 Current–Time Curves at Different Anodization Voltage

Figure 4.1 shows typical current–time (*i–t*) curves recorded during the anodization of planar gallium films in 4 M H_2SO_4 at different anodization voltages. At 1 V, the anodic current was very small and almost constant. At higher anodization voltages, an initial large anodic current followed by a gradual decrease were observed. The gradual decrease in anodic current was due to the formation of a barrier oxide layer. In addition, the *i–t* curves at 10 and 15 V showed an increase in anodic current after the gradual current decrease, as indicated by the arrows in **Figure 4.1**. The time at which this current increase occurred became shorter at higher voltages (*ca.* 1000 sec and *ca.* 500 sec at 10 V and 15 V, respectively). The current increase reflects an increase in oxide surface area due to the formation of nanoporous structures, as reported in the anodization of metallic aluminum.[29] However, longer anodization was required to observe the current increase for gallium, probably reflecting the lower solubility of gallium oxide as compared to aluminum oxide (e.g., the solubility product constants of $Ga(OH)_3$ and $Al(OH)_3$ are 7.28 x 10^{-36} and 1.3 x 10^{-33}, respectively).[18]

It should be noted that the majority of the oxidized gallium was dissolved into the H_2SO_4 solution. Indeed, the amount of oxidized gallium, which was estimated from the anodization charge, was comparable to that of gallium species released into the aqueous solution during the anodization, as determined by atomic emission spectroscopy (*vide infra*). As a result of gallium oxide dissolution into the highly acidic solution, the thickness of the nanoporous oxide layer was significantly smaller (e.g., 2 μm) than that estimated from the anodization charge (e.g., 16 μm).

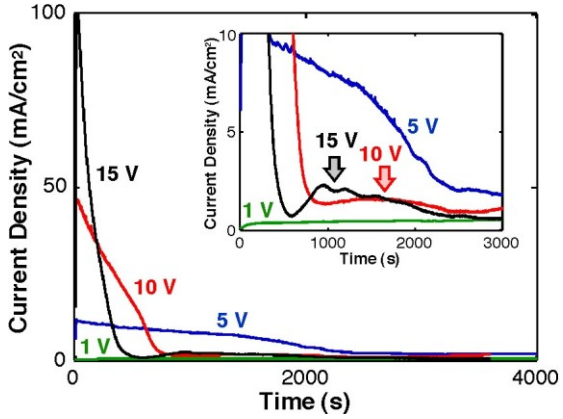

Figure 4.1 Typical current–time (*i–t*) curves for anodization of planar gallium films on Si substrates in 4 M H_2SO_4 at different anodization voltages. The geometrical area used were those defined by the O-ring (0.80 cm in diameter).

The dissolution of the oxidized gallium into the H_2SO_4 solution was verified using ICP-AES. As shown in **Figure 4.2**, a standard calibration curve for Ga^{3+} was obtained using a series of standard solutions.

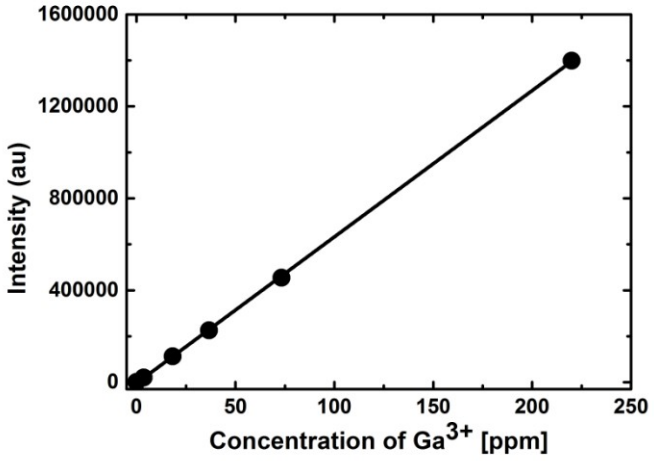

Figure 4.2 Calibration curve for standard solutions of Ga^{3+} measured using ICP-AES.

To determine the Ga^{3+} in the solution used during anodization, 10 μL sample solution was diluted to 10 mL using the acetate buffer, pH 3.5. The emission of the sample was recorded and the concentration estimated using the calibration curve.

The concentration of unknown from ICP-AES was calculated to be 4.20 ppm. Therefore, actual concentration in the undiluted anodized solution is 4.20 × 1000 (dilution factor) = 4200 ppm = 4200 mg/L Ga^{3+}.

$$\text{\# mmol of } Ga^{3+} \text{ in the anodized solution} = \frac{4200 mg Ga^{3+}}{L} \times \frac{1 mol Ga^{3+}}{69.73 g Ga^{3+}} \times 0.0015 L = 90.35 \times 10^{-3}$$

mmoles. It has to be noted that 0.0015 L was the total volume of the H_2SO_4 used for anodization. The number of mmol of Ga^{3+} in the anodized solution was quite comparable to the amount estimated from the charge of the *i-t* curve which was ca. 72.61×10^{-3} mmol.

4.3.2 SEM Images of a Gallium Film Anodized in 4 M H2SO4 at 10 V

Figure 4.3(a) shows a low-magnification SEM image of the surface of a planar gallium film anodized in 4 M H_2SO_4 at 10 V for one hour. There were rough and smooth regions on the sample surface. Importantly, these two types of regions exhibited different nanoscopic surface

morphologies. The smooth regions showed hexagonally-distributed circular nanopores with uniform diameters (**Figure 4.3(b)**), whereas the rough regions showed less organized nanoporous structures (**Figure 4.3(c)**). The formation of rough and smooth regions in the anodized film may originate from heterogeneous surface structures and/or the presence of impurities such as gallium oxide and/or contaminants in the solid gallium film. We have found that a smooth surface is required to obtain well-ordered nanoporous structures: The SEM images shown in **Figure 4.3(b)** could be obtained only on a mirror-like solid gallium film, but not on cloudy films. The following discussion of the nanoscopic surface features of anodized gallium films will be based on SEM images measured in smooth regions alone.

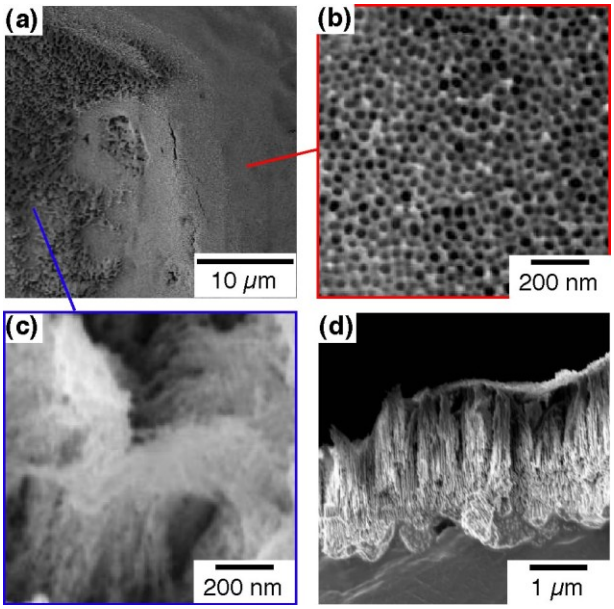

Figure 4.3 SEM images of planar gallium films on Si substrates after anodization in 4 M H_2SO_4 at 10 V. The *i–t* curve recorded during anodization of a sample for Figure 4.3a-c is shown in Figure 4.1, and that of a sample for Figure 4.3d is shown in Figure 4.3. (a) Measured at low-magnification, showing smooth and rough regions. (b) High-magnification image obtained from a smooth region. (c) High-magnification image obtained from a rough region. (d) Cross-sectional view of a planar gallium film. Anodized gallium oxide appears brighter in the image.

The diameter of the nanopores measured in the smooth regions of planar gallium films anodized in 4 M H_2SO_4 at 10 V for one hour was 28 ± 5 nm (**Table 4.1**). The small relative standard deviation (*ca*. 17%) indicates that the pore diameter was uniform, as is observed for anodic alumina nanopores. This pore diameter is also similar to those of anodic alumina nanopores obtained at high H_2SO_4 concentrations and similar voltages.[30] It has been reported that tensile stress at the metal-oxide interface, which originates from the volume expansion involved in anodic oxide formation, affects defect density and pore diameter in nanoporous anodic alumina.[31] Considering the closer density between solid gallium and its oxide as compared with their aluminum counterparts (2.7 and 4.0 g/cm^3 for Al and □-Al_2O_3; 5.9 and ≈6 g/cm^3 for Ga and Ga_2O_3),[32] tensile stress for gallium anodization may be smaller. Observation of similar pore diameters for anodized gallium and aluminum however suggests a minor influence of tensile stress on the pore parameters. On the other hand, the pore diameter increased upon longer anodization due to the dissolution of gallium oxide into the H_2SO_4 solution: As shown in **Figure 4.4**, the pore diameter obtained upon anodization for two hours was 32 ± 6 nm.

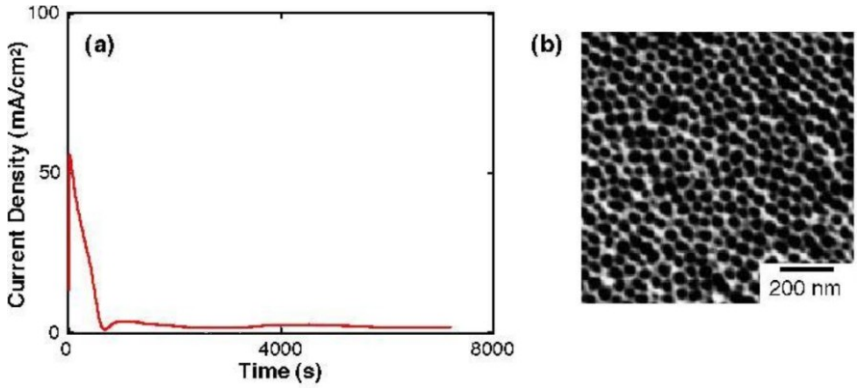

Figure 4.4 (a) An *i-t* curve for anodization of a planar gallium film on a Si substrate at 10 V in aqueous 4 M H_2SO_4 for 2 hours. (b) An SEM image of the planar gallium film anodized at 10 V in 4 M H_2SO_4 for 2 hours. The cross-sectional view of this sample is shown in Figure 2d.

The cross-sectional SEM image of the fractured sample (**Figure 4.3(d)**) revealed nanopores aligned vertically to the film surface, *i.e*., parallel to the applied electric field, and extended down to a depth of ~ 2 μm. The thickness of the nanoporous layer is probably limited

by the relatively quick dissolution of anodic oxide at the high H_2SO_4 concentration (*vide supra*), as has been described previously for anodic titanium oxide nanopores/nanotubes.[11]

The elemental composition determined by EDX (**Figure 4.5(a)**) indicated the anodic formation of gallium oxide: The atomic % of Ga and O was found to be 40% Ga and 52% O, which were reasonably close to the expected values of 40% Ga and 60% O. The smaller oxygen content may originate from the acquisition of signals from the underlying metallic gallium film. The detection of sulfur (< 3%) suggests the presence of SO_4^{2-} impurity in the material. These results clearly indicate that self-organized nanoporous gallium oxide films can be obtained via anodization of smooth solid gallium surfaces in 4 M H_2SO_4 at 10 V.

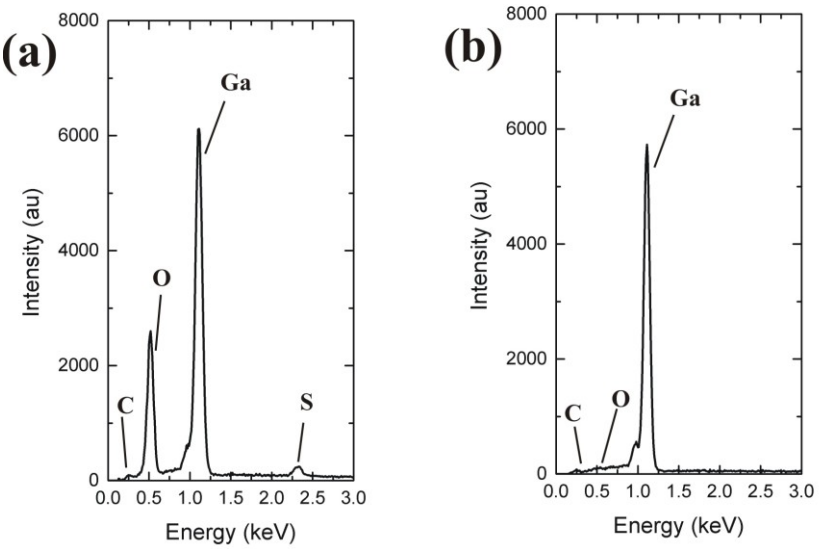

Figure 4.5 (a) EDX spectrum measured on a planar gallium film anodized at 10 V with 4 M H_2SO_4 for one hour. The surface morphology is shown in Figure 4.3abc. (b) EDX spectrum measured on a planar gallium film anodized at 1 V with 4 M H_2SO_4 for 2 hours. The surface morphology is shown in Figure 4.6cd.

4.3.3 Effects of Anodization Voltages on Surface Morphology

The surface features of the samples anodized at different voltages were examined with SEM. **Figure 4.6(a)** and (**b)** shows the low- and high-magnification images of a planar solid gallium film before anodization. The surface is smooth overall, but some features that may reflect those of the plastic petridish can be seen. Such μm-scale features may result in the formation of the rough region upon anodization, as shown in **Figure 4.3(a)**.

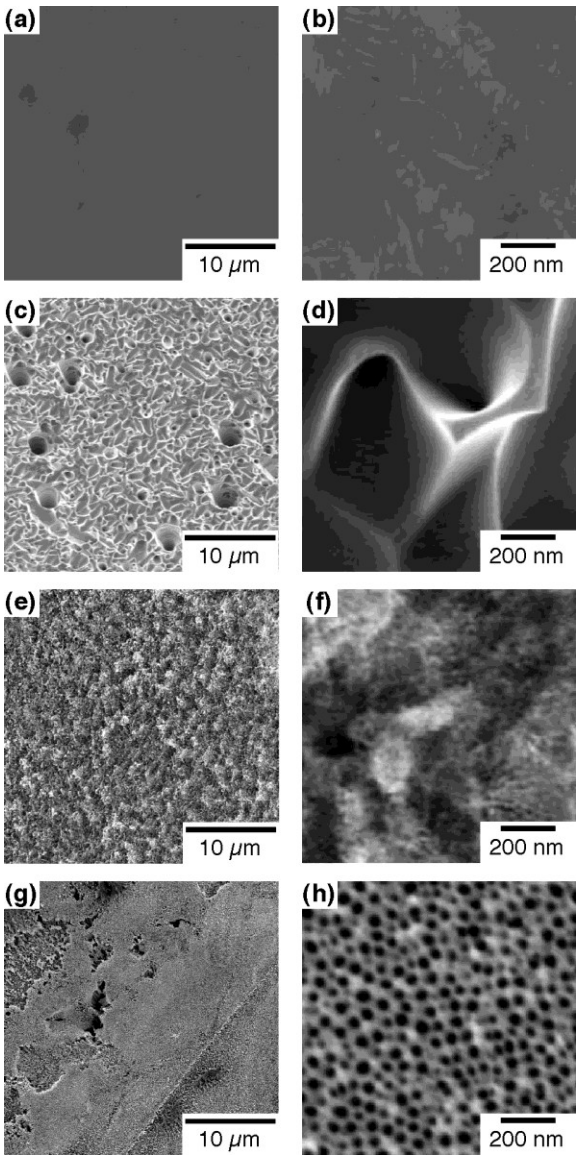

Figure 4.6 SEM images of planar gallium films on Si substrates before anodization (a,b); after anodization in 4 M H_2SO_4 at 1 V (c,d); 5 V (e,f); and 15 V (g,h). The *i–t* curves for the latter three samples are shown in Figure 1.

After anodization, the surface morphology of the solid gallium film changed significantly, depending upon the anodization voltage. At 1 V, large and small pits were observed across the film surface (**Figure 4.6(c)** and **(d)**). Similar surface features were observed regardless of anodization time up to 2 hours. The observation of the pits may reflect the heterogeneous formation of anodic oxide, which originates from the surface roughness and the presence of impurities in the solid gallium film, and its quick dissolution into 4 M H_2SO_4. Indeed, the film surface mainly consisted of metallic gallium (**Figure 4.5(b)**).

Table 4.1 Pore Diameter, Interpore Spacing and Pore Density Obtained at Nanoporous Gallium Oxide Anodized for One Hour under Different Conditions.

sample type[a]	electrolyte	voltage	diameter (nm)[b]	spacing (nm)[b]	density (pores/μm^2)[c]
planar film [3][d]	4 M H_2SO_4	10 V	27.5 ± 4.8	44.7 ± 5.3	430 ± 30
planar film [2][d]	4 M H_2SO_4	15 V	40.5 ± 8.3	59.1 ± 7.2	270 ± 20
planar film [2][d]	6 M H_2SO_4	10 V	18.7 ± 3.4	36.6 ± 5.2	710 ± 70
monolith [1][d]	6 M H_2SO_4	10 V	19.5 ± 2.5	35.4 ± 3.9	710 ± 60

[a] Planar gallium film on Si wafer (planar film) or capillary-incorporated monolith (monolith). [b] Average and standard deviation from all the pores measured: 50 pores from each sample. [c] Density values from three different areas (1 x 1 μm^2) on each samples. [d] The numbers of samples examined are shown in square brackets.

At 5 V, the low-magnification image (**Figure 4.6(e)**) did not show any pits. The surface morphology did not depend on anodization time up to 3.5 hours. The relatively uniform surface reflected the efficient formation of an anodic oxide layer, as supported by the large anodic current in the *i–t* curve (**Figure 4.1**). The high-magnification image (**Figure 4.6(f)**) shows some nanoscale features, but not well-organized structures (see **Figure 4.3(b)**), probably because the field-induced instability required for self-ordering of nanopores[33] could not be attained at relatively low anodization voltage.

At 15 V, the low-magnification image (**Figure 4.6(g)**) was very similar to that obtained at 10 V (**Figure 4.3(a)**). Well-organized nanopores were observed in the smooth regions (**Figure 4.6(h)**). As compared to those at 10 V, the nanopore diameter (41 ± 8 nm on samples anodized for one hour; **Table 4.1**) was significantly larger and less uniform. The larger diameter of nanopores anodized at a larger voltage was similarly observed in anodization of metallic aluminum,[34] which has been explained by the thicker oxides that are formed under higher anodization voltages at the early stage of nanopore formation.[10,11]

4.3.4 Effects of H2SO4 Concentration on i-t Curve and Surface Morphology

Subsequently, the effects of H_2SO_4 concentration on the anodization of solid gallium at 10 V were investigated. **Figure 4.7** shows typical *i–t* curves measured at different H_2SO_4

concentrations. In 1 M H_2SO_4, the anodic current was very small, probably because of the quick formation of the barrier oxide layer. The *i–t* curve at 2 M showed a larger initial anodic current and subsequent gradual current decrease. In 4 M and 6 M H_2SO_4, just after the quick decrease in anodic current, a current increase was observed. The current increase was observed earlier for 6 M solution, probably reflecting the quicker dissolution of the anodic oxide.

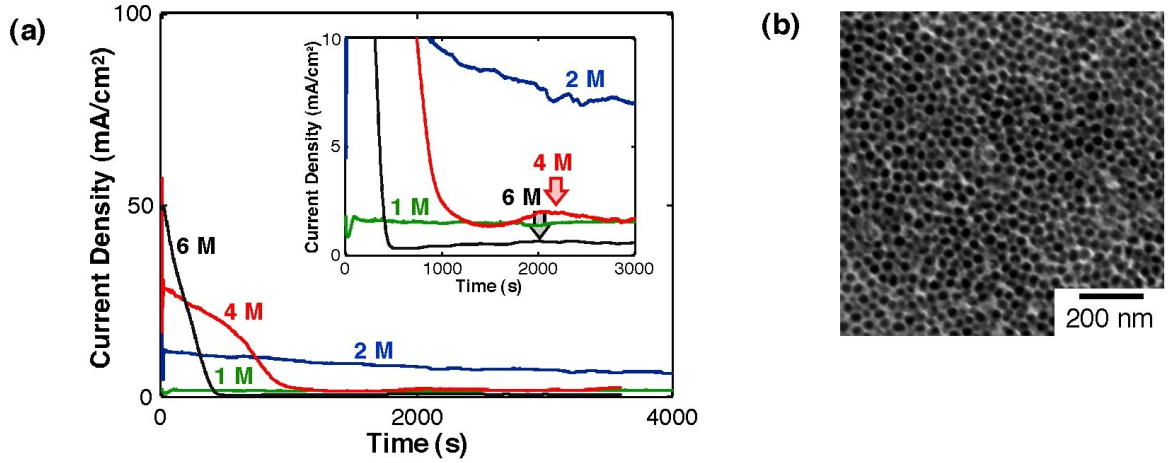

Figure 4.7 (a) Typical current–time (*i–t*) curves for anodization of planar gallium films on Si substrates at 10 V in aqueous H_2SO_4 solutions of different concentrations. The geometrical area used were those defined by the O-ring (0.80 cm in diameter). Note that the curve at 4 M H_2SO_4 was obtained from a different gallium film than that in Figure 1, but the *i–t* curve and SEM images (as shown in (b)) were very similar. (b) SEM image of an anodized planar gallium film that was anodized at 10 V in 4 M H_2SO_4 for 1 hr, whose *i–t* curve is as shown in (a).

Figure 4.8 summarizes the SEM images of planar gallium surfaces anodized at 10 V in 1, 2 and 6 M H_2SO_4. At 1 M (**Figure 4.8(a) and (b)**), the surface was not smooth, probably because the oxide dissolution took place heterogeneously due to its slow removal in relatively low concentration H_2SO_4. This result indicates that the anodic formation of nanoporous gallium oxide requires higher H_2SO_4 concentration than that of nanoporous anodic alumina.[35] This observation is probably related to the lower solubility of the former as compared with the latter (*vide supra*).[18] At 2 M, the surface was smoother than that at 1 M (**Figure 4.8(c)**), but did not show well-ordered nanopores (**Figure 4.8(d)**). Note that the surface features obtained on

gallium surfaces anodized in 1 M or 2 M H_2SO_4 were similarly observed regardless of anodization time (3 hours). In contrast to anodization in 1 M or 2 M H_2SO_4, that in 6 M H_2SO_4 (**Figure 4.8(e) and (f)**) offered a gallium film surface similar to that in 4 M H_2SO_4 (**Figure 4.3(a) and (b)**). However, as compared with the nanopores obtained via anodization at 4 M, these nanopores were less ordered and smaller in diameter (19 ± 3 nm on samples anodized for one hour; **Table 4.1**). The formation of smaller nanopores was also reported in anodization of aluminum, which was explained by the faster field-assisted oxide dissolution at the nanopore tip at the higher acid concentration.[36]

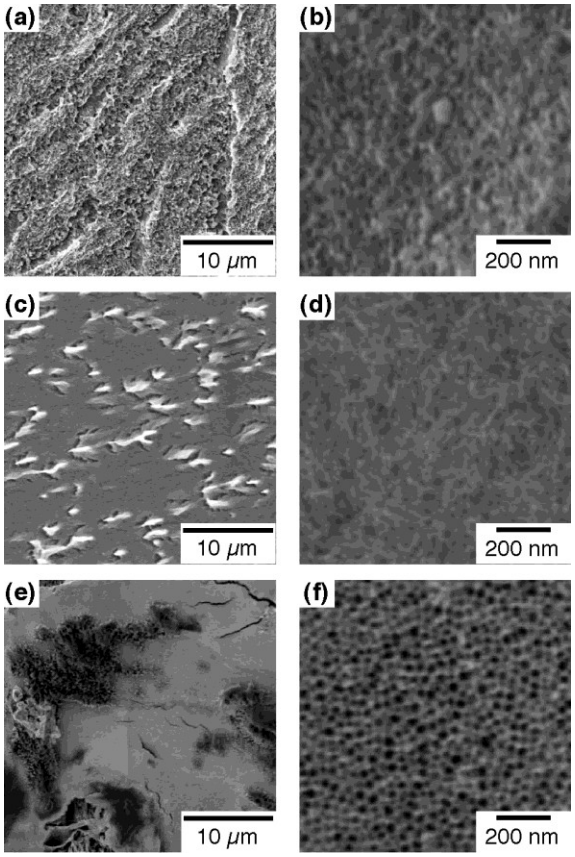

Figure 4.8 SEM images of planar gallium films on Si substrates after anodization at 10 V in (a,b) 1 M H_2SO_4; (c,d) 2 M H_2SO_4; and (e,f) 6 M H_2SO_4. The *i–t* curves measured at these samples are shown in Figure 4.7.

4.3.5 Fabrication of Nanoporous Anodic Oxide on a Capillary-Incorporated Solid Gallium Monolith

Because of its low melting point, solid gallium can be incorporated into confined spaces like microchannels.[19] Anodization of solid gallium within a confined space will provide a simple means for integrating nanoporous monoliths with microfluidic devices. Here, we examined the anodization of solid gallium incorporated at the end of a glass capillary to demonstrate the fabrication of nanoporous anodic gallium oxide within a confined space.

Figure 4.9(a) shows an *i–t* curve recorded from a capillary-incorporated solid gallium monolith in 6 M H_2SO_4 at 10 V. Capillary-incorporated samples needed to be anodized for a longer time than planar films to obtain the increase in anodic current, and thus nanoporous structures, probably because of the larger potential drop within the solid gallium: The gallium layer thickness was *ca*. 100 μm and *ca*. 1 mm for the planar films and capillary-incorporated monoliths, respectively. The anodic current density in the *i–t* curve was significantly larger than that of the planar film under the same conditions (**Figure 4.7**), probably because the solid gallium surface was rougher as indicated by the SEM image of the anodized gallium-incorporated capillary (**Figure 4.9(b)**). In addition, the relatively small area of the carbon counter electrode (ca. 0.16 cm^2) may limit the current measured in the experiments, which gives smaller current density on the planar films with larger area. The surface was not perfectly smooth or uniform, as nanoporous oxides can be found as brighter regions (ca. 65% of the entire surface). There is no clear gap found between the monolith and capillary wall.

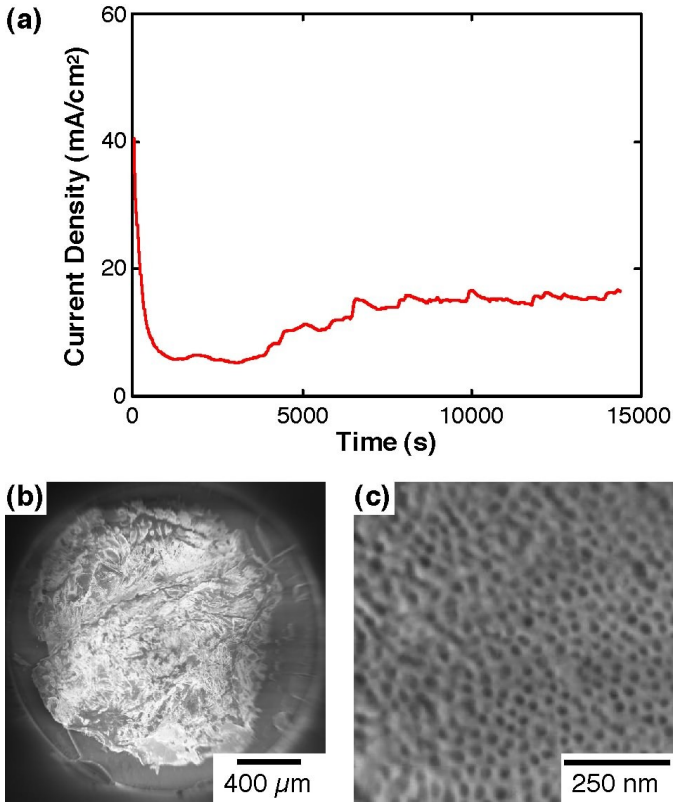

Figure 4.9 (a) A current-time (*i–t*) curve for anodization of a capillary-incorporated gallium monolith at 10 V in 6 M H_2SO_4. The geometrical area was defined by the I.D. of the capillary (1.75 mm). (b,c) SEM images of the anodized gallium monolith. The capillary is shown in (b).

Figure 4.9(c) shows a high-magnification SEM image of the surface of the anodized gallium monolith. As with the anodized planar films (**Figure 4.8(f)**), well-organized nanopores were found on the anodized surface. The diameter of the nanopores was 20 ± 3 nm, close to that obtained on the planar films (**Table 4.1**), although the anodization time was longer. The similar pore diameter suggests that anodization conditions, such as effective anodization potential at the solution/oxide/metal interfaces and concentration polarization near the gallium surface during anodization, were different for the planar films and the capillary system. The pore density on the capillary samples was similar to that obtained on the planar films. These results indicate that a nanoporous anodic oxide monolith can be fabricated for a capillary-incorporated gallium monolith under conditions similar to those used for a planar gallium film.

4.4 Conclusions

In this study, we systematically measured the anodization current and surface morphology of solid metallic gallium anodized under different conditions. Self-organized nanoporous structures were obtained by anodization in ice-cooled aqueous solutions of relatively high H_2SO_4 concentrations (4 and 6 M) at relatively high anodization voltages (10 and 15 V). Smaller pore diameters can be obtained by anodization at higher H_2SO_4 concentrations and at lower anodization voltages. Higher H_2SO_4 concentration was required for anodic nanopore formation on gallium as compared with aluminum. We could successfully show the formation of nanoporous anodic gallium oxide layer in a monolith confined in a capillary, demonstrating the capability to integrate nanoporous monoliths with microfluidic channels.

There are several challenges for future applications of the nanoporous gallium oxide monoliths. First, well-organized nanoporous structures were obtained only on smooth gallium surfaces. Preparation of uniformly smooth solid gallium surfaces is required to fabricate uniform nanoporous structures over wide areas. Instead of the plastic petridish, template materials with flatter surfaces and weak gallium adhesion may be required to improve the uniformity of the anodic films. Second, the length of the anodic nanopores is currently limited to ~ 2 μm. As the *i*–*t* curves in **Figures 4.1** and **4.7** suggest, anodic nanopore formation ceases after a relatively short period of time. Further optimization of the anodization conditions, including temperature and solution composition, will be required to obtain longer nanopores. In addition, methods to remove the barrier oxide and metallic gallium on the other side need to be established for fabrication of monoliths comprising nanopores that bridge two fluidic spaces. To summarize, we have demonstrated that anodization of fusible metallic gallium provides a simple and controlled means for preparing nanoporous materials in different geometries. The physical and chemical properties of the self-organized nanoporous gallium oxide will be further studied to realize the potential applications.

References

(1) Chen, H. M.; Liu, R.-S. *J. Phys. Chem. C* **2011**, *115*, 3513.

(2) Baker, L. A.; Jin, P.; Martin, C. R. *Crit. Rev. Solid State Mater. Sci.* **2005**, *30*, 183.

(3) Martin, C. R. *Science* **1994**, *266*, 1961.

(4) Kline, T. R.; Tian, M.; Wang, J.; Sen, A.; Chan, M. W. H.; Mallouk, T. E. *Inorg. Chem.* **2006**, *45*, 7555.

(5) Liu, R.; Duay, J.; Lee, S. B. *Chem. Commun.* **2011**, *47*, 1384.

(6) Perry, J. L.; Martin, C. R.; Stewart, J. D. *Chem. Eur. J.* **2011**, *17*, 6296.

(7) Deen, W. M. *AIChE J.* **1987**, *33*, 1409.

(8) Diggle, J. W.; Downie, T. C.; Goulding, C. W. *Chem. Rev.* **1969**, *69*, 365.

(9) Masuda, H. In *Ordered Porous Nanostructures and Applications*; Wehrspohn, R. B., Ed.; Springer Science+Business Media, Inc: New York, 2005, p 37.

(10) Sulka, G. D. In *Nanostructural Materials in Electrochemistry*; Eftekhari, A., Ed.; Wiley-VCH Verlag GmbH &Co: Weinheim, 2008, p 1.

(11) Ghicov, A.; Schmuki, P. *Chem. Commun.* **2009**, 2791.

(12) Shankar, K.; Basham, J. I.; Allam, N. K.; Varghese, O. K.; Mor, G. K.; Feng, X.; Paulose, M.; Seabold, J. A.; Choi, K.-S.; Grimes, C. A. *J. Phys. Chem. C* **2009**, *113*, 6327.

(13) Shin, H.-C.; Dong, J.; Liu, M. *Adv. Mater.* **2004**, *16*, 237.

(14) Rangaraju, R. R.; Raja, K. S.; Panday, A.; Misra, M. *Electrochim. Acta* **2010**, *55*, 785.

(15) Downs, A. J., Ed. *Chemistry of Aluminum, Gallium, Indium and Thallium*; Blackie Academic & Professional: London, 1993.

(16) Popova, T. I.; Bagotskaya, I. A.; Moorhead, E. D. In *Encyclopedia of Electrochemistry of the Elements*; Bard, A. J., Ed.; Marcel Dekker: New York, 1976; Vol. 8, p 207.

(17) Tuck, C. D. S.; Hunter, J. A.; Scamans, G. M. *J. Electrochem. Soc.* **1987**, *134*, 2970.

(18) Speight, J. G. *Lange's Handbook of Chemistry, 17th Ed.*; McGraw-Hill: New York, 2005.

(19) So, J.-H.; Dickey, M. D. *Lab Chip* **2011**, *11*, 905.

(20) Miyata, T.; Nakatani, T.; Minami, T. *J. Lumin.* **2000**, *87-89*, 1183.

(21) Ogita, M.; Higo, K.; Nakanishi, Y.; Hatanaka, Y. *Appl. Surf. Sci.* **2001**, *175*, 721.

(22) Bartic, M.; Ogita, M.; Isai, M.; Baban, C.-L.; Suzuki, H. *J. Appl. Phys.* **2007**, *102*, 023709.

(23) Hou, Y.; Wang, X.; Wu, L.; Ding, Z.; Fu, X. *Environ. Sci. Technol.* **2006**, *40*, 5799.

(24) Tsuneoka, H.; Teramura, K.; Shishido, T.; Tanaka, T. *J. Phys. Chem. C* **2010**, *114*, 8892.

(25) Pileni, M. P. In *Nanoscale Materials in Chemistry*; Klabunde, K. J., Ed. New York, 2001, p 61.

(26) West, C.; Mokaya, R. *Chem. Mater.* **2009**, *21*, 4080.

(27) Deshmane, C. A.; Jasinski, J. B.; Carreon, M. A. *Eur. J. Inorg. Chem.* **2009**, 3275.

(28) Yang, F. *Electrochem. Solid-State Lett.* **2006**, *9*, C44.

(29) Hoar, T. P.; Yahlom, J. *J. Electrochem. Soc.* **1963**, *110*, 614.

(30) Masuda, H.; Takenaka, K.; Ishii, T.; Nishio, K. *Jpn. J. Appl. Phys.* **2006**, *45*, L1165.

(31) Sulka, G. D.; Stroobants, S.; Moshchalkov, V. V.; Borghs, G.; Celis, J.-P. *J. Electrochem. Soc.* **2004**, *151*, B260.

(32) Lide, D. R., Ed. *CRC Handbook of Chemistry and Physics, 82nd ed.*; CRC Press: Boca Raton, FL, 2001.

(33) Hebert, K. R.; Albu, S. P.; Paramasivam, I.; Schmuki, P. *Nat. Mater.* **2012**, *11*, 162.

(34) Paolini, G.; Masoero, M.; Sacchi, F.; Paganell.M *J. Electrochem. Soc.* **1965**, *112*, 32.

(35) Masuda, H.; Hasegwa, F.; Ono, S. *J. Electrochem. Soc.* **1997**, *144*, L127.

(36) Parkhutik, V. P.; Shershulsky, V. I. *J. Phys. D-Appl. Phys.* **1992**, *25*, 1258.

Chapter 5 - Assessment of the Surface Chemical Properties of Self-Organized Nanoporous Anodic Gallium Oxide

5.1 Introduction

The development of self-organized nanoporous materials has attracted tremendous interest, investment and effort in research and development in recent times. Self-organized nanoporous materials possess unique surface and structural properties that allow them to be used in a variety of applications such as separation,[1] catalysis,[2] sensor,[3] isolation and purifications of biomolecules.[4] In case of self-organized materials based on anodic alumina, the surface features and properties of aluminum metal before anodic oxidation has been shown to have an effect on the properties of the nanoporous anodic alumina.[5] In this regard, understanding the surface features and chemical properties of both the metal and the anodic metal oxide helps elucidate the formation mechanism of the nanoporous metal oxide structure as well as hint at the possible applications of the nanoporous anodic metal oxides.

The self-organized nanoporous anodic gallium oxides as described in chapter 4 were prepared from metallic gallium for the first time, and thus the surface chemical properties of these materials are yet to be explored. On the other hand, common gallium oxide found in the form of nanocrystals,[6] nanorods[7] have been synthesized and characterized extensively. They are known as wide band semiconductor (band gap ~4.8 eV). They possess high n-type conductivity and charge carrier mobility due to the presence of structural defects, particularly oxygen vacancies. The characterization of the structural surface features of these gallium oxide nanocrystals and nanorods has helped realize their importance in applications such as catalysts,[8] and gas sensors.[9]

In order to understand the surface chemical properties of the self-organized nanoporous anodic gallium oxide structures, we employed hexagonally arranged cylindrical pores of anodic gallium oxide with diameters of 18 - 30 nm[10] for potentiometric studies. The surface acidity/basicity of the porous oxide surfaces can be investigated by potentiometry. Additionally, gallium metal as well as barrier layer gallium oxide formed by oxidation in neutral solution were examined for potentiometric studies. It is important to understand the surface chemical properties of the gallium metal and gallium metal oxides for two reasons. First, these studies could provide insight to improve the pore size uniformity and equal spacing between the pores. Monodispersed,

equally spaced pores can be used as a template for controlled synthesis of other nanomaterials. Second, better understanding of the surface chemical properties of these self-organized anodic gallium oxide could lead to their future applications as efficient sensors and catalysts.

The potentiometric studies revealed that the bare planar gallium substrates show significantly larger potentiometric responses to pH as compared to the porous and non-porous gallium oxides. The potential of the bare planar gallium substrates decreased with an increase in solution pH. The response time was quite slow (ca. 5 min) and magnitude of response was larger at alkaline pH. The oxide-coated substrates exhibited pH response only at acidic pH (≤ 4), and their response time is even slower than the bare planar gallium substrate.

5.2 Experimental Section

5.2.1 Chemicals and Materials

All solutions were prepared with water having a resistivity of 18 MΩ cm or higher (Barnstead Nanopure Systems). High purity gallium (99.99%) was purchased from GalliumSource, LLC and used as received. Sulfuric acid (Fisher Chemical, Certified ACS Plus) was used without further purification. Boric acid (Fisher Chemical), sodium borate (Fisher Chemical), lithium chloride (Acros Organics), lithium hydroxide (Fisher Chemical), and hydrochloric acid (Fisher Chemical, Certified ACS Plus) were used as received. Si (100) wafers (p-type) were purchased from University Wafer.

5.2.2 Electrode Preparation

Planar gallium films on a Si-substrate were prepared under Ar atmosphere according to the procedure described previously.[10] Anodization was carried out at 10 V in 4 and 6 M aq. H_2SO_4 for planar Ga films on a substrate.[10] In addition, anodization in a solution mixture of 0.5 M boric acid with 0.005 M sodium tetraborate was performed to obtain a barrier layer gallium oxide as described previously.[11] After anodization, the samples were washed thoroughly with ultra pure water and kept immersed in ultra pure water overnight before the potentiometric measurements were made.

5.2.3 Potentiometric measurements

Potentiometric measurements were performed in a cell as shown in Scheme 1. All the solutions employed contain 0.01 M LiCl as a supporting electrolyte, since LiCl did not exhibit any potentiometric responses up to 0.1 M. Solutions of LiOH or HCl containing 0.01 M LiCl were used to adjust the solution pH. The solution was stirred by using a stir bar. Potentiometric time curves were recorded every 30 seconds and the solution pH was changed once the differential quotient ($\Delta E/\Delta t$) of a potential-time curve became smaller than a prechosen value ($\Delta E/\Delta t \leq 1$ mV/min).

Scheme 1

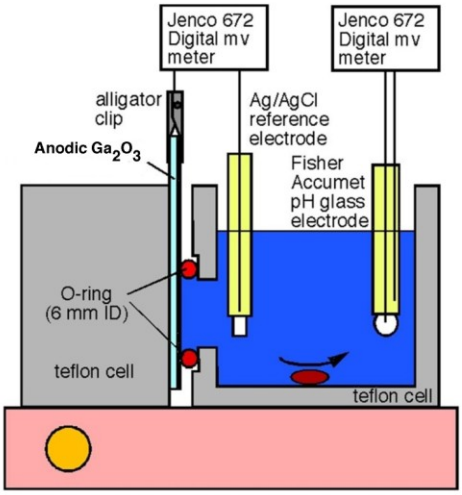

5.3 Results and Discussion

In this study, we investigated the surface chemical properties of planar gallium films, self-organized nanoporous anodic gallium oxide structures and barrier layer gallium oxide using potentiometry. Shown in Scheme 1 is the potentiometric cell where a substrate of interest was fixed using a O-ring with the anodized surface (in case of oxides) and metal surface (in case of gallium metal) exposed to the solution side. The EMF value of the metal or oxide electrode was then recorded as the pH of a solution containing 0.01 M LiCl as a supporting electrolyte was changed by adding HCl or LiOH solution. The solution was stirred at all times. pH of the 0.01 *M* LiCl solution (pH ~ 5.4 initially) was changed to more basic at first and then to acidic and

potential time curves recorded. The nanoporous anodic gallium oxides and the barrier layer gallium oxide showed response only at the acidic pH (pH ≤ 4). The metallic gallium substrates showed a decrease in potential with increasing pH, as with a pH glass electrode.

5.3.1 Time course and response time

A stepwise change in pH was realized by adding a certain amount of HCl or LiOH into a solution containing 0.01 *M* LiCl as a supporting electrolyte. The time curves of potentials were obtained for each electrode type from which response time and magnitude of response can be discussed. Response time is defined as the length of time necessary to obtain a stable electrode potential upon a change in solution pH. The response of each electrode type is described one at a time in the sections below.

5.3.1.1 Potentiometric Response of Self-Organized Nanoporous Gallium Oxides

The nanoporous anodic gallium oxide substrates were prepared in 4 M and 6 M H_2SO_4 at an applied voltage of 10 V as described in chapter 4. Thus prepared anodic substrates were assembled in a potentiometric cell as shown in Scheme 1 and ultrapure water was filled in the solution chamber and the sample stored as such overnight. The potentiometric measurements were performed the next day. This conditioning of the electrode needed to be done so as to ensure that H_2SO_4 remaining in the nanopore (if any) is removed. Some of the electrodes measured immediately after preparation showed the decrease of pH of 0.01 *M* LiCl solution in the solution chamber even when no HCl was added probably due to leaching of H_2SO_4 remaining in the nanopores into the solution. In addition to the conditioning, the anodized samples were kept under reduced pressure to remove air bubbles from the nanopores.

Figure 5.1a shows a potentiometric time courses for a substrate that was anodized in 4 M H_2SO_4. The EMF of this electrode showed a gradual increase irrespective of the direction of the pH change of the electrolyte solution. This meant that the surface of the anodic oxide did not possess any sites for the interaction and/or exchange of the H^+/OH^- from the solution. When the pH reached to more acidic value, the magnitude of the response suddenly increased. This sudden increase in magnitude is probably due to change in the surface oxide properties induced by the acidic pH of the solution. The response time was very slow: it took ca. 10 minutes to reach a stable potential ($\Delta E/\Delta t \leq 1$ mV/min).

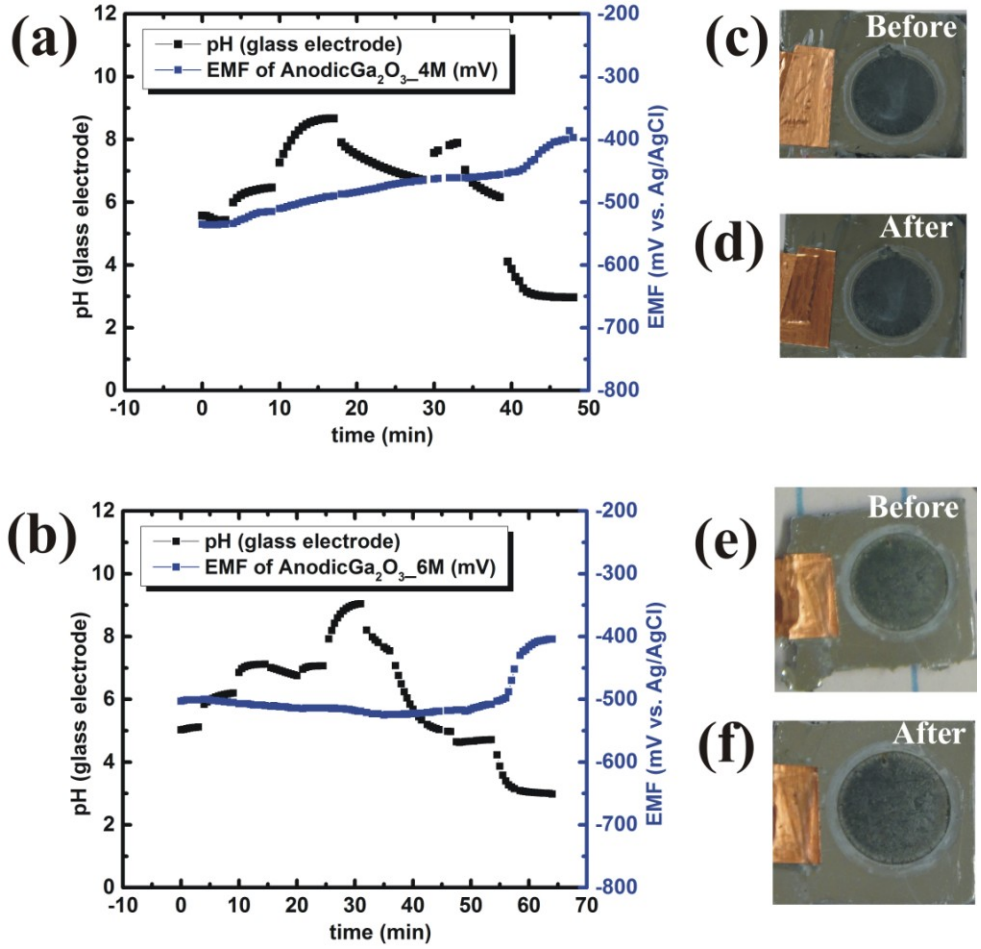

Figure 5.1 Potentiometric time courses for self-organized nanoporous gallium oxide substrate that were anodized at 10 V in (a) 4 M H_2SO_4, and (b) 6 M H_2SO_4. The supporting electrolyte was 0.01 M LiCl and pH was changed by adding HCl and LiOH solutions containing 0.01 M LiCl. A time course for a pH glass electrode measured simultaneously is also shown to indicate solution pH changes. Optical micrograph of the 4 M H_2SO_4 anodized gallium substrate (c) before and (d) after the potentiometric measurements as well as those of the 6 M H_2SO_4 anodized gallium substrate (e) before and (d) after the potentiometric measurements are also shown. The area inside the circular ring reveals the anodized area which did not show any noticeable change in appearance after the potentiometric experiments.

Figure 5.1c,d are the pictures of the anodic metal oxide before and after the time course measurements, respectively. The anodized surface did not show any noticeable change in appearance after the potentiometric measurements, suggesting the stability and inertness of the oxide to aqueous solutions.

Figure 5.1b is a time course for a gallium substrate anodized in 6 M H_2SO_4. The potentiometric response of the oxide surface was very small upon pH changes from initial pH (ca. 5) to more basic pH (ca. 9) and back to pH 5. The response time for this case was ~ 5 minutes. When the pH was changed to pH 4 to 3, a large increase in potential was observed as with the substrate anodized in 4 M H_2SO_4. This means that the surface properties of the oxides altered at the acidic pH range. At this time, further characterization is necessary to fully understand the observations. The appearance of the anodized sample surface as shown in **Figure 5.1e,f** before and after potentiometric measurements were almost the same.

5.3.1.2 Potentiometric Response of a Planar Gallium Substrate

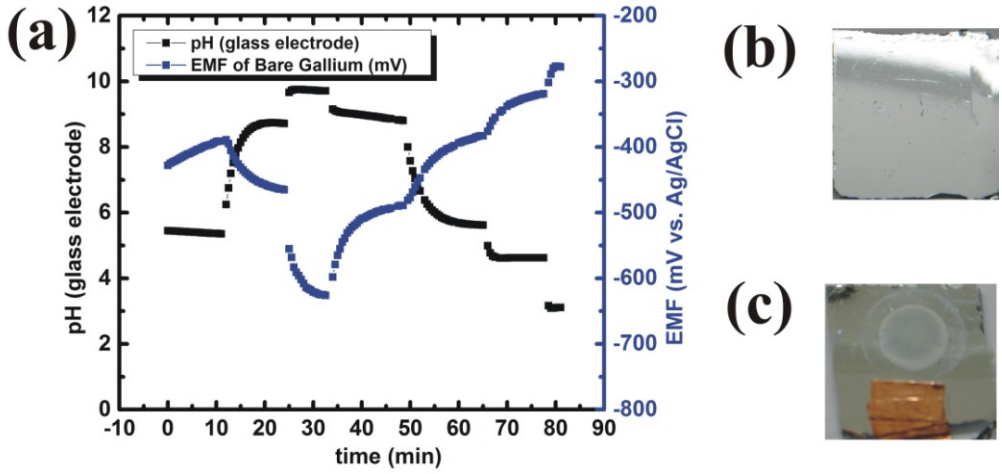

Figure 5.2 (a) A potentiometric time course measured for a bare planar gallium substrate. The supporting electrolyte was 0.01 M LiCl and pH was changed with solutions of HCl and LiOH containing 0.01 M LiCl. A time course for a pH glass electrode measured simultaneously is also shown to indicate solution pH changes. Optical micrographs of the bare planar gallium substrate (b) before and (c) after the potentiometric measurements. The bare planar gallium substrate appeared cloudy after potentiometric measurements as shown by the area within the circular ring.

Figure 5.2a shows a potential time course for a planar gallium substrate. When the solution pH was changed from neutral to basic, the EMF decreased. Subsequently, the EMF increased upon a decrease in pH from basic to acidic. Response time was relatively slow (~ 5 minutes) as compared to that of a glass pH electrode. The magnitude of the response was large at the alkaline pH region compared to the acidic region.

The surface of the gallium substrate appears cloudy after potentiometric measurements (Figure 5.2c) in contrast to the mirror-like surface of the initial planar gallium substrate. This means that gallium surface is susceptible to HCl, LiOH and/or LiCl.

5.3.1.3 Potentiometric Response of Barrier Layer Gallium Oxide

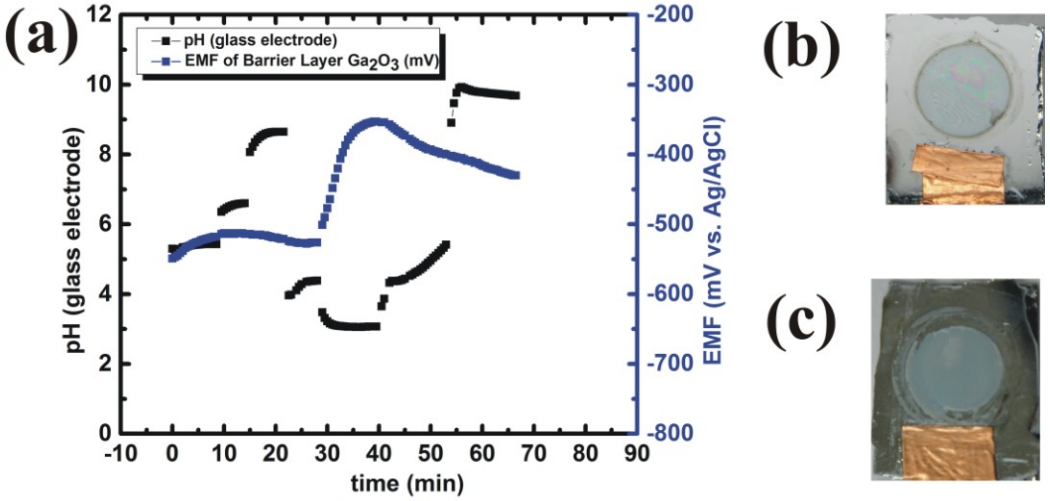

Figure 5.3 (a) A potential time course measured for a barrier layer gallium oxide that was obtained by anodic oxidation in a mixture of 0.5 M boric acid with 0.005 M sodium tetraborate (pH 7.6). The supporting electrolyte was 0.01 M LiCl and pH was changed with solutions of HCl and LiOH containing 0.01 M LiCl. A time course for a pH glass electrode measured simultaneously is also shown to indicate solution pH changes. Optical micrograph of the barrier layer gallium oxide (b) before and (c) after the potentiometric measurements. The area inside the circular ring reveals the oxidized area which changed to greyish after the potentiometric experiments.

Figure 5.3a shows a potentiometric time course for barrier layer oxide which was formed by anodization in a solution mixture of 0.5 M boric acid and 0.005 M sodium tetraborate (pH

7.6). The EMF response was very small for this electrode as the pH was changed from neutral to basic. The response time was ~ 7 minutes. When pH was slightly above 4, sudden increase in the potential was observed. When the pH was changed to more acidic, huge potential change was observed. When the pH was changed to more basic region next, a decrease in the potential was observed as opposed to small response earlier in the same direction. This suggests that these oxide surfaces need to be treated to acidic solutions first so that they respond to changes in the pH. The appearance of the sample changed to greyish after the potentiometric measurement (F**igure 5.3c**) as opposed to the surface before the measurement (**Figure 5.3b**).

5.4 Conclusions

In this study, we investigated the surface chemical properties of the nanoporous anodic gallium oxide, planar gallium film and barrier layer gallium oxide. The study of the surface chemical properties of the metallic gallium, nanoporous and barrier gallium oxides provide directions for their potential applications. The EMF response of the nanoporous anodic metal oxides was small and the response time was very slow (~10 minutes). The appearance of the oxide did not show noticeable changes. As for the bare gallium, EMF response was comparatively larger at alkaline pH. The response time was slow (~5 minutes). The film appeared cloudy after the potentiometric measurements. In the case of barrier layer gallium oxide, the electrode showed an increase in EMF at pH $\leq$ 4. The response time was slower than bare gallium film and similar to the anodic oxides. In conclusion, the potentiometric studies to understand the surface chemical properties of the bare gallium film and the oxides revealed some differences: the oxide surfaces exhibited potential responses only at the acidic pH, whereas the gallium metal showed changes in the EMF at the pH range examined (3-10). Also, the response time for all these surfaces to changes in pH was slow. The response was smaller for anodic gallium oxides as compared to the gallium metal.

References

(1) Baker, L. A.; Jin, P.; Martin, C. R. *Crit. Rev. Solid State Mater. Sci.* 2005, *30*, 183.

(2) Chu, S. Z.; Inoue, S.; Wada, K.; Hishita, S.; Kurashima, K. *Adv. Funct. Mater.* 2005, *15*, 1343.

(3) Cheng, M. S.; Lau, S. H.; Chow, V. T.; Toh, C.-S. *Environ. Sci. Technol.* 2011, *45*, 6453.

(4) Yu, S. F.; Lee, S. B.; Kang, M.; Martin, C. R. *Nano Lett.* 2001, *1*, 495.

(5) Rashidi, F.; Masuda, T.; Asoh, H.; Ono, S. *Surf. Interface Anal.* 2013.

(6) Wang, T.; Farvid, S. S.; Abulikemu, M.; Radovanovic, P. V. *J. Am. Chem. Soc.* 2010, *132*, 9250.

(7) Gao, Y. H.; Bando, Y.; Sato, T.; Zhang, Y. F.; Gao, X. Q. *Appl. Phys. Lett.* 2002, *81*, 1507835.

(8) Hou, Y.; Wang, X.; Wu, L.; Ding, Z.; Fu, X. *Environ. Sci. Technol.* 2006, *40*, 5799.

(9) Bartic, M.; Baban, C.-I.; Suzuki, H.; Ogita, M.; Isai, M. *J. Am. Ceram. Soc.* 2007, *90*, 2879.

(10) Pandey, B.; Thapa, P. S.; Higgins, D. A.; Ito, T. *Langmuir* 2012, *28*, 13705.

(11) Li, Y.; Shimada, H.; Sakairi, M.; Shigyo, K.; Takahashi, H.; Seo, M. *J. Electrochem. Soc.* 1997, *144*, 866.

Chapter 6 - Conclusions and Future Directions

In this dissertation, self-organized nanoporous materials have been utilized for chemical separations and chemical sensing applications. Our work is driven by the fact that the self-organized, uniform, cylinder-shaped nanopores provide a unique platform for chemical separations and chemical sensing. All the work described in the projects aim at understanding the materials, methods and mechanisms of utilizing these nanoporous materials for different applications. It is our sincere hope that other researchers will benefit from our results to develop better materials and devices in future.

In the forthcoming sections, all the projects will be summarized one at a time along with recommendations for future work.

6.1 Understanding the diffusion of cytochrome c inside PS-*b*-PMMA nanopores using electrochemical methods

In this study, we used ~30 nm thick nanoporous films derived from PS-*b*-PMMA having different pores diameters: 11, 14 and 24 nm respectively to study the diffusion of cytochrome c within the nanopores. Within 11 and 14 nm nanopores, cytochrome c molecule experienced greater hindrance of its diffusion and were more strongly adsorbed. This is probably due to the geometrical restrictions imposed by the simultaneous penetration of multiple cytochrome c molecules into single nanopores. In case of 24-nm diameter pores, cytochrome c exhibited diffusion-controlled CVs. In order to better understand the experimental results, finite-element computer simulations were performed which made it possible to assess the structure of the nanoporous films and the diffusion coefficients of redox species within the nanopores.

In future, the results reported in this study will provide guidance in designing recessed nanodisk array electrodes for size-based chemical sensing and also for controlled immobilization of biomolecules within nanoporous media for biosensors and bioreactors. The results of the simulation studies are particularly encouraging. The studies undertaken to understand the effects of interpore spacing clearly showed the presence of an optimum interpore spacing for detection of physical blocking of the RNE nanopores. A decrease in faradic current induced by physical blocking can be measured for RNEs with relatively large interpore spacing, *i.e.*, relatively low pore density. The relatively low pore density may also be required for detecting permeability

changes induced by a decrease in effective nanopore radius. Additionally, the effects of apparent diffusion coefficients within the pores (D_{pore} dependence) show the possibility to develop RNE-based chemical sensors based on changes in chemical environment within the nanopores. For example, the diffusion coefficients within the pores depend on solution viscosity in nanopores. Thus, RNEs may be applicable for electrochemical detection of analytes that can change solution viscosity upon their binding to the nanopore surface.

6.2 Anodization of metallic gallium to form self-organized anodic gallium oxide

In this study, we investigated the conditions for anodization of solid gallium metal so as to form self-organized nanoporous gallium oxide. Because of its low melting point (ca. 30 °C), metallic gallium can be shaped into flexible structures, permitting the fabrication of nanoporous anodic oxide monoliths within confined spaces like the inside of a microchannel. In our study, solid gallium films prepared on planar substrates were employed to investigate the effects of anodization voltage (1, 5, 10, 15 V) and H_2SO_4 concentration (1, 2, 4, 6 M) on anodic oxide morphology. Self-organized nanopores aligned perpendicular to the film surface were obtained upon anodization of gallium films in ice-cooled 4 and 6 M aqueous H_2SO_4 at 10 V and 15 V. Nanopore formation was recognized by an increase in anodic current after a current decrease reflecting barrier oxide formation. The average pore diameter was in the range of 20 ~ 40 nm with a narrow diameter distribution (relative standard deviation < 10%), and was larger at lower H_2SO_4 concentration and higher applied voltage. The maximum thickness of nanoporous anodic oxide was ca. 2 μm. In addition, anodic formation of self-organized nanopores was demonstrated for a metallic gallium monolith incorporated at the end of a glass capillary.

Nanoporous anodic oxide monoliths formed from a fusible metal like gallium will lead to future development of unique devices for chemical sensing and catalysis. However, there are several challenges that need to be addressed. Since well-organized nanoporous structures were obtained only on smooth gallium surfaces, template materials with flatter surfaces and weak adhesion to gallium may be required to get smooth solid gallium surfaces for anodization. This could improve the uniformity of the anodic films over wide areas. Nanopores obtained thus far are only a few microns in length. Thin membranes are preferred for many important applications such as filtration and selective molecule separation as they provide faster transport rates.

However, sometimes they do not have the satisfactory mechanical strength for such applications as ultrafiltration and the need for thicker membrane arises. Further optimization of anodization conditions, including temperature and solution composition, will thus be required to obtain longer nanopores. In addition, methods to remove the barrier oxide and metallic gallium on the other side need to be established for fabrication of monoliths comprising nanopores that bridge two fluidic spaces.

6.3 Assessment of the Surface Chemical Properties of Self-Organized Nanoporous Anodic Gallium Oxide

In this study, we investigated the surface chemical properties of planar gallium substrates, nanoporous anodic gallium oxide and barrier layer gallium oxide using potentiometry. The study of the surface chemical properties of the gallium metal, nanoporous and barrier oxide layers provide directions for their potential applications. Both the nanoporous anodic and barrier-layer gallium oxides only showed response at acidic pH ($pH \leq 4$). The bare planar gallium metal substrates exhibited pH-dependent potential changes in the pH range of 3-10, but the response were smaller than that of the pH glass electrode.

The surface chemical properties and material properties need to be further investigated using spectroscopic and electrochemical methods of these gallium oxides so as to better understand the material properties. Only then their potential applications will be realized. The advantages of using the porous structures need to be critically evaluated.

In conclusion, this dissertation aimed at the characterization of self-organized, uniform, and cylinder shaped nanopores of PS-*b*-PMMA polymer films and anodic gallium oxide. Furthermore, the studies undertaken in this dissertation hints at the possibility of using these materials for different applications: PS-*b*-PMMA nanoporous thin films for size-based chemical sensing, biosensors and bioreactors whereas nanoporous anodic gallium oxide could be a platform for the growth of other nanostructures, or even be used as sensor or catalyst. There are some challenges to be addressed before these goals are realized though.